Studies of the phase diagrams of core-softened fluids

Gibson, Helen May

Award date:
2007

Awarding institution:
University of Bath

STUDIES OF THE PHASE DIAGRAMS OF CORE-SOFTENED FLUIDS

Submitted by Helen May Gibson
for the degree of
Doctor of Philosophy
of the University of Bath
Department of Physics
May 2007

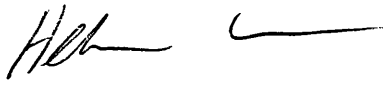

ProQuest LLC
789 East Eisenhower Parkway
P.O. Box 1346
Ann Arbor, MI 48106-1346

Contents

Acknowledgements

Thanks to Nigel Wilding for his excellent guidance and support, and to my parents, Jill and Kenneth Gibson, whose support has also contributed to the completion of this thesis.

Declaration

This thesis has been composed by myself and it has not been submitted in any previous application for a degree. The work reported within was executed by me, unless otherwise stated. Use was made of codes written by Dr Nigel B. Wilding, as explained within. Elements of this work appear in reference [1].

Abstract

A wide variety of single-component substances show evidence of a liquid-liquid phase transition (LLPT) and a liquid-liquid critical point (LLCP). These arise from the competition between two types of bonding: a short-range bond that comes into play at higher temperatures and a longer-range bond that predominates at lower temperatures. However, only two of these substances, water and silica, show a density anomaly (increasing density with increasing temperature) away from the LLPT. Isotropic "core-softened" interaction pair potentials can mimic the competition between the two types of bond, and thus also display LLPTs and LLCPs. However, again, only some of these models display a density anomaly.

In this thesis we predominantly study an isotropic pair potential where the hard core is softened by a ramp. Jagla [2] designed a potential of this kind that produced both an LLPT and a density anomaly. However, the gradient of the LLPT (that is, dP/dT where P is the coexistence pressure at temperature T) was positive, while in water it is negative. Also the LLPT in water is metastable, whereas Jagla's potential generated a stable LLPT. In this thesis we vary the parameters of Jagla's potential and find a set for which the LLPT is metastable and of negative gradient, and the density anomaly is still stable, thus adding to the evidence supporting an LLPT and LLCP in water.

We then study the connection between the LLCP and the meeting point of the LLPT and the high-pressure end of the locus of temperatures of maximum density (TMD). We find a range of parameters for which the TMD always tends towards the LLCP, another range for which the TMD meets the LLPT at sub-critical temperatures, and further parameter sets of the pair potential for which no stable density anomaly is present at all. The parameters that bring about these very

different results differ by only small amounts, showing the extent to which the phase diagrams of real substances are dependent on the finer details of their inter-particle attractions and repulsions.

Abbreviations

FCC	Face centred cubic
GEMC	Gibbs Ensemble Monte Carlo
HCP	Hexagonal close packed
HDA	High density amorphous
HDL	High density liquid
LDA	Low density amorphous
LDL	Low density liquid
LGCP	Liquid-gas critical point
LGPT	Liquid-gas phase transition
LLCP	Liquid-liquid critical point
LLPT	Liquid-liquid phase transition
MC	Monte Carlo
MD	Molecular dynamics
TMD	Temperature of maximum density

VFT	Vogel-Fulcher-Tamman

Chapter 1

Introduction

In this thesis we use computational techniques to better understand some of the features of the phase diagrams of well-known substances.

This introductory chapter will first outline the standard features of a phase diagram, and then go on to describe some methods of analysing the features, before outlining the rest of the thesis.

It is useful to draw phase diagrams of substances by plotting density against temperature and pressure, indicating which areas correspond to crystalline solid, fluid, liquid and gas. An example of a typical phase diagram in the temperature-pressure and density-temperature planes is shown in figure 1.1. Only equilibrium phases are plotted. Amorphous solids are not at equilibrium, and so an amorphous solid does not appear in the phase diagrams.

An amorphous solid looks like a liquid but the particles are not diffusing through the substance. It is metastable with respect to the corresponding crystalline solid at the same temperature and pressure, but the energy barrier is large so it stays amorphous for a very long time.

There is a sharp change in density as a liquid becomes a crystalline solid at constant pressure. This discrete jump in density signifies a *first-order* phase transition, so called because the *first* derivative of the density is infinite at the

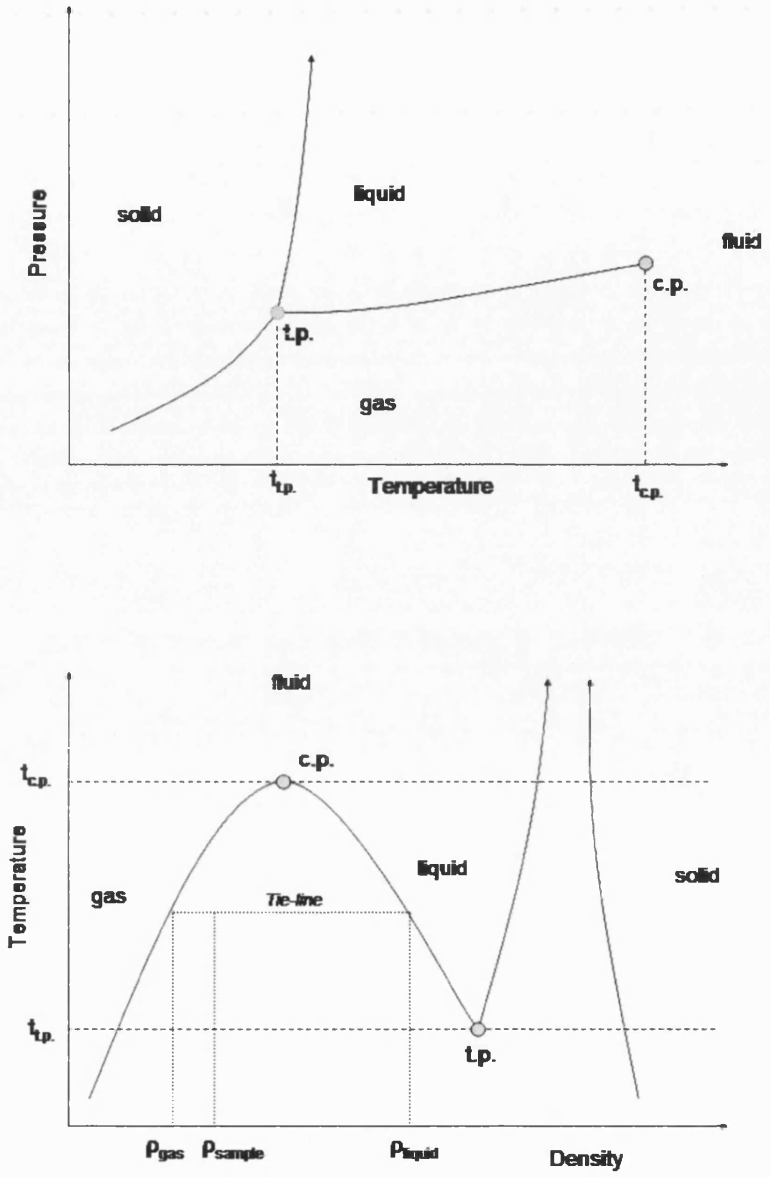

Figure 1.1: **(a)** A typical phase diagram plotted in the temperature-pressure plane. The solid lines indicate lines of coexistence between the two phases on either side of them. The label t.p. indicates the triple point between the solid, liquid and gas, while the label c.p. indicates the critical point terminating the gas-liquid coexistence line. **(b)** A typical phase diagram plotted in the density-temperature plane. The solid lines indicate the boundaries of the phases. At coexistence, for example between a liquid and a gas, a substance at constant pressure with density ρ_{sample} consists of some gas at density ρ_{gas} and some liquid at density ρ_{liquid}, the proportions determined by the lever rule. The triple point and critical point are labelled t.p. and c.p. respectively.

transition. The line of first-order phase transitions plotted on a temperature-pressure graph is also referred to as a line of coexistence, because just at this line it is possible for a substance to have both solid and liquid phases in the same sample, with proportions determined by the lever rule, and in thermodynamic equilibrium with each other.

A first-order phase transition also occurs between liquids and gases. However, in contrast to the solid-fluid lines, the difference between the density of the gas and liquid becomes less and less as the temperature increases, until eventually there is no discrete jump and a plot of density as the experiment progresses is smooth and fully defined in the first derivative, but the *second* derivative is undefined, due to a point of infinite gradient. This is therefore known as a *second-order* phase transition, or, more commonly, a critical point. Above the critical point the plot of density against time is smooth and the gradient is finite at all points. Here the gas and liquid phases can no longer be distinguished and we have the fluid phase.

The behaviour of what are known as *response functions* is very interesting. Response functions, which measure the response of macro variables (such as volume V) to changes in temperature T or pressure P, include thermal expansivity α, isothermal compressibility κ_T and isobaric specific heat capacity C_P.

$$\alpha = \frac{1}{V}\left(\frac{\partial V}{\partial T}\right)_P \tag{1.1}$$

$$\kappa_T = -\frac{1}{V}\left(\frac{\partial V}{\partial P}\right)_T \tag{1.2}$$

$$C_P = \left(\frac{\partial H}{\partial T}\right)_P \tag{1.3}$$

where H is the enthalpy given by $H = U + PV$, where U is the internal energy.

Along the coexistence line, and precisely at the critical point, response functions are infinite. Above the critical point the response functions have maxima. The line of maxima for each response function is known as a Widom line. These lines

converge asymtopically as they approach the critical point [3].

At the low-temperature end of the liquid-gas coexistence line is a *triple point* where the liquid-gas coexistence line meets the liquid-solid and solid-gas coexistence lines. At this point all three phases coexist.

As well as plotting first-order phase transitions, it is also useful to plot spinodal lines. A spinodal line indicates the limit of stability of a phase. For example, a metastable liquid may exist some way into the solid phase, but the further from the melting point the liquid is, the less stable it becomes, until it is mechanically unstable. The liquid spinodal line on a phase diagram indicates the locus beyond which it is impossible to find a liquid phase.

Density-temperature plots of a system at constant pressure can also be illuminating, because in some substances these isobars reveal that the density of a fluid increases with increasing temperature, which is the reverse of what is expected and normally observed. When such a "density anomaly" is observed, this suggests that there are two average bond lengths competing, and that the prevalence of the bonds with the longer separation distance increases with decreasing temperature while the prevalence of shorter bonds increases with increasing temperature. When plotting a density anomaly onto a pressure-temperature phase diagram, it is the temperature of maximum density (TMD) at the pressure of the isobar that is plotted. The locus of density maxima, i.e. the line tracing the TMD points, can reveal interesting phase behaviour.

Another feature which highlights the existence of two preferred separation distances is a negatively-sloped solid-fluid coexistence line on the pressure-temperature plane. This can be seen through the Clapeyron equation:

$$\frac{dP}{dT} = \frac{\Delta S}{\Delta V} \tag{1.4}$$

where $\frac{dP}{dT}$ is the gradient of the coexistence line in the pressure-temperature plane, and ΔS and ΔV are the entropy and volume differences between the phases. By the Clapeyron equation, a negatively-sloped solid-fluid coexistence line indicates that the solid is of lower density than the liquid (assuming that the solid has a lower entropy than the liquid), suggesting that a different type of bonding has

come into play.

In addition, anomalous behaviour of the response functions could indicate competition between bond lengths. For example, in most substances the compressibility decreases with decreasing temperature, but if the compressibility were seen to increase with decreasing temperature this would indicate that a more open network was forming. The compressibility would then be seen to decrease once the more open network was fully formed. It should also be noted that this would mean the compressibility had a maximum, and therefore it could be a point on a Widom line. If this was in the liquid phase it might suggest that there was another critical point present in addition to the liquid-gas critical point – a liquid-liquid critical point.

Substances with features that suggest that two preferred separation distances exist may exhibit of a liquid-liquid phase transition (LLPT) and liquid-liquid critical point (LLCP). In the past it was assumed that there was not enough structure in liquids to make this possible, but, as will be outlined in Chapter 2, LLPTs separating liquids of differing densities have been detected.

The gradient of the LLPT is important. The Clapeyron equation (equation 1.4) shows that, if the gradient is positive, the denser phase will have the lower entropy, and if the gradient is negative, the denser phase will have the higher entropy. In terms of statistical thermodynamics, a larger entropy corresponds to more microscopic configurations being accessible at that temperature and pressure.

Another aspect of a substance that can be revealing is its dynamic behaviour. In a supercooled liquid the viscosity can either follow the Arrhenius Law and be defined as a *strong* liquid, or it can follow the Vogel-Fulcher-Tamman (VFT) law and be defined as a *fragile* liquid. These laws describe changes in viscosity with temperature at constant pressure. Most liquids follow the Arrhenius Law, written as:

$$\eta \propto e^{\epsilon/kT} \tag{1.5}$$

where η is the viscosity, and ϵ is the energy barrier that a particle must overcome in order to escape from its "cage". An upper bound for ϵ is the latent heat of

vaporisation per molecule.

The Arrhenius Law states that the viscosity diverges when the temperature reaches absolute zero. Liquids which follow the Arrhenius Law show straight lines when the natural log of their viscosity, $\ln \eta$, is plotted against $1/T$.

However, some liquids seem to tend to infinite viscosity before absolute zero. These follow the VFT law, written as:

$$\eta \propto e^{B/(T-T_0)} \tag{1.6}$$

where B is a constant, and T_0 is the temperature at which the viscosity diverges. As this is non-zero, the liquid shows a curved line on a plot of $\ln \eta$ against $1/T$, and a straight line when $\ln \eta$ is plotted against $1/(T - T_0)$.

Cusps in the plots, indicating that the data changes from fitting one equation to fitting the other, mark the crossing of a Widom line. If the change happens gradually, this must occur over a coexistence line, as the presence of both types of liquid prevents a sharp change in the dynamics of the system. Thus an LLPT can be identified using dynamic methods.

As you will read in Chapter 2, not all substances with LLPTs display a density anomaly. For a density anomaly to occur, a certain type of tetrahedral bonding that seems to exist only in water and silica is required. The focus of this thesis is to explore the connection between the density anomaly and the LLPT, shedding light on why some systems with an LLPT exhibit a locus of density maxima while others do not.

$\star$ $\star$ $\star$ $\star$

The thesis is laid out as follows. In the next chapter, Chapter 2, we review the evidence for the existence of LLPTs in some substances, and we review some simple computational models which also exhibit LLPTs, including the two that are focused on in this thesis. In Chapter 3 we study one of these models, Jagla's potential, using cell theory, and see how modifying the potential affects the results.

Chapter 4 outlines the Monte Carlo (MC) simulation techniques used throughout the rest of the thesis, and shows how the results are analysed. In Chapters 5 and 6 Jagla's potential is modified in various ways and the effects on the phase diagram are analysed. In Chapter 7 we look at square-well potentials before concluding the thesis and outlining future work in Chapter 8.

Chapter 2

Background and literature review

The possibility of single-component liquids having two distinct liquid phases separated by a first-order phase transition has been the subject of extensive detailed study over the past few years. Liquid-liquid coexistence often occurs in fluid mixtures [4] and liquid crystals [5], but has only recently been observed in simple pure fluids.

2.1 Experimental and *ab initio* computational evidence

The idea that liquid-liquid phase transitions (LLPTs) may exist in pure fluids can be traced as far back as 1967 [6, 7] when a model was derived to explain why some substances, such as caesium, carbon, water, silicon, iodine, sulphur, phosphorus and selenium, to name a few, have a section of negative gradient on their melting curve when plotted on a pressure-temperature diagram. This negative gradient showed that there were some parts of the phase diagram in which the liquid was of higher density than the solid, such that increasing the pressure on the solid further would cause it to melt.

The model sought to explain these anomalous negative melting curves. It was suggested that the liquid had regions of high- and low-density configurations, and

that, by increasing the pressure, the high-density configurations would increase in size [6]. In this model, the solid also had two differing configurations but it was much more difficult for it to undergo the structural changes required for a transition between them. As a result, the liquid would change its configuration first and become more dense than the solid.

This "two-state" liquid model predicts a transition of width $\delta T \approx T/N$ between the two differing configurations, where N is the number of particles in a domain, or nucleus droplet (see references within [8]). When $k_B T$ (k_B being the Boltzmann constant) is lower than the cluster-cluster interaction energy (that is the free-energy barrier separating the clusters) the clusters are much bigger, i.e. N is much bigger, and a true first-order phase transition exists, marked by a small δT. If, however, this low temperature T is below the glass transition, no true first-order phase transition can exist. This is because amorphous solids are not at a free-energy minimum, and so are not in thermodynamic equilibrium. Also, if this temperature is below the crystallisation temperature, the phase transition is metastable. The distinguishing feature is the size of the free-energy penalty for the coexistence of the two liquids.

Examples of systems with a large free-energy barrier between liquid phases are phosphorus and carbon [9]. For these substances the LLCPs are expected to occur at higher temperatures than the crystalline phase, and so the LLCPs are stable. In contrast, water falls into the bracket of having an intermediate free-energy barrier between the liquid phases [9]. It follows that the LLCP is predicted to fall below the melting line, and is therefore metastable with respect to the solid. It is therefore much harder to identify the LLCP and LLPT. Despite this, some evidence does exist. The experimental evidence supporting the existence of LLPTs in these elemental liquids, and a few others, is outlined below.

2.1.1 Phosphorus

Perhaps the most compelling evidence for an LLPT is to be found in the phase diagram of phosphorus. The possibility of an LLPT was suggested by the observation of a point of maximum temperature in its melting curve at a temperature of around 1300 K and a pressure of around 1 GPa [10]. Compare this with a typical phase diagram (figure 1.1) where the solid-liquid coexistence line has a

positive gradient throughout. The region where the melting curve of phosphorous has a negative gradient is where the liquid is of higher density than the solid, suggesting another structure in addition to the known tetrahedral P_4 molecules. The authors pursued this possibility and found a polymeric form of liquid phosphorus at pressures above 1 GPa. Their x-ray diffraction studies showed a sharp change in radial distribution function over a pressure change of only 0.02 GPa, in which both forms of the liquid existed. This strongly suggests a first-order phase transition. A subsequent experimental paper extended the coexistence line [11]. Its authors added the previously known liquid-gas coexistence line of the molecular P_4 liquid to the phase diagram, and saw that, as the liquid-gas critical point lay at 968K, 8.2MPa, a much lower pressure than the proposed LLPT, the polymeric liquid was actually in coexistence with a molecular fluid.

2.1.2 Carbon

Carbon has been shown to have a maximum temperature of 4790 K in its melting curve at 5.6 GPa, accompanied by a change in the gradient of the plot of electrical resistivity against pressure at the same temperature and pressure [12]. Together, these suggest an LLPT between two different structures. Atomistic simulation methods carried out by Glosli and Ree [13] calculated the melting curve maxima (graphite-liquid-liquid triple point) to be 5133K, 1.88 GPa, from which a liquid-liquid phase transition extended, ending in a critical point at 8800 K, 10.6 GPa. However, a later *ab initio* study showed that this was not the case, and that the original method had been unable to adequately describe the complex electrionic behaviour of liquid carbon [14].

2.1.3 Water

The proposed LLPT in water is predicted to be deep within the supercooled region of its phase diagram. Despite this there are clues to its existence.

Water's anomalies

The first clues to a possible LLPT in water are its many anomalies in the stable liquid region.

As we all know, ice floats on water. This shows that ice is less dense than water, and therefore its melting curve must have a negative gradient on a pressure-temperature plot. As with the substances previously discussed, this suggests that there is competition between configurations of differing local density.

Also well known is the fact that water has a maximum density at 4°C at atmospheric pressure. This maximum density implies that there is competition between local structures of differing density within the liquid. The top left graph in figure 2.1 shows how the density-temperature plot of water differs from that of "normal" liquids. Linked to this is thermal expansivity α (equation 1.1), which is negative below 4°C while most liquids maintain positive values, as shown in the top right graph of figure 2.1.

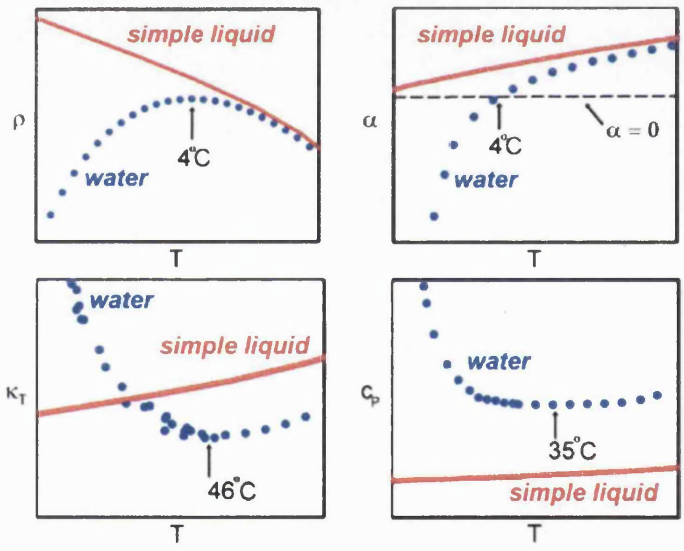

Figure 2.1: Schematic graphs comparing the behaviour of water with that of a simple liquid. Plotted against temperature at constant pressure are density ρ, thermal expansivity α, isothermal compressibility κ_T and isobaric specific heat capacity C_P. Figure reproduced from [15].

The specific heat at constant pressure C_P (equation 1.3) has an anomalous minimum at 35°C (as seen in the bottom right graph of figure 2.1) and increases

rapidly as temperature is lowered further, tending towards infinity around $-45°C$ (determined through entropy considerations [16]), but this is below the homogeneous nucleation temperature of $T_H = -38°C$ – the temperature at which crystal phases nucleate spontaneously throughout the whole liquid, causing it to freeze [17] and making experimental study below this difficult.

Water's isothermal compressibility κ_T (equation 1.2) has an anomalous minimum at 46°C as shown in the bottom left graph in figure 2.1. As temperature decreases further, κ_T increases, suggesting that a more open structure has come into play. It appears, through curve-fitting and extrapolation, that κ_T may also tend to infinity around $-45°C$ [17, 16].

Theories of the origins of the anomalies

There are three main theories to explain the anomalies in water. The first theory, proposed by Speedy [18] in 1982, is known as the **stability limit conjecture**. It predicts that the liquid spinodal line meets the line of TMD at a negative pressure[1] and therefore (through thermodynamic arguments) the spinodal line's gradient on the pressure-temperature plane changes sign and it bends back into positive pressure at low temperatures to become metastable with respect to the solid at low temperatures. A schematic of this can be seen in figure 2.2(a). As the response functions are predicted to become singular at the spinodal line, this scenario would explain the anomalies described above.

In 1992, Poole *et al.* suggested another possibility: that there existed a **second critical point** [20]. At first thought to be between two amorphous solids, and later regarded as being between two liquids of different density, this second critical point would be accompanied by singularities in the response functions, giving another explanation for the unusual behaviour of the specific heat capacity and the isothermal compressibility of stable liquid water. The second critical point would separate two phases of differing density, the competition between which would be the cause of the density anomaly. The authors predicted that the spinodal line would not retrace (i.e. change gradient and tend back towards

[1] Negative pressure can be produced in physical experiments. If a fluid is held in a cylinder with a piston at one end, the piston can be pushed in to create positive pressure (its magnitude given by force per unit area of the piston), or pulled out to create negative pressure.

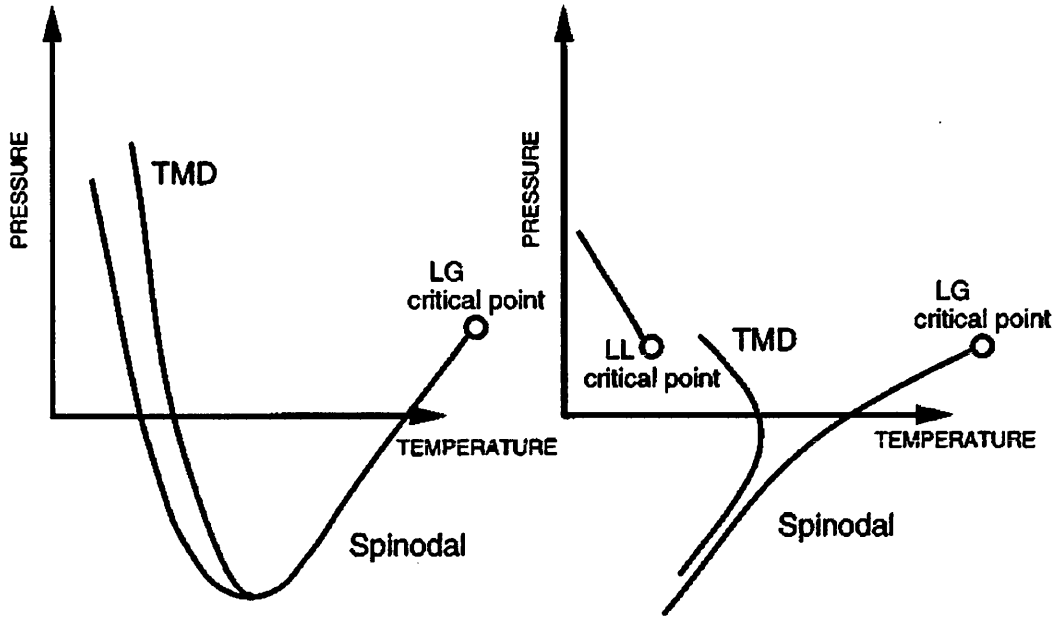

Figure 2.2: Schematic representations of **(a)** the stability limit conjecture, and **(b)** the second critical point scenario. The line meeting the liquid-liquid (LL) critical point represents a liquid-liquid phase transition (LLPT) while the lines meeting the liquid-gas (LG) critical point are spinodal lines. Diagram reproduced from [19].

positive pressures), and that the TMD line would change direction and would be of positive gradient at negative pressures and so would not meet the spinodal. A schematic demonstrating this theory can be seen in figure 2.2(b).

In a third theory, known as the **singularity-free scenario** [19], it was shown through thermodynamic analysis that the maxima in the response functions could be a direct result of the line of TMD. The theory suggests that the competition between two local configurations of differing density is enough to produce all the anomalies seen in liquid water, and that the system can move smoothly from one prevalent configuration to the other without a first-order phase transition. Hence there are no singularities, and the response functions always remain finite, eventually rounding off to a maximum. The phase diagram would look much like that for the second critical point scenario (figure 2.2(b)) except that the LLPT would be replaced by a region of sharp but continuous changes in density.

The evidence supporting the various theories

Speedy's stability limit conjecture concluded that the liquid spinodal line, $P_S(T)$, must retrace because thermodynamic arguments (see references within [20]) state that there must be a minimum in $P_S(T)$ where it meets the TMD line. As experiments showed the TMD line had a negative gradient when plotted in the pressure-temperature plane (see figure 2.2(a)), and the spinodal line a positive gradient, Speedy predicted that the two lines would meet in areas of negative pressure. As a result, the spinodal line would re-enter positive pressure in the metastable region of the phase diagram. This theory was highly regarded, as the presence of the spinodal line at low temperatures would explain water's anomalies.

However, an experimental study using x-ray scattering performed near the proposed spinodal line [21] did not show correlation lengths of density fluctuations increasing with decreasing temperature, a phenomenon that would be expected near a spinodal line. The authors therefore suggest that there is no spinodal point, and that the increased density fluctuations are due to an increased fraction of water molecules participating in clusters, a proposition that is in line with the singularity-free scenario.

Thus the spinodal line theory became superseded by the second critical point theory and the singularity-free theory, both of which were supported by the identification of two distinct amorphous solids: while a low-density amorphous solid, LDA, had been formed from liquid water in 1980 (see references within [17]), a high density amorphous solid, HDA, was formed from compressing ice in 1984 [22]. HDA has been reversibly changed into LDA, and vice versa. The change is accompanied by a volume change greater than 20%.

Poole *et al.* simulated an accurate model of water, ST2 [20]. Their simulations showed the line of TMD curving round and becoming of positive gradient in the negative pressure area of the phase diagram, and thus never intersecting the spinodal line. The same simulations also identified a second critical point terminating a line of coexistence. The authors speculated that this represented a transition between LDA and HDA.

Four years later, in 1996 [19], Sastry *et al.* showed, through thermodynamic arguments, that a locus of compressibility extrema was a thermodynamic conse-

quence of a density maximum. Their lattice model demonstrated the competition between stronger "hydrogen" bonds forming regions of lower entropy, and weaker "non-hydrogen" bonds forming regions of higher entropy. Whilst it produced a line of TMD and compressibility extrema, it did not demonstrate a second critical point.

But it is only through experimental evidence that it will be possible to tell which of the two scenarios actually applies to water. What distinguishes the two theories is whether the phase transition between the HDA and LDA phases is first-order or not. Given the metastable, non-equilibrium nature of amorphous ice, one must be careful when talking about first-order phase transitions, but a lot of work has gone into showing whether the HDA-LDA transition is discontinuous or continuous. In 1985, Mishima *et al.* [21] were startled by a 26% change in density over a very small change in pressure (about 0.9 GPa), and suggested that the transition from HDA to LDA appeared to be discontinuous. In a later study, neutron diffraction studies [23] showed that intermediate states have structure factors[2] that are a superposition of initial and final stages. However, the HDA must first be annealed. Other studies could not find any amorphous solid that had a structure factor that was a superposition of those of other amorphous solids, and therefore concluded that the HDA-LDA transition is continuous [24]. But a third study [25], using Raman spectroscopy, identifies a phase boundary – that is, a region containing a mixture of both phases – that grows narrower with increasing temperature, strongly suggesting that the HDA-LDA phase transition is discontinuous.

A great deal of work has also focused on demonstrating that these amorphous phases are connected to liquid phases. It has been shown through neutron scattering experiments in 1995 that LDA is structurally similar to water cooled at low pressures, while HDA is structurally similar to water cooled at high pressures (see references within [17]). Although the glass transition point of HDA has not been identified, LDA has been heated and transformed into a viscous liquid at its glass transition of 130 K. Given the connection between the amorphous solid and the liquid, the search for the second critical point has shifted to supercooled water.

[2]The structure factor of a substance is a mathematical description of the way that the substance scatters particles. It is the Fourier transform of the radial distribution, calculated in Section 4.3.1.

This search has been hampered by the prediction that if an LLCP were to exist, it would occur between the homogeneous nucleation temperature, T_H, and the crystallisation temperature, T_X. T_H is the temperature below which supercooled water freezes, and T_X is the temperature above which amorphous ice crystallises. But despite this, the continuity of the amorphous-to-liquid transition means that it is possible to plot the Gibbs free energy[3] landscape by extrapolating from experimental data obtained from the metastable decompression-induced melting curves of high pressure ice [26]. Such extrapolations suggest that there may be an LLPT, emanating from the HDA-LDA transition, that terminates in a critical point at 0.1 GPa and 220 K. Also, the metastable decompression-induced melting curve showed an abrupt change at the proposed line of LLPT, suggesting that the crystal melts to phases of differing density. But it is impossible to say if the liquid phases change continuously into each other, or if the change is discontinuous and there is a line of coexistence of the two liquids.

Very recently, a study on confined water examined its dynamical behaviour [27]. It identified a cusp-like fragile-to-strong dynamic transition, as would be expected along a Widom line. Along a line of coexistence, the transition would be expected to be smooth due to the presence of both types of liquid at the line. Thus, the point where the fragile-to-strong transition became smooth is tentatively put forward as the LLCP, at 1600 ± 400 bars[4], and 200 ± 10 K.

So, although not conclusive, the experimental evidence is pointing towards the second critical point scenario. In addition, all the water-specific computational studies support the second critical point scenario. Figure 2.3 shows the stable fluid and crystalline phases of the SPC/E model and the TIP4P model compared with experimental evidence. The similarities are striking. It is therefore significant that both these models display an LLPT and LLCP [28]. Also the accurate ST2 and TIP5P models display both LLPTs and LLCPs. The phase diagrams are displayed in figures 2.4 and 2.5. Note how the gradient of the LLPT is negative (i.e. $dP/dT < 0$), showing, through the Clapeyron equation (equation 1.4), that the higher density state has higher entropy. Another interesting prediction of the ST2 model is a return to normal behaviour at cold temperatures with the appearance of a density minimum [29]. The line of density maxima turns into a line of density minima.

[3]Gibbs free energy is given by $G = U + PV - TS$ where U is the internal energy, P is the pressure, V is the volume, T is the temperature and S is the entropy.

[4]1 bar = 10^5 Pa

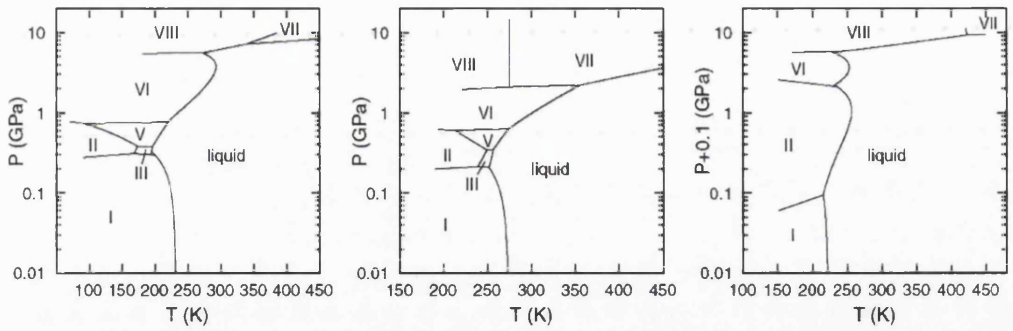

Figure 2.3: Phase diagram of stable phases of H_2O. Left: simulation results of the TIP4P model. Middle: experimental results. Right: simulation results of the SPC/E model, with coexistence pressures shifted up by 0.1 GPa to include results for ice I. Diagram reproduced from [30].

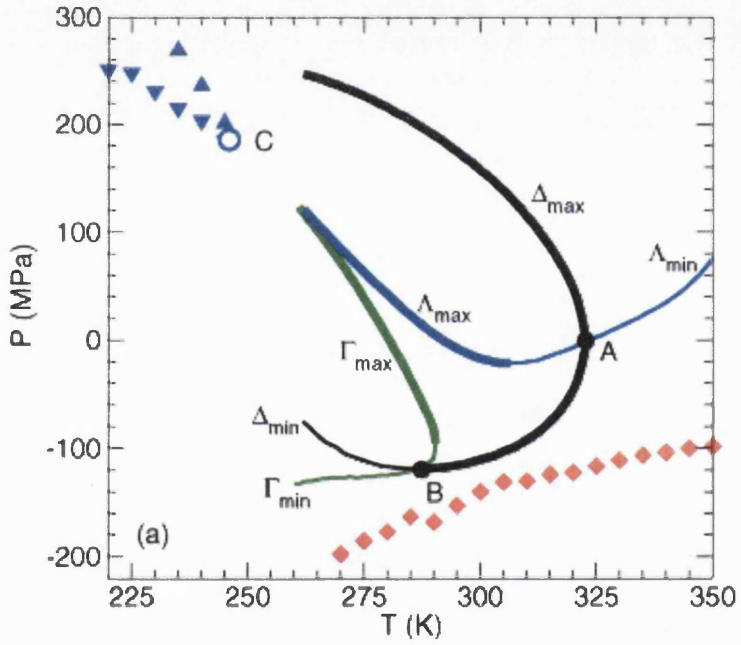

Figure 2.4: ST2 model. Location of the LLCP (C), LDL spinodal (up-triangles), HDL spinodal (down-triangles) and liquid-gas spinodal (diamonds), density extrema (Δ), isothermal compressibility extrema (Λ), and isobaric specific heat capacity extrema (Γ). Reproduced from [29].

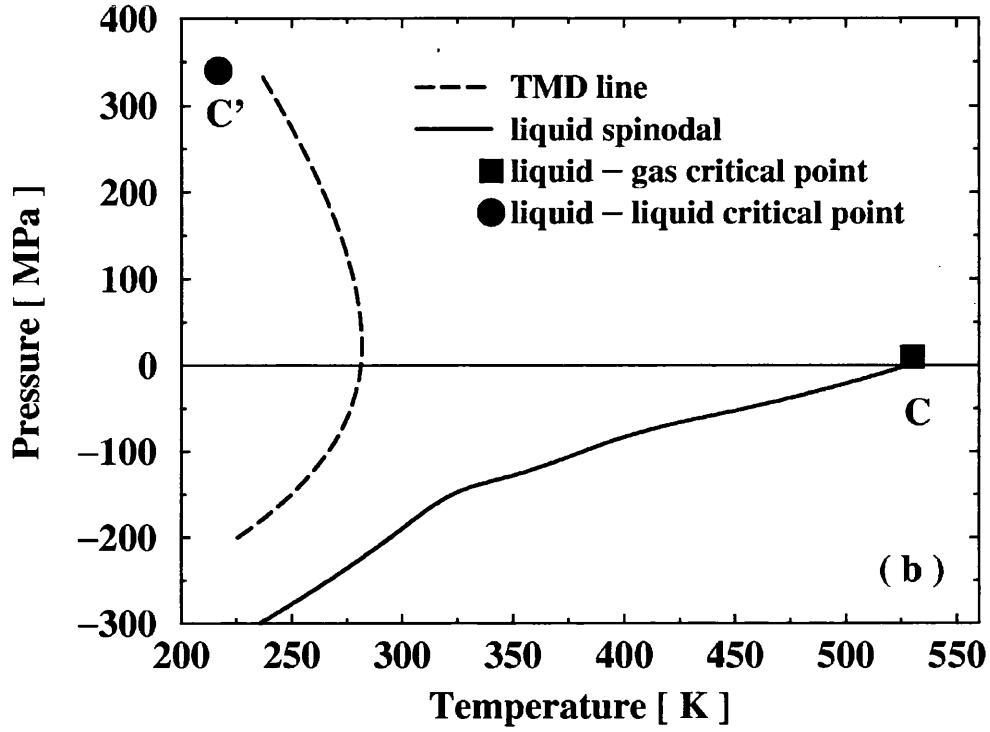

Figure 2.5: The phase diagram of the TIP5P model. The liquid-gas critical point, C, is marked by a square, and the liquid-liquid critical point, C', is marked by a circle. Reproduced from [31].

A simple lattice model adds further computational evidence supporting the second critical point scenario [32] as it suggests that if the average H-O-H angle in water molecules is constant over time then an LLPT must exist. Therefore, as experiments show that the H-O-H angle has a well-defined value, the authors suggest the singularity-free scenario cannot occur.

Another finding suggesting that more than just a smooth transition between low density liquid (LDL) and high density liquid (HDL) might be occurring, is that enzymes stop working below $-53°$C, 1kbar, when water is still liquid due to being confined. This is very close to the predicted location of the proposed critical point [32].

2.1.4 Silica

Silica also has a density anomaly, suggesting the existence of an LLPT. The density maximum is much less sharp than that of water. It is thought that the water and silica density anomalies are due to expanded tetrahedral networks that are formed at low temperatures. The water maximum is sharper due to a near-straight intermolecular O$\cdots$H-O bond, while the equivalent silica bond (Si-O-Si) is at an angle of 144° [33]. It should also be noted that the density maximum in water gets flatter with increasing pressure due to the O$\cdots$H-O bond angle decreasing with pressure.

It has also been observed that silica has a density minimum in the glassy phase. It was often predicted that, once all the tetrahedral networks had formed, the system would return to normal behaviour, after passing through a density minimum. This was observed in silica when its Si-O-Si bond angle was at a maximum [34].

Molecular dynamics simulations of silica show anomalous trends in isothermal compressibility, as were seen in water. The line of κ_T maxima forms a negatively-sloped line in the P-T plane, and the maximum increases in magnitude as temperature decreases, as also demonstrated by water simulations [35].

Polyamorphism (the presence of more than one amorphic solid) has been observed both through experiments and through simulations (see references in [36]), and an LLPT has been found in two computational models of silica [36], also with a

negative gradient.

Also observed in computational studies [37, 38] is a fragile-to-strong transition which is associated with a Widom line extending from the proposed liquid-liquid phase transition.

2.1.5 Other systems

Many other systems also show signs of first order liquid-liquid phase transitions. For example, there is experimental evidence of a transition from a supercooled liquid to an amorphous solid of a different liquid in triphenyl phosphite, strongly suggesting that the molecular liquid has an LLPT in a supercooled state [39].

Selenium, as well as showing a maximum in its melting curve as previously mentioned [40], demonstrates a first-order semiconductor-metal transition terminating in a critical point [41].

Iodine demonstrates three liquid phases separated by sharp changes in conductivity in one case, and volume in the other [40].

Other systems also show signs of LLPTs including n-butanol, sulphur, and silicon. All the substances mentioned have pressure- and/or temperature-induced structural changes in common. However, water and silica are apparently unique in demonstrating density maxima away from the phase transition. In this thesis the connection between density anomalies and the LLCP will be studied.

2.2 Simple computational approaches

There are many *ab initio* molecular dynamic models of substances which accurately reproduce their structure and phase diagrams: for example, the ST2 model of water (a rigid four-point-charge model [42]) mentioned in Section 2.1.3, and the models of silica mentioned in the referenced papers in Section 2.1.4.

Despite the success of these models, there has been a drive for simpler models.

These simpler models have the ability to isolate the features that produce a given phenomenon. They are also much less computationally intensive and so many more parameters can be explored.

2.2.1 Lattice-based and orientation-dependent models

A variety of lattice-gas models encourage particles to sit at next-nearest neighbour distance from each other, and discourage particles from sitting on the closest lattice points to each other [43, 44]. And other lattice models favour particles sitting at specific orientations to each other [45], and again discourage over-filling of the lattice [46, 47]. These models produce the competition between a less dense, energetically-favourable configuration and a more dense, higher-energy configuration, and display density anomalies. Some also display LLPT and LLCP. The models are well suited to studying how the geometry of the lattice (and therefore orientation of the bonds) and the relative strength of the bonds affect the phase diagrams.

As mentioned in Section 2.1.3, one lattice-gas model [32] had a variable that could change the extent to which the angle of the intra-molecular H-O-H bond was self-correlated, reducing the energy when two bonds of a particle were at the correct orientation. When its designers removed the energy advantage, the singularity-free scenario was obtained. As experiments have shown that the H-O-H bond has a well-defined angle, this demonstrated that the singularity-free scenario is not consistent with experiments, adding weight to the LLCP hypothesis.

Some off-lattice models promote the bonding of atoms at certain orientations and distances and discourage atoms from coming close to each other [48]. These models also demonstrate LLPT, LLCP and density anomalies.

2.2.2 Off-lattice isotropic models

Hemmer and Stell

It was through using a lattice model that Hemmer and Stell [49] suggested the possibility that an isotropic potential could produce an extra phase transition over and above the liquid-gas transition. After using symmetry arguments on a lattice, they moved on to a continuous system. In this thesis we also focus on off-lattice, continuous systems.

Hemmer and Stell calculated the equation of state for a one-dimensional continuum fluid defined by an inter-particle pair potential. Pair potentials (or interaction potentials) define the potential energy felt by two particles over a range of separation distances. A pair potential with a hard core[5] followed by an attractive part[6] produces one phase transition. Hemmer and Stell demonstrated that by introducing a softening ramp to the pair potential (see figure 2.6) they could induce a second transition. The second critical point was always of higher density and lower temperature than the first. The authors varied the parameters of the pair potential used (known as a ramp potential), and found that increasing the height of the ramp would decrease the temperature and increase the pressure of the second critical point. Reducing the range of the ramp was also found to decrease the temperature and increase the pressure of the second critical point. The pressure was seen to tend to infinity when the ramp was removed altogether.

A pair potential with the hard core softened this time by a square shoulder (that is, a section of the pair potential with a finite repulsion, constant with increasing separation) was shown to have a similar phase diagram. It was shown to have an extra phase transition in a one-dimensional study, and a three-dimensional study showed the presence of a solid-solid transition [50].

Pair potentials where the hard core is softened in some way (for example by a ramp or a square shoulder, as in the cases above) are known as *core-softened* potentials. Largely used to study the phenomenon of LLPTs, they have also been

[5]Hard cores are modelled by setting the potential energy to infinity for particles whose separation is less than the hard core's diameter.

[6]Attractive parts of the pair potential are at separation distances where particles experience negative potential energy.

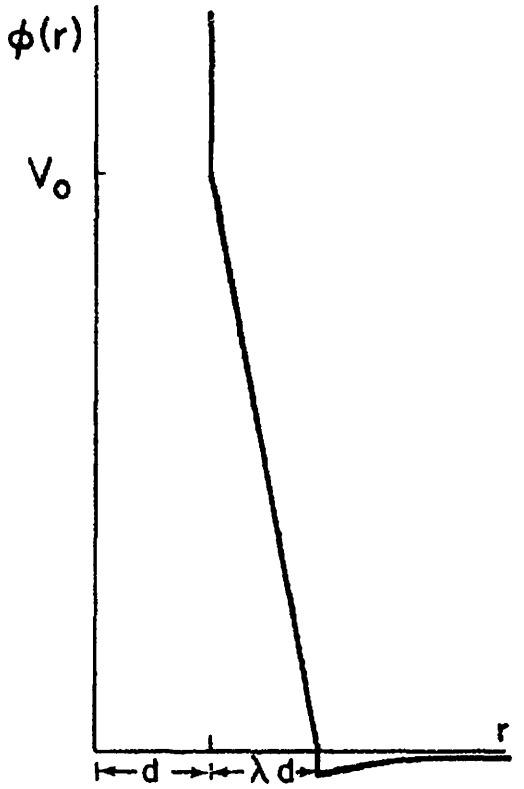

Figure 2.6: The Hemmer-Stell potential, reproduced from [49]. $\phi(r)$ is the potential energy felt by two particles whose centres are separated by distance r. Each particle has a hard core of diameter d, which, if penetrated by another particle will result in infinite potential energy, ϕ. This hard core is *softened* by a ramp that is still repulsive but to a finite extent. The ramp is the section of the pair potential where increasing the separation of the particles will cause their potential energy to decrease linearly.

used to mimic colloidal systems of magnetic particles in magnetic fields [51], and have exhibited stripe phases in two-dimensional studies [52]. But here we will focus on the models that display density anomalies, LLPTs, or both.

Lennard-Jones with outer Gaussian minimum

A smooth potential consisting of a Lennard-Jones potential with an outer Gaussian minimum was shown to have a water-like density anomaly and diverging compressibility in a two-dimensional study [53], prompting suspicions of a metastable LLPT. But when this potential was studied further [54] it was found that the anomalies were due not to an LLPT after all, but to the emergence of low-density crystal structures within the fluid phase as the temperature was lowered and the system went through a quasi-continuous phase transition to the lower density crystal. Furthermore, when studied in three dimensions [55], no anomalies were present; nor was an LLPT. However, a solid-solid phase transition was identified [56].

Square well potentials

A class of potentials where the hard core is softened by a square shoulder, and the attractive part takes the form of a square well (a discrete section of the pair potential with negative potential energy, constant with increasing separation), has been studied extensively [57, 58, 53, 54, 59, 60, 61]. Potentials with the form shown in figure 2.7 (which is a discrete version of the smooth potential mentioned above) have been studied in one, two and three dimensions. In one and two dimensions, lines of density maxima and compressibility maxima were displayed [58, 53]. However, the results of the square potential were qualitatively similar to those of the smooth potential mentioned above [53], which were shown not to be linked to an LLCP [54]. Also, in three dimensions the anomalies did not exist [61].

Other studies focused on a class of square potential that had a softening shoulder of positive energy. For one particular parameter set, for which the graph is drawn in figure 2.8, two studies were carried out: one using molecular dynamics (MD) [59] and the other using Gibbs Ensemble Monte Carlo (GEMC) [60].

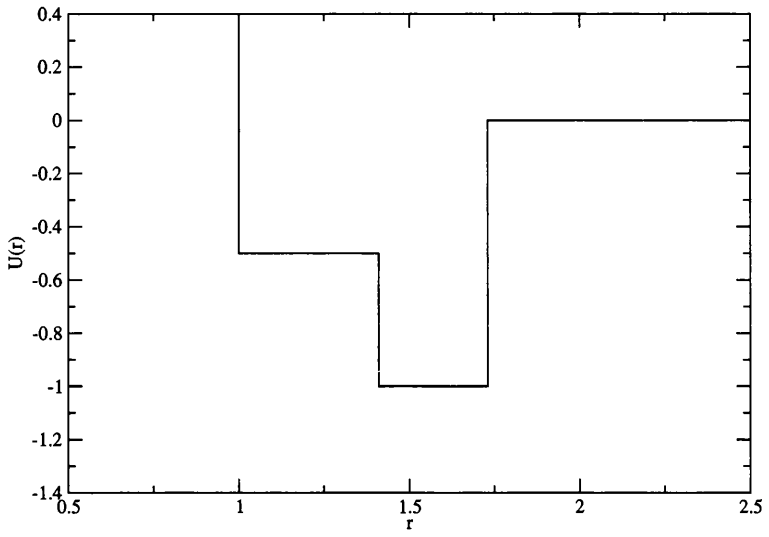

Figure 2.7: An example of the type of potential studied in [61].

The results of the studies were very close, both qualitatively and quantitatively, validating the results as real and not artifacts of the simulation technique. The results showed that there was a second phase transition in the fluid region, albeit metastable with respect to the solid, but the authors did not identify a line of density maxima. In Chapter 7 we study the potential using a third technique.

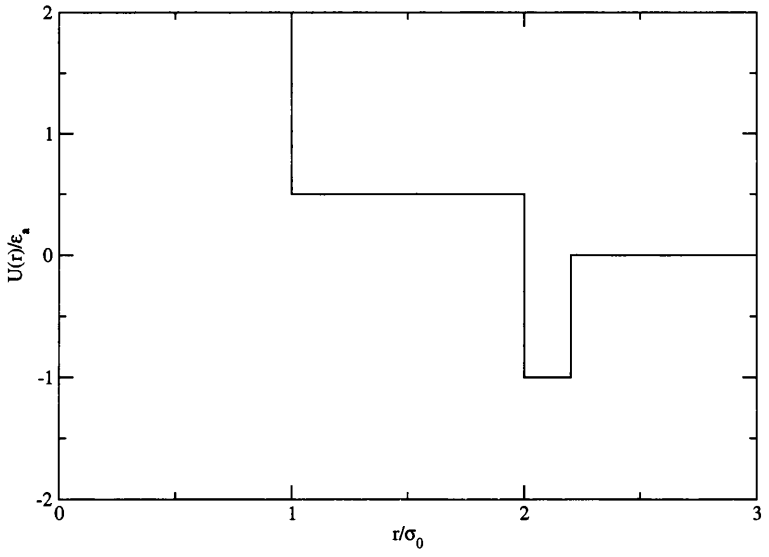

Figure 2.8: The square interaction potential studied in [59, 60].

Skibinsky *et al.* [57] did a series of studies varying the dimensions of the square well potential. They found that increasing the well width or shoulder width would move the LLCP (higher density critical point) to lower density and pressure, and

to higher temperature. Increasing the shoulder height had limited effect on the density of the LLCP but did decrease its temperature and increase the pressure at which it occurred. None of the systems was reported to have density anomalies. The high density critical point for the fourth potential they used is studied using our method in Section 7.5 of this thesis.

Ramp potentials

Jagla looked at the ramp version of the Stell and Hemmer potentials. In his first study [62], which was two-dimensional, the potential only had a hard core and ramp section, and did not have an attractive element. As a result (see references within [62]), it did not have a liquid-gas phase transition, but instead a continuous fluid. Using Monte Carlo in the constant-NPT ensemble (where the number of particles, pressure and temperature are kept constant, while energy and volume are allowed to fluctuate), he demonstrated that the fluid-solid coexistence line had a negative gradient and that melting resulted in a reduction in volume. He also located a temperature of maximum density along an isobar in the fluid region, and multiple crystalline states in the solid region.

In a later paper [63] he again used Monte Carlo in the constant-NPT ensemble to study the same potential in three dimensions. This time, as well as a maximum density he also identifed a maximum in compressibility as a function of temperature. He then added a long-range Van der Waals attraction, in the form of a global term per particle, proportional to $-\gamma/v$ where γ is the total integrated strength of the attraction and $v = V/N$ is the specific volume, thus obtaining a liquid-gas phase transition and associated critical point. When the strength of the attraction rose above a certain value, a second critical point appeared at T=0. This was metastable relative to a variety of crystalline structures, but enough data was gathered just before crystallisation. Increasing the strength further moved it into finite temperature, although still metastable. The loci of anomalies in density and κ_T also moved with changing γ, and the line of K_T maxima always ended at the critical point. The line of density maxima turns into a line of density minima.

In a third paper on ramp potentials, Jagla added an attractive well explicitly to the potential [2], as shown in figure 2.9. He began the study in two dimensions.

This time both the liquid-liquid and liquid-gas critical points, and associated phase transitions, were stable. The LLPT had a positive gradient in the pressure-temperature plane, and the line of TMD was seen to connect with it below the critical point. Again a variety of crystalline structures were present. Both the liquid phases were seen to be denser than the solid.

In three dimensions, the LLCP and locus of TMD were also present and stable. Studying the structure factor of the two coexisting liquids at the LLPT revealed that the prevalent inter-particle distance was the hard core diameter (r_0) for HDL and the minimum of the potential (r_1) for LDL.

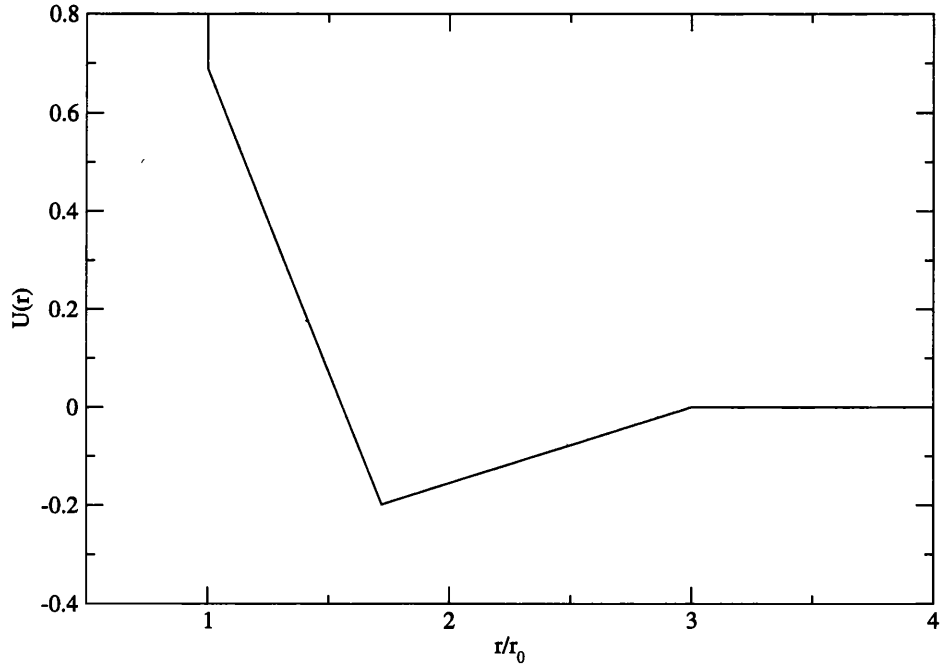

Figure 2.9: Jagla's interaction potential with attractive element [2]. The potential Jagla used in three dimensions is shown. The parameters of the potential he used in the two-dimensional experiments were slightly different.

Wilding and Magee did further work on the ramp potential that Jagla had used when he was working three dimensions [54]. They confirmed the existence of the LLCP and TMD, and also found the liquid-gas critical point (LGCP). They calculated sections of the line of coexistence for each critical point, and found that they both had a positive gradient in the pressure-temperature plane. This

differs from water, where it is predicted that the LLPT has a negative gradient. Jagla's model, by the Clapeyron relation (equation 1.4), must therefore generate an LDL with higher entropy than the HDL, which is the reverse of water. In addition, later studies [64, 65], using molecular dynamics, show that in Jagla's model HDL is Arrhenius (strong) while LDL is non-Arrhenius (fragile). This, again, is the reverse of water. The authors suggest that the entropy of the phase determines its viscous behaviour, rather than the density. The less ordered phase in both water and the Jagla model is fragile, while the more ordered phase in both cases is strong.

The locus of TMD was seen to point towards the critical point, and the isothermal compressibility, κ_T, was seen to tend to infinity in its vicinity.

As the model features both a stable LLPT and a line of TMD, it is a very interesting tool for studying how density maxima relate to LLPTs. As such, it forms the focus of our investigations.

Chapter 3

Lennard-Jones-Devonshire cell theory

3.1 Theory

The Lennard-Jones-Devonshire cell theory is a form of mean field theory, and is a quick way of obtaining a feel for a phase diagram. A liquid state is modelled by considering a lattice of spherical cells. Each cell is occupied by one particle which can move within the cell independently of all the other particles. Thus it is possible to consider a single cell of radius s, volume v, and its interactions with its c nearest neighbours that are "smeared" around the surface of a larger concentric sphere, whose radius a is given by $a^3 = \gamma v$, where $\gamma = \sqrt{2}$ for an FCC (face centred cubic) lattice for which $c = 12$. See figure 3.1(a) for a two-dimensional representation of this.

For each temperature and pressure the minimum of $G(V)$, the Gibbs free energy, is found, thus identifying the density of the system. Lines of coexistence appear as lines of discontinuities on the density surface, and can be calculated exactly by finding the temperature and pressure that give $G(V)$ two minima of equal depth.

$$G(V) = -k_B T \ln v_f \sigma_c + E_0/2 + PV \tag{3.1}$$

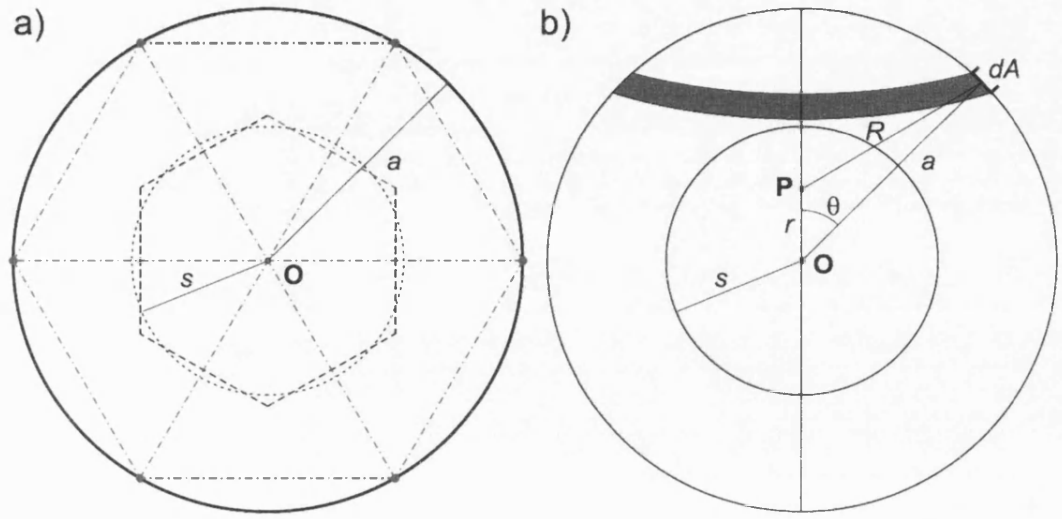

Figure 3.1: **(a)** The inner, dotted, circle represents the cell of radius s and volume v. The overlaid dashed hexagon is of the same volume and represents the primitive unit cell. The FCC lattice is represented by the dot-dashed lines, with lattice sites as vertices. The effects of the nearest neighbours are "smeared out" over the solid outer circle of radius a that joins the lattice sites surrounding the central lattice site (marked with **O**). **(b)** The geometry showing how the separation R between a particle at position **P** and an element of the shell dA can be calculated. The particle is at radius r from the centre of the cell **O**, while the shell is at a radius a. The angular coordinate of the shell element is θ. The diagram is reproduced from [66].

where $\sigma_c = e$ (see references within [66]). E_0 is the energy the system would take if all particles were on their lattice sites; that is, the distance from one particle to the next is exactly a, so $E_0 = cU(a)$ where $U(r)$ is the potential energy between particles of separation r. v_f is the "free volume" given by

$$v_f = \int_v \exp\{-[E(\mathbf{r}) - E_0]/k_B T\} d\mathbf{r} \tag{3.2}$$

where $E(\mathbf{r})$ is the interaction energy of a particle at position $\mathbf{r}$. In figure 3.1(b) the cell geometry is shown. By radial symmetry it is possible to reduce $E(\mathbf{r})$ to $E(r)$ where r is the radial coordinate of the particle's position. First, simple trigonometry calculates the separation R between the particle at position $\mathbf{P}$ and a section of the shell, $d\mathbf{A}$, thus:

$$R^2 = r^2 + a^2 - 2ar\cos\theta \tag{3.3}$$

Then, as c particles are smeared over the shell, $E(\mathbf{r})$ can be written as

$$E(r) = c\frac{\int_{shell} U(R) dA}{\int_{shell} dA} = c\frac{2\pi a^2 \int_0^\pi U(R)\sin\theta d\theta}{4\pi a^2} \tag{3.4}$$

Employing this method it must be stressed that we will only get a general feel for the phase diagram as the model is very crude and is known to overestimate critical temperatures because it does not allow the volume to fluctuate [66].

3.2 Results using Jagla's potential

We used the above model using Jagla's ramp potential [2] as our definition of $U(r)$, thus defining the interaction energy between particles of separation r. The interaction potential was shown in figure 2.9 and is defined thus:

$$U(r) = \infty \quad \text{for} \quad r < r_0 \tag{3.5}$$

$$U(r) = \epsilon_0(r_1 - r)/(r_1 - r_0) - \gamma(r_2 - r)/(r_2 - r_0) \quad \text{for} \quad r_0 \leq r < r_1 \tag{3.6}$$

$$U(r) = -\gamma(r_2 - r)/(r_2 - r_0) \quad \text{for} \quad r_1 \leq r < r_2 \tag{3.7}$$

$$U(r) = 0 \quad \text{for} \quad r > r_2 \tag{3.8}$$

where r_0 is the diameter of the hard core (and the unit of distance), r_1 is the separation of minimum energy, $r_2 > r_1$ and the attraction intensity $\gamma > 0$. Temperature is measured in units of ϵ_0/k_B and pressure is measured in units of $\epsilon_0/{r_0}^3$. Jagla used the parameters $r_1 = 1.72\ r_0$, $r_2 = 3.0\ r_0$ and $\gamma = 0.31\ \epsilon_0$.

Figure 3.2 shows the temperature-pressure-density plot obtained. There are three phases, each separated by a line of coexistence that appears as a large jump in the density-surface of the plot in figure 3.2. The radial symmetric cell potentials of each phase are plotted in figure 3.3. In the high-density phase the cell potential has a deep minimum at zero separation, suggesting that most particles are on their lattice sites. In the intermediate-density state a shallow minimum is some way out from the lattice site, suggesting particles are usually slightly displaced from their lattice site. In the low-density phase the shallow minimum is at the very edge of the cell, suggesting that in this phase the particles are usually far from their lattice sites.

Identifying the phases is not trivial. At first glance, given the results of Jagla [2] and Wilding and Magee [54], we would expect these phases to be HDL, LDL and gas. However, the study of the Lennard-Jones potential using the same cell theory [66] also found three phases. Given what is known about the phase diagram of the Lennard-Jones fluid it was natural to assume that the three phases were solid, liquid and gas. However, despite being forbidden by symmetry in real systems, the solid-liquid line of coexistence ended in a critical point. This could have been a consequence of the cell theory: as the theory is lattice-based, there may well be a point where a liquid has the same symmetry as the solid, and can therefore be indistinguishable from a solid. On the other hand, perhaps it was not a solid, but a very dense liquid, and the second phase transition was an artifact of the cell theory.

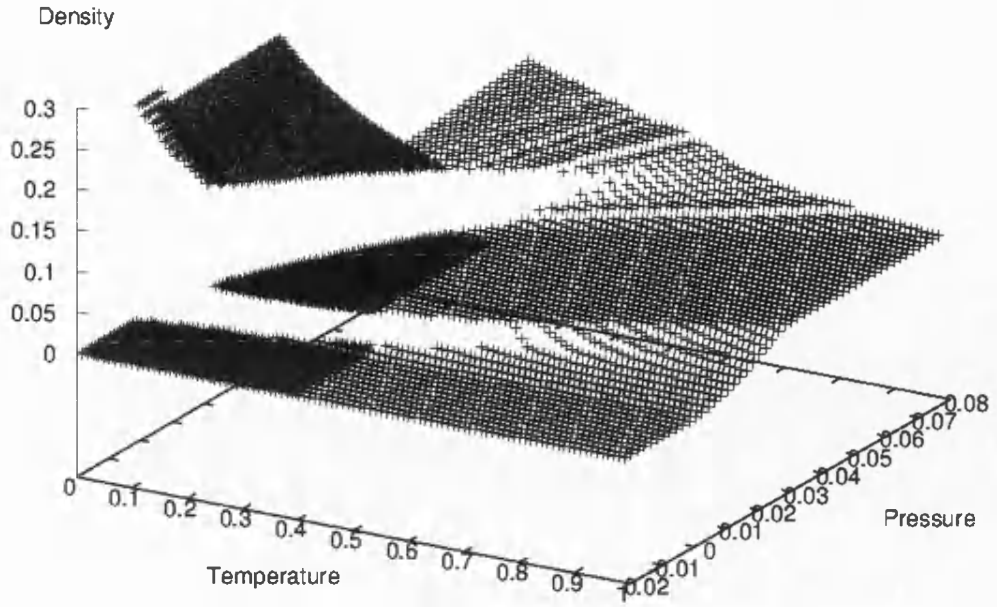

Figure 3.2: The temperature-pressure-density plot of the results of the cell model when using the pair potential described by equation 3.5.

So, given that the cell theory applied to the Lennard-Jones potential produces two critical points, the appearance of two lines of coexistence using Jagla's potential must be treated with caution.

If the two phase transitions seen are indeed an LLPT and a liquid-gas phase transition (LGPT), then we could look in the LDL phase to see if the density anomaly is displayed. However, we saw no such anomaly. Indeed, a T-ρ projection of the plot in figure 3.2 is in figure 3.4 and shows that the LDL phase is totally flat. Looking at the $G(\rho)$ plots for this phase (figure 3.5) reveals why. The minimum is very sharp – instead of a point of zero gradient it has a cusp. The value of the density at this cusp does not change with pressure or temperature, hence the unchanging density in this phase. The cell model does not reproduce the density anomaly seen using the Monte Carlo techniques of Jagla, and Wilding and Magee.

Quantitatively the results of the two techniques differ also. As the temperature-pressure-density plot (figure 3.2) shows, the high density critical point occurs at $T \approx 0.49$ and $P \approx 0.06$. Compare this with the Monte Carlo simulation

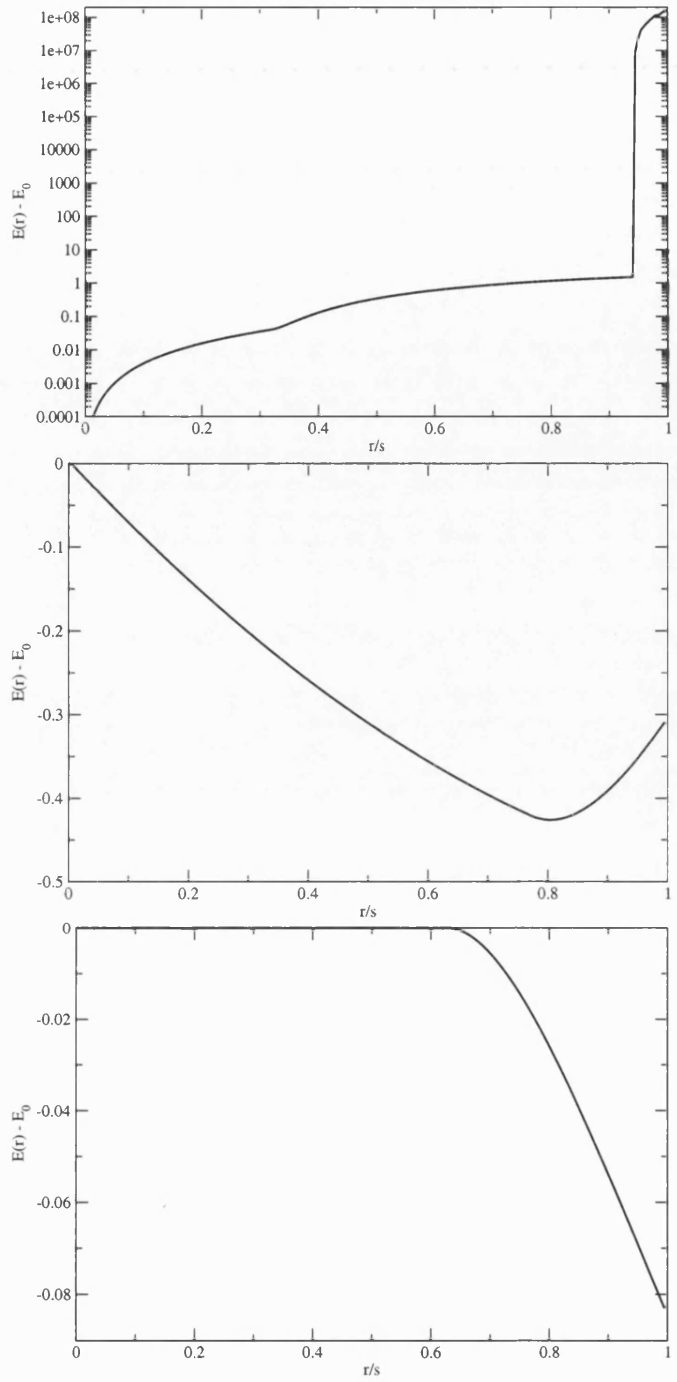

Figure 3.3: Radially symmetric cell potentials $E(r)$ (see equation 3.4) expressed relative to the ground state energy E_0 from the cell theory using Jagla's potential. **(a)** The high density phase, taken at $T = 0.2$, $P = 0.02$. **(b)** The intermediate density phase, taken at $T = 0.04$, $P = 0.02$. **(c)** The low density phase, taken at $T = 0.5$, $P = 0.006$.

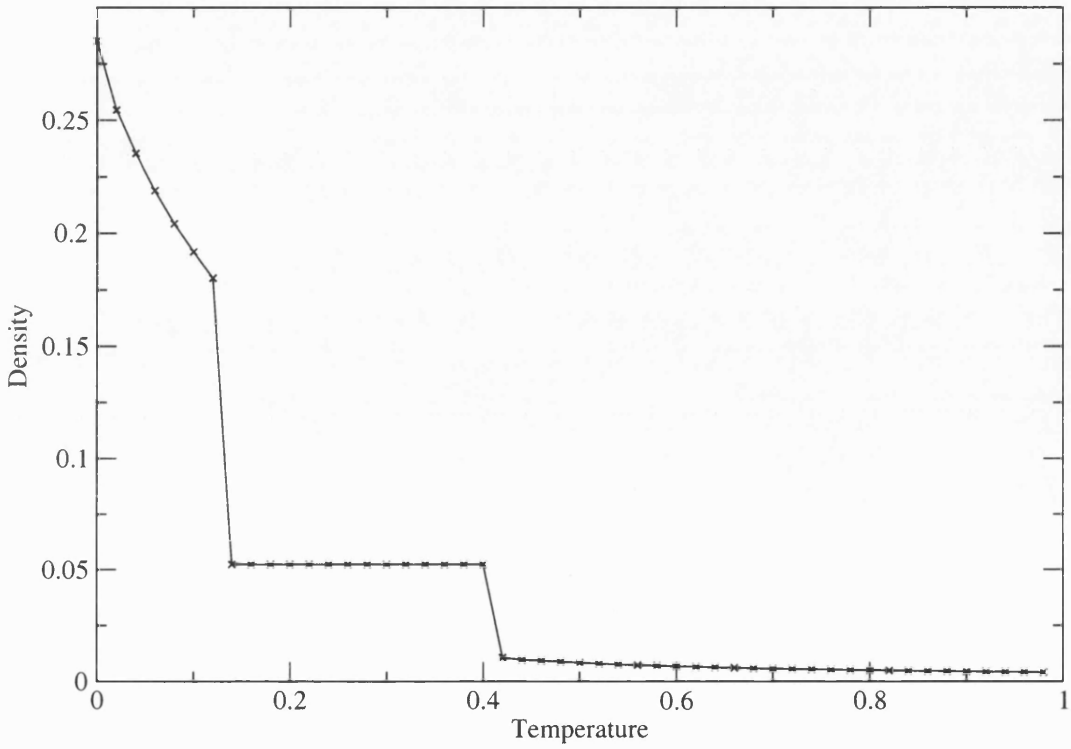

Figure 3.4: An isobar at $P = 0.004$, as calculated using the cell model for Jagla's potential.

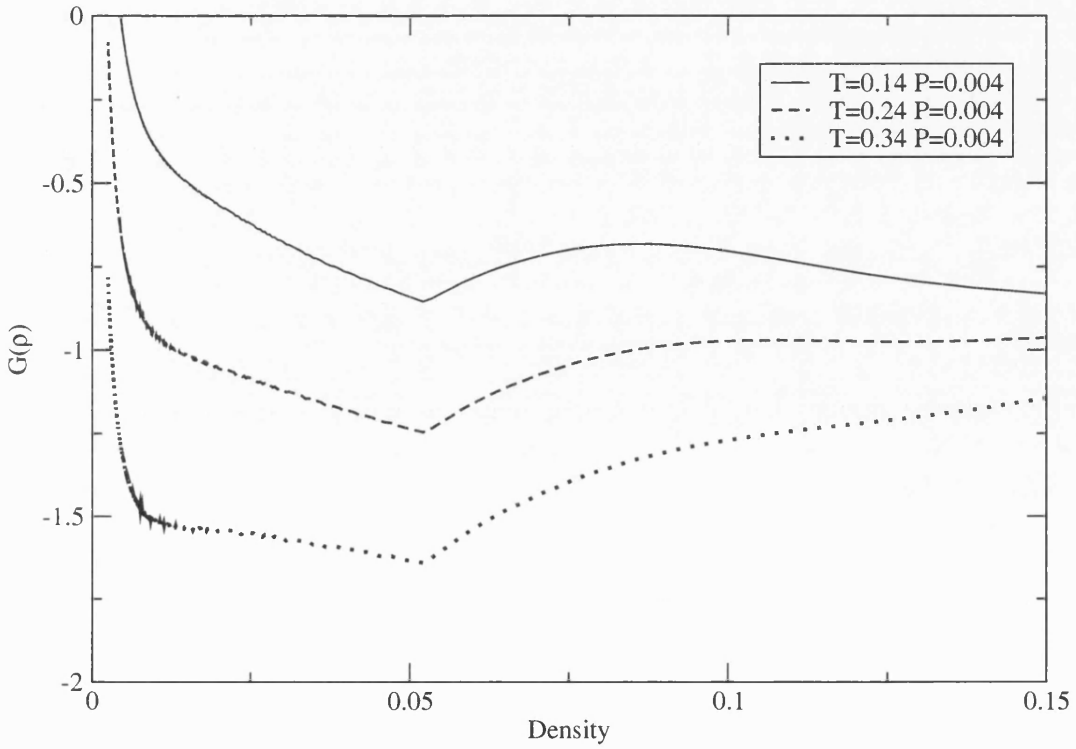

Figure 3.5: Gibbs free energy plotted against the density at three temperatures of the $P = 0.004$ isobar.

results of Wilding and Magee [54] of $T_c = 0.076(2)$, and $P_c = 0.0341(5)$ – while the pressures differ only by a factor of 2, the temperatures differ by an order of magnitude.

3.3 Changing the potential

How does the picture change if the parameters of the pair potential change? We tried a variety of different potentials to see how the phase diagram changed.

Whilst changing the shape of the interaction potential, it is important to keep the second virial coefficient $B(T)$ (defined below) constant, as it is an indication of the degree of non-ideality of the system. Specifically, in an ideal gas, $P = \rho k_B T$, while in a non-ideal gas we can write $P = \rho k_B T(1 + B_2\rho + B_3\rho^2 + ...)$, where B_2 is the second virial coefficient.

The second virial coefficient, simplified to the isotropic case from the definition in *Computer Simulation of Liquids* [67] is

$$B_2(T) = -\frac{1}{2}\int_0^\infty 4\pi r^2 \left(e^{-U(r)/T} - 1\right) \mathrm{d}r \tag{3.9}$$

where the units of temperature T are ϵ_0/k_B (as defined in Section 3.2). As can be seen, when the potential energy $U(r) = 0$ the contribution to $B_2(T)$ is zero, as particles are not affected by zero energy. When $U(r)$ is positive, the particles are pushed away, resulting in higher pressure, and so the contribution to $B(T)$ is positive. But, if $U(r)$ is negative, particles are attracted, the pressure decreases, and the contribution to $B(T)$ is negative.

As we are interested in the shape of the interaction potential, we can set the temperature to a constant value of 1. Also, beyond r_2, $U(r) = 0$ (as shown in equation 2.4) and so we can re-write the second virial coefficient as

$$B = -\frac{1}{2}\int_0^{r_2} 4\pi r^2 \left(e^{-U(r)} - 1\right) \mathrm{d}r \tag{3.10}$$

B was calculated for Jagla's interaction potential (defined in Section 3.2) and came to $-0.76r_0^3$.

We defined a "family" of potentials by changing the position of the minimum, r_1. The point where the ramp meets the hard core, $U(r_0)$, was kept constant, and r_2 was changed such that B was maintained at a constant value. This implies that each potential in the family is equally "displaced" from an ideal gas (assuming the effects of the higher-order virial coefficients are small), and thus has an equivalent effect on surrounding particles.

We assigned a depth to the well by defining a limiting potential which was an approximation of the Lennard-Jones potential. The minima were then set to lie on a line that joined the minimum of Jagla's well and the minimum of the Lennard-Jones approximation.

In order to do this, the Lennard-Jones interaction potential was scaled to have a similar B for comparison. It is described by

$$U(r) = 4\epsilon\left(\left(\frac{1}{r}\right)^{12} - \left(\frac{1}{r}\right)^{6}\right). \tag{3.11}$$

When $\epsilon = 0.41879428$, $B = -0.77r_0^3$.

The chosen parameters for the limiting Lennard-Jones approximation were $r_1 = 1.0\, r_0$, depth $= 0.6$ and $r_2 = 1.77783\, r_0$. It had a virial coefficient of $B = -0.76r_0^3$. Figure 3.6 shows the scaled Lennard-Jones interaction potential alongside the approximation and Jagla's original interaction potential.

A family of interaction potentials was chosen such that the minimum of each interaction potential lay on the line joining the two ramp minima, as drawn in figure 3.6.

Specifically, the depth of the minimum of each interaction potential was a function of r_1, thus:

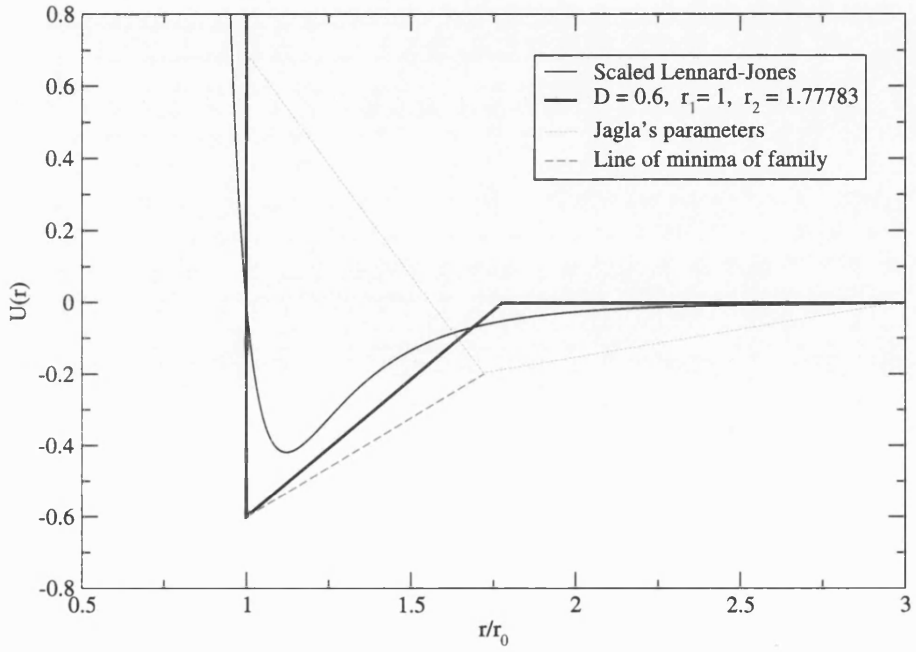

Figure 3.6: Comparing the scaled Lennard-Jones with its approximation (depth = 0.6, $r_1 = 1$ and $r_2 = 1.77783$). Also plotted are Jagla's original interaction potential and the line that the minima of the family of interaction potentials will lie on.

$$D(r_1) = 1.1578 - 0.5578 r_1 \tag{3.12}$$

where $D = -U(r_1)$.

Then, for each value of r_1, a value for r_2 was found that would keep B close to the value of B in Jagla's original model. In order to do this it was useful to re-write the equations defining the potential $U(r)$ so that it was defined in terms of the depth of the minimum, D, thus:

$$\tilde{U}(r) = \infty \quad \text{for} \quad r < r_0 \tag{3.13}$$

$$\tilde{U}(r) = (r_0 - r)(D + 0.69)/(r_1 - r_0) + 0.69 \quad \text{for} \quad r_0 \leq r < r_1 \tag{3.14}$$

$$\tilde{U}(r) = D\ (r_2 - r)/(r_1 - r_2) \quad \text{for} \quad r_1 \leq r < r_2 \tag{3.15}$$

$$\tilde{U}(r) = 0 \quad \text{for} \quad r > r_2 \tag{3.16}$$

where $\tilde{U}(r) = U(r)/\epsilon_0$ is a dimensionless potential (measured in units of a parameter ϵ_0 which serves to set the energy scale, and which we set equal to unity in what follows). The units of measurement are the same as for Jagla's potential (see Section 3.2).

A selection of the resulting family of interaction potentials can be seen in figure 3.7, and the parameters of the potentials studied in this thesis are listed in the Appendix.

3.4 Results using the family of potentials

Lines of coexistence correspond to pressures and temperatures where $G(V)$ has two minima of equal depth. For example, for the Jagla potential, there is a coexistence point at $T = 0.25$, $P = 0.285$. A $G(\rho)$ plot[1] at these parameters is shown in figure 3.8. It is possible to write a script that will calculate the

[1] In this system the density $\rho = 1/V$, where V is the cell volume.

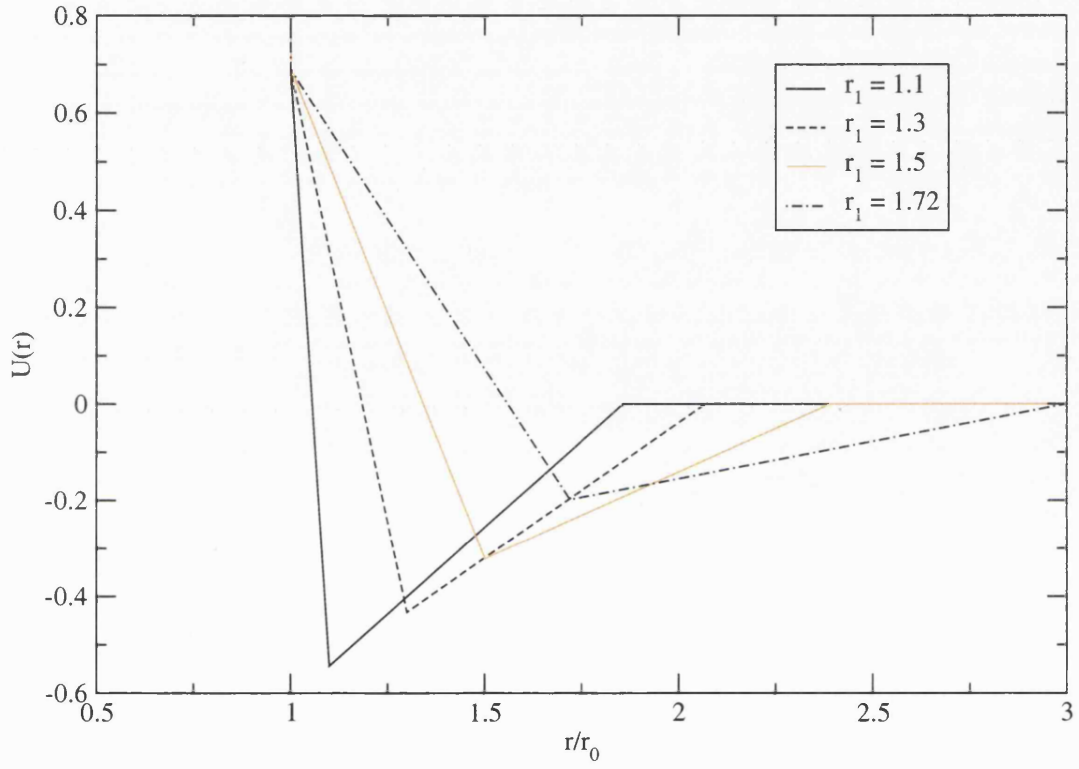

Figure 3.7: A selection of the family of interaction potentials chosen to move the critical point further towards the solid with decreasing r_1.

temperature and pressure at which the two minima have exactly equal depth. However, for the purpose of getting a broad overview, a line of coexistence can be approximated by plotting the temperature and pressure at which a jump in the density occurs (see figure 3.2). To do this, we calculated the density for a set of points on a pressure-temperature grid (one set of results is shown in figure 3.2), and where adjacent grid points of the same pressure showed a change in density of greater than 20%, the temperature and pressure of the lower density point was recorded.

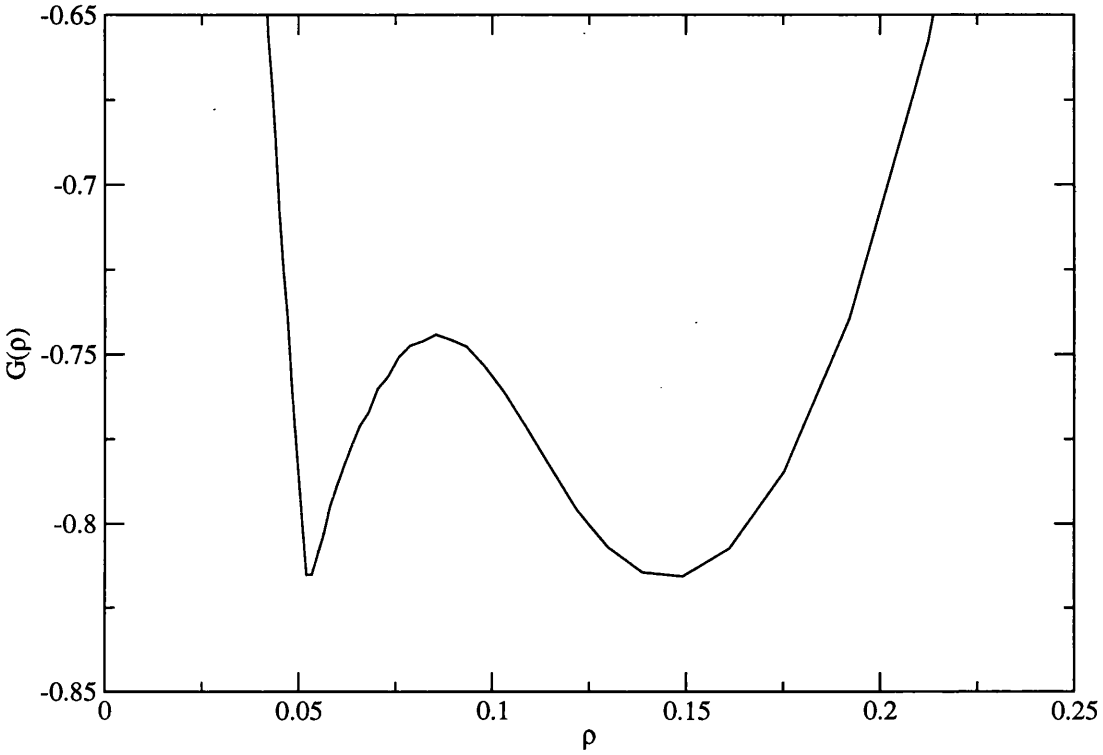

Figure 3.8: The plot of $G(\rho)$ for the Jagla potential at $T = 0.25$, $P = 0.0285$.

As the results (figure 3.9) show, the gradient of the higher-pressure, higher-density line of coexistence increases with decreasing r_1. Also, the length of the coexistence line can be seen to increase with decreasing r_1, with the critical point moving to higher temperatures and higher pressures.

3.5 Conclusion

While this method was quick to give results, there are strong doubts as to its accuracy. The fact that both the Lennard-Jones potential and the Jagla potential

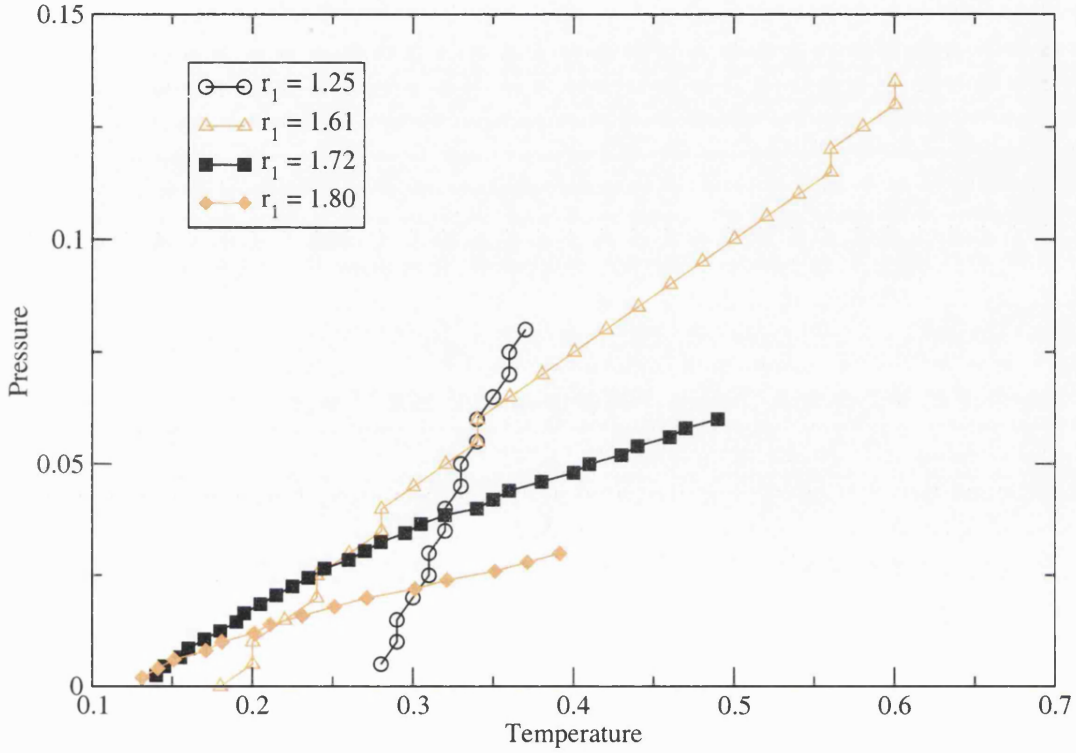

Figure 3.9: Approximate lines of coexistence (calculated as described in the text) for three potentials. Only the higher-pressure, higher-density coexistence line is shown for each potential. The whole line of coexistence (from the triple point at low temperature and pressure, to the critical point at high temperature and pressure) is plotted for $r_1 = 1.80$, 1.72 and 1.61, but for $r_1 = 1.25$, only the low temperature, low pressure end of the line is shown. The parameters of the potentials can be seen in the Appendix.

produce two critical points is not consistent with previous studies that have shown the Lennard-Jones model to have one critical point [68, 69], while the Jagla potential has two [54, 2].

The nature of the cell model does not allow the calculation of the interaction energy between two distinct particles. Nor does it allow any insight into how the proximity of a third particle may affect this interaction. It would appear that these are important calculations to make if one is to distinguish between the effects of the Lennard-Jones and Jagla potentials.

Chapter 4

Monte Carlo simulation techniques

We decided to proceed with our investigations using the Monte Carlo technique which allowed Wilding and Magee [54] to pin-point the critical points that Jagla had identified [2]. In contrast to the cell model discussed in the previous chapter, in this method the location of each particle is known, and thus interactions between multiple individual particles can be calculated exactly.

Molecular dynamics methods, which use Newton's equations of motion to calculate the trajectories of particles, would allow the calculation of the interaction energy between multiple individual particles too, but studying phase transitions requires a computational approach that allows movement across free energy barriers. While molecular dynamics allows particles to be tracked, it does not provide the means to overcome the free energy difference between phases. In contrast, Monte Carlo (a stochastic technique), described in Section 4.1, does not calculate trajectories but instead exploits the Boltzmann probability distribution function of observing a particle configuration. It is possible to increase the probability of the unfavourable configurations between phases (bias sampling), allowing the system to move freely across phase boundaries. The disadvantage is that it is meaningless to track individual particles, but for the purposes of studying the phase space of a selected interaction potential it is not necessary to know which path particles follow.

4.1 Monte Carlo

Named after the European gambling capital, Monte Carlo methods use random numbers to simulate systems. In our investigations, we used a type of classical Monte Carlo whereby samples are selected at random from the Boltzmann distribution to obtain thermodynamic properties. Thus we are able to explore the phase space of a substance described by an isotropic interaction potential. In this section, after a brief introduction to statistical mechanics, the specifics of the Monte Carlo method used will be discussed.

4.1.1 Statistical mechanics

Statistical mechanics involves calculating the probabilities of various configurations through microscopic properties (the interactions between particles) and macroscopic properties (such as temperature, pressure, volume and chemical potential). Simulations can take place in a variety of *ensembles.* An ensemble is a collection of points in phase space, the probability distribution of which is determined by which macroscopic parameters are kept constant. If, for example, the temperature, pressure and number of particles are fixed, and the energy and volume are allowed to fluctuate, this is known as the constant-NPT ensemble, or the isobaric-isothermic ensemble, and is the ensemble that we use in this thesis.

Other ensembles include the canonical ensemble (where the number of particles, volume and temperature are fixed and only the energy can fluctuate) and the grand-canonical ensemble (where the chemical potential, volume and temperature are fixed and the number of particles and energy can fluctuate). However, the canonical ensemble is poor at simulating phase transitions, as the density cannot fluctuate, while the grand canonical ensemble does not work well at high density due to the low probability of insertions of particles. The isobaric-isothermic ensemble is the natural choice if we want results in terms of pressures and temperatures, and it does well at simulating phase transitions. The only disadvantage is that the volume moves are costly to compute, and work less well at high densities when reductions in volume become unlikely.

In the constant-NPT ensemble the probability, p, of each coordinate set $\{q\}$

occurring, given the conditions c (macroscopic and microscopic variables), is given by

$$p(\{q\}|c) = \frac{e^{-\mathcal{E}(\{q\},c)}}{Q(c)} \tag{4.1}$$

where $\mathcal{E}(\{q\},c)$ is the dimensionless energy function with the factor $1/k_BT$ absorbed. Specifically $\mathcal{E}$ is H/k_BT where H is the enthalpy given by $H = U + PV$. The normalizing factor, or *partition function*, is defined by

$$Q(c) \equiv \frac{1}{N!}\frac{1}{h^{3N}}\frac{1}{V_0}\int \mathrm{d}V \int \mathbf{drdp} e^{-\mathcal{E}(\{q\},c)} \tag{4.2}$$

Where V_0 is a basic unit of volume to render the equation dimensionless.

The different phases are distinguished by an *order parameter* which changes dramatically with changes of phase. For different systems, different parameters are used. For example, for determining the difference between fluid phases of equal symmetry, as is done in this thesis, the density is most useful. The portion of the coordinate space associated with phase α is denoted $\{q\}_\alpha$, while the range of the order parameter M associated with that phase is denoted $[M]_\alpha$. It follows that $\{q\} \in \{q\}_\alpha$ if and only if $M(\{q\}) \in [M]_\alpha$. Thus it is possible to re-write equation 4.1 with a particular phase in mind:

$$p(\{q\}|\alpha, c) = \begin{cases} \frac{e^{-\mathcal{E}(\{q\},c)}}{Q_\alpha(c)} & \{q\} \in \{q\}_\alpha \\ 0 & \text{otherwise} \end{cases} \tag{4.3}$$

where

$$Q_\alpha(c) \equiv \frac{1}{N!}\frac{1}{h^{3N}}\frac{1}{V_0}\int \mathrm{d}V \int \mathbf{drdp} e^{-\mathcal{E}(\{q\},c)}\delta(M(\{q\}) - [M]_\alpha) \equiv e^{-G_\alpha(c)/k_BT} \tag{4.4}$$

where the delta function selects out those states that belong to phase α.

Equation 4.4 defines the *Gibbs free energy*, $G_\alpha(c)$ of phase α [70]. Using both equation 4.4 and equation 4.1 it is possible to write the partition function for phase α, Q_α(c), in terms of the total partition function for all the conditions c, $Q(c)$, thus:

$$Q_\alpha(c) = Q(c) \int \delta(M(\{q\}) - [M]_\alpha) p(\{q\}|c) \mathbf{drdp} dV \tag{4.5}$$

The *a priori* probability of phase α is therefore linked to its free energy thus:

$$p(\alpha|c) \equiv \int \delta(M(\{q\}) - [M]_\alpha) p(\{q\}|c) \mathbf{drdp} dV = \frac{Q_\alpha(c)}{Q(c)} = \frac{e^{-G_\alpha(c)/k_B T}}{Q(c)} \tag{4.6}$$

Between two phases, α and $\tilde{\alpha}$, the free energy difference is given by

$$\Delta G_{\alpha\tilde{\alpha}}(c) = G_\alpha(c) - G_{\tilde{\alpha}}(c) = k_B T \ln \frac{p(\tilde{\alpha}|c)}{p(\alpha|c)} \tag{4.7}$$

Therefore a phase boundary, where each phase has equal probability, is identifiable by points where the free energies of the respective phases are equal. Effectively this means that at a phase boundary a plot of the probability of the order parameter $p(M)$ against M will have two peaks, one corresponding to each phase, and that the area under the range of M corresponding to the first phase will be equal to the area under the range of M corresponding to the second phase.

All this is based on the assumption of *ergodicity* in $\{q\}$-space, i.e. that all parts of the phase diagram are accessible. Section 4.3.5 will describe a technique for overcoming the free energy barrier between phases that arises due to the mixing of the two species, thus allowing the simulation to sample both sides of the phase transition.

The cell theory in Chapter 3 was also in the constant-NPT ensemble. Thus phase boundaries were identified by points in the pressure-temperature plane where the Gibbs free energy function $G(V)$ expressed two minima, one for each phase, with

equal depth. This indicated that each phase was equally likely: the hallmark of a phase boundary.

To simulate a constant-NPT ensemble using Monte Carlo, the particles begin in a random configuration and then particle moves and volume changes are proposed. There are rules determining which changes are accepted, as will be explained below. At regular intervals the current volume and energy are recorded, and over time the probability distribution of each is obtained.

The acceptance rules employed are different depending on whether one is considering a particle move or a volume change. Both, however, stem from detailed balance, explained in the next subsection. In the two subsequent subsections the particle and volume acceptance rules are derived.

4.1.2 Detailed balance

The system must be in equilibrium in order to obtain the correct probability distribution. Therefore the probability of a change from state μ to state ν must be the same as the probability of the reverse. Mathematically, this is written as:

$$\sum_{\nu} p_\nu a(\nu \to \mu) P(\nu \to \mu) = \sum_{\nu} p_\mu a(\mu \to \nu) P(\mu \to \nu) \tag{4.8}$$

where p_ν is the probability the system is in state ν, $a(change)$ is the probability of attempting *change*, and $P(change)$ is the probability of *change* taking place.

The only way to satisfy this is to make sure all moves equally likely to be attempted, and that all moves are reversible:

$$p_\nu P(\nu \to \mu) = p_\mu P(\mu \to \nu) \tag{4.9}$$

This is known as detailed balance [71].

4.1.3 Particle moves

The classical energy distribution is the Boltzmann distribution, $p_\nu \propto e^{-\beta H_\nu}$, where H_ν is the enthalpy of state ν and $\beta = 1/k_B T$, or $1/T$ in our simplified units (see Section 3.2). Using this and rearranging equation 4.9 yields:

$$\frac{P(\mu \to \nu)}{P(\nu \to \mu)} = \frac{p_\nu}{p_\mu} = \frac{e^{-\beta H_\nu}}{Q} \frac{Q}{e^{-\beta H_\mu}} = e^{-\beta(H_\nu - H_\mu)} \tag{4.10}$$

If the change in enthalpy as a result of a change of state is negative, the change of state will definitely occur. Therefore, one of the probabilities will be unity, and so from this we get the Metropolis acceptance rule [71]:

$$P(accept) = \min\left\{1, e^{-\beta \Delta H}\right\} \tag{4.11}$$

where ΔH is the change in enthalpy, and the units of temperature T are as stated in Section 3.2. As a result there is a finite probability that the change will occur even if the enthalpy change is positive.

In this simulation method, the change of state takes the form of a particle move. To propose a particle move, random numbers are used to suggest the change in each coordinate. For example, $x' = x + rM_p$, where r is a random number between -1 and 1, and M_p is the maximum extent of the particle move. The enthalpy of the system with the particle in the new position is compared with the original enthalpy, and the probability of the change being accepted is calculated using the Metropolis acceptance rule. The calculated probability is compared with a random number between 0 and 1 to decide if the change should be accepted or rejected.

4.1.4 Volume change

A volume change is proposed according to the following equation:

$$\ln V' = \ln V + rM_V \tag{4.12}$$

where r is a random number between -1 and 1 and M_V is the maximum extent of the volume change. Because of the logarithms, when the volume is small, small changes are proposed, and when the volume is large, large changes are proposed. This best describes real systems.

Taking the exponential of each side of equation 4.12 gives

$$V' = Ve^{rM_V} \tag{4.13}$$

so the new volume is obtained by scaling the old volume, rather than incrementing it.

After the change has been proposed, the probability of the change taking place is calculated. This time, however, more than a comparison of the enthalpies of the states is required. The ratio of the volumes of the states is also part of the calculation of probability.

The reason for this comes from the effects of scaling the particle positions as the volume is changed. Scaling particle positions results in the volume space around each particle being scaled too. This is because the probability of any given configuration of particle positions is effectively zero, due to the infinite number of combinations, so instead of asking what the probability of a particle being at a particular location is, one asks what the probability is of it lying inside an infinitesimal volume $\mathrm{d}\mathbf{u}_i$, where $\mathbf{u}_i$ is the coordinates of particle i. Therefore we can define p_μ, the probability of state μ, as equivalent to $P(\{\mathbf{u}\}, V)\prod_{i=1}^{N}\mathrm{d}\mathbf{u}_i\mathrm{d}V$, where $\{\mathbf{u}\}$ is the set of coordinates of the particles in that state, and V is the volume of that state. Similarly, let $p_\nu \equiv P(\{\mathbf{u}\}', V')\prod_{i=1}^{N}\mathrm{d}\mathbf{u}_i'\mathrm{d}V'$.

When a volume change is made, the particle coordinates are scaled by the cube-root of the ratio of the old volume, V, to the new volume, V'. Therefore the volume round each particle is scaled by V'/V and the following is true:

$$\frac{\mathrm{d}\mathbf{u}_i'}{\mathrm{d}\mathbf{u}_i} = \frac{V'}{V} \tag{4.14}$$

Because the new volume is obtained by scaling the old volume, the size of the volume element $\mathrm{d}V$ is also scaled by the same factor. This results in

$$\frac{\mathrm{d}V'}{\mathrm{d}V} = \frac{V'}{V} \tag{4.15}$$

From this we can calculate the ratio of $\prod_{i=1}^{N} \mathrm{d}\mathbf{u}_i' \mathrm{d}V'$ (the new volume element

$$\frac{\prod_{i=1}^{N} \mathrm{d}\mathbf{u}_i' \mathrm{d}V'}{\prod_{i=1}^{N} \mathrm{d}\mathbf{u}_i \mathrm{d}V} = \left(\frac{V'}{V}\right)^{N+1}$$

From Detailed Balance (equation 4.9) we have (4.16)

From Detailed Balance (equation 4.9) we have

$$\frac{P(\mu \to \nu)}{P(\nu \to \mu)} = \frac{p_\nu}{p_\mu} = \frac{P(\{\mathbf{u}\}', V') \prod_{i=1}^{N} \mathrm{d}\mathbf{u}_i' \mathrm{d}V'}{P(\{\mathbf{u}\}, V) \prod_{i=1}^{N} \mathrm{d}\mathbf{u}_i \mathrm{d}V} \tag{4.17}$$

We can write p_μ as $e^{-\beta H_\mu}$ where H_μ, the enthalpy of state μ, is given by $H_\mu = U_\mu + PV$. Also $H_\nu = U_\nu + PV'$.

Therefore

$$\frac{P(\mu \to \nu)}{P(\nu \to \mu)} = \frac{p_\nu}{p_\mu} = \frac{e^{-\beta H_\nu + (N+1)\ln V'}}{e^{-\beta H_\mu + (N+1)\ln V}} \tag{4.18}$$

In the same way as in Section 4.1.3, this results in the volume change being accepted with probability

$$P(accept) = \min\{1, e^{-\beta \Delta H + (N+1)\ln(V'/V)}\} \quad [71]. \tag{4.19}$$

Again the calculated probability is compared with a random number between 0 and 1 to decide if the change should be accepted or rejected.

4.2 Implementation

One mole, 18 grams, of water contains 6×10^{23} molecules. However, even the newest computers cannot deal with systems remotely approaching that size: the memory usage and time required are too great. We use a system of 300 particles. One processor takes about 24 hours to sample ten thousand density values. Samples are taken every hundred steps, where a step is 300 particle move attempts and two volume change attempts. It is pointless to sample the data at every step as they would not differ significantly from each other.

In order to get realistic data using such a small number of particles we used periodic boundary conditions to make the particles behave as if they were in an

infinite system. It is essential that the range of the interaction potential is less than half the length of the simulation box: otherwise each particle would be able to interact with its periodic image.

The ability of the box to change size during the simulation reduces finite-size effects. The results of simulations carried out with a variety of different numbers of particles, but with the same pair potential, are compared to results using 300 particles, but with differing pair potentials, in figure 4.1. While increasing the system size has some effect on the temperature and pressure of the critical point, it is not a large change when compared with the changes that result from altering the potential slightly to identify overall trends.

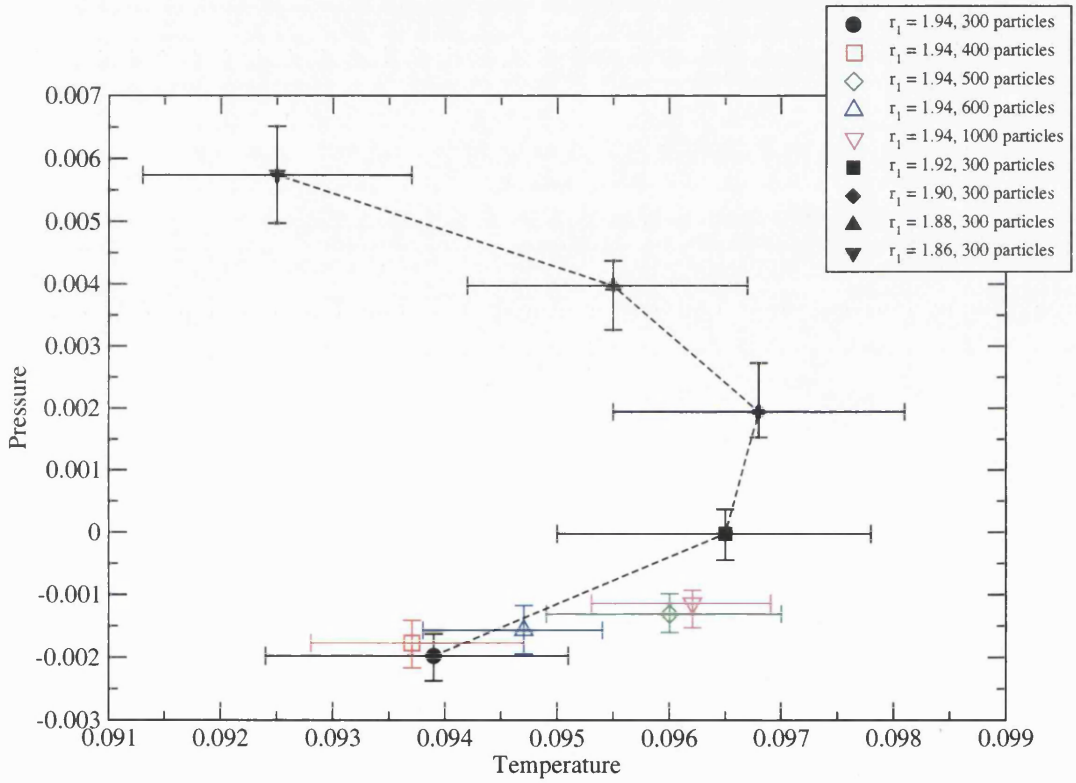

Figure 4.1: The temperature and pressure of the critical point of the $r_1 = 1.94$ pair potential (see equation 3.13 for a definition) is plotted for a variety of system sizes. Also plotted are the results of simulations of 300 particles carried out on several other pair potentials, defined by their value of r_1 (see Section 3.3). The dashed line joining the data obtained using 300 particles is a guide for the eyes.

The maximum extent of a particle move, M_p, is varied over the course of the simulation to maintain an approximate 50% acceptance rate. In the same way, the maximum change in the logarithm of the volume, M_V, is adjusted regularly throughout the simulation so that around half of the volume moves are accepted.

These measures are expected to increase the efficiency of the simulation, by reducing time spent rejecting moves that are too large, and reducing time spent making lots of small moves.

4.3 Analysis

During the simulation the energy and density were sampled every 100 steps. The data were stored in an output file. In addition, the coordinates of all the particles could be printed out at any stage during the simulation. In the following sub-sections a few of the methods used to analyse this data will be described.

4.3.1 Radial distribution

The particles' coordinates were used to gain information regarding the structure of the phases through calculating the radial distribution $g(r)$. The radial distribution is defined as the expected number of particles at separation r from a central particle, divided by the number expected at separation r for an ideal gas at the same density. This is written as

$$g(r) = \rho^{-2}\langle \sum_i \sum_{j \neq i} \delta(\boldsymbol{r}_i)\delta(\boldsymbol{r}_j - \boldsymbol{r})\rangle = \frac{V}{N^2}\langle \sum_i \sum_{j \neq i} \delta(\boldsymbol{r} - \boldsymbol{r}_{ij})\rangle \tag{4.20}$$

The radial distribution was obtained by counting the number of particles at each separation from a given particle. This was done at regular intervals throughout the simulation and the counts were stored in bins of width δr. At the end of the simulation, the count at each separation was divided by the number of samples taken, thus obtaining the average number of particles expected at each separation from a central particle. This was then divided by the number of particles expected at each separation in an ideal gas ($\frac{4\pi\rho}{3}((r+\delta r)^3 - r^3)$) [67].

4.3.2 Co-ordination number

Once $g(r)$ was obtained it was possible to calculate the co-ordination number, n, that is, the number of particles in the shell between separation distances r_a and r_b, as defined by the following equation:

$$n = \rho \int_{r_a}^{r_b} 4\pi r^2 g(r) dr \tag{4.21}$$

where $\rho = N/\langle V \rangle$, that is the number of particles over the average volume. r_a and r_b would be the separation distances bounding the peak in $g(r)$ that was being studied.

In addition, the positions of the particles could be printed out and visualised using Jmol, a java-powered graphics package, which allowed the system to be visualised from any angle.

4.3.3 Critical point identification

Graphs of the density against the number of steps show how the density varies over the course of the simulation. A jump in the density indicates a phase change. Near a critical point, the difference in density between the two phases involved is very small, so the simulation passes easily between the two phases of the system. This can be seen clearly in figure 4.2. The temperature and pressure of critical points were obtained using finite-size scaling techniques [72]. The basis of this is that at criticality the histogram of the density assumes a scale-invariant form very close to the *universal shape*. An example of this is seen in figure 4.3. Therefore, in order to identify the critical point, the temperature and pressure for which the density distribution resembled the universal shape were sought using histogram reweighting (Section 4.3.4). In particular, each peak had to be of equal area, and the ratio between the peak height and the trough's height had to be approximately 2.173 [73]. However, as we have not involved the energy in the order parameter, it is not the exact universal shape. In addition, due to the finite nature of the system, it would be impossible to obtain the exact universal shape even had we included the energy. Therefore, we quoted error bounds for each critical point.

The upper temperature bound was the temperature for which the height of the trough of the distribution was two-thirds of the height of the peaks (mean height, if the peaks were uneven). The lower temperature bound was the temperature for which the height of the trough was a third of the height of the peaks. The bounding pressures were the pressures at which one of the peaks had been reduced in height so that it almost disappeared.

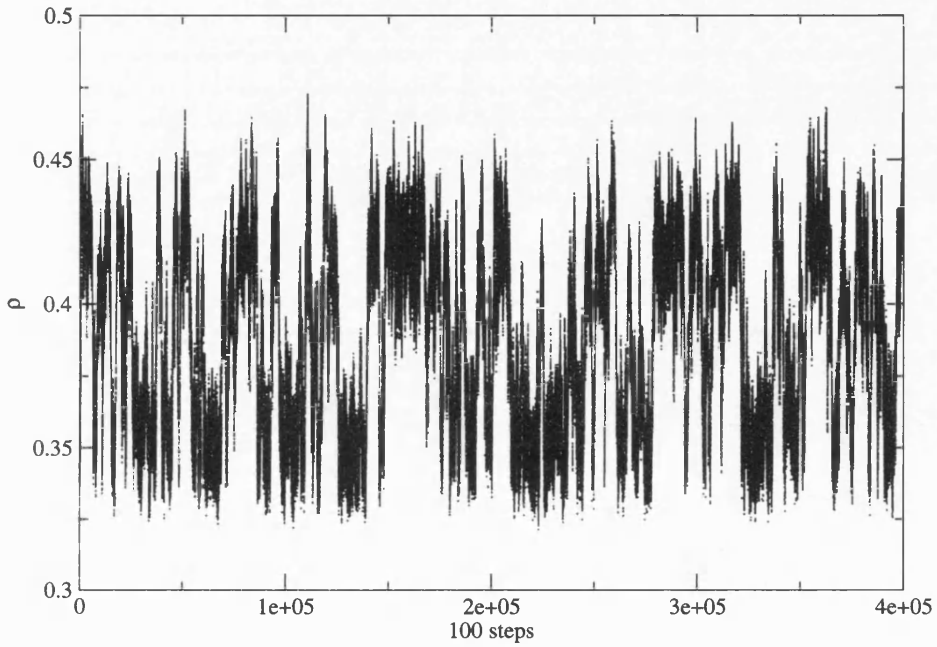

Figure 4.2: A density-step graph of a simulation at the HDL-LDL critical point. The simulation was of the $r_1 = 1.63\ r_0$ interaction potential at $T = 0.064$ and $P = 0.1012$.

4.3.4 Histogram reweighting

It is possible to reweight data to estimate the form of the histogram at a different set of pressure and temperature values from those at which the original measurements were taken. If $p(V|T,P)$ is the probability of volume[1] V at temperature

[1]Density and volume are interchangeable through $\rho = N/V$ where ρ is the density, N the number of particles (held constant at 300), and V is the volume.

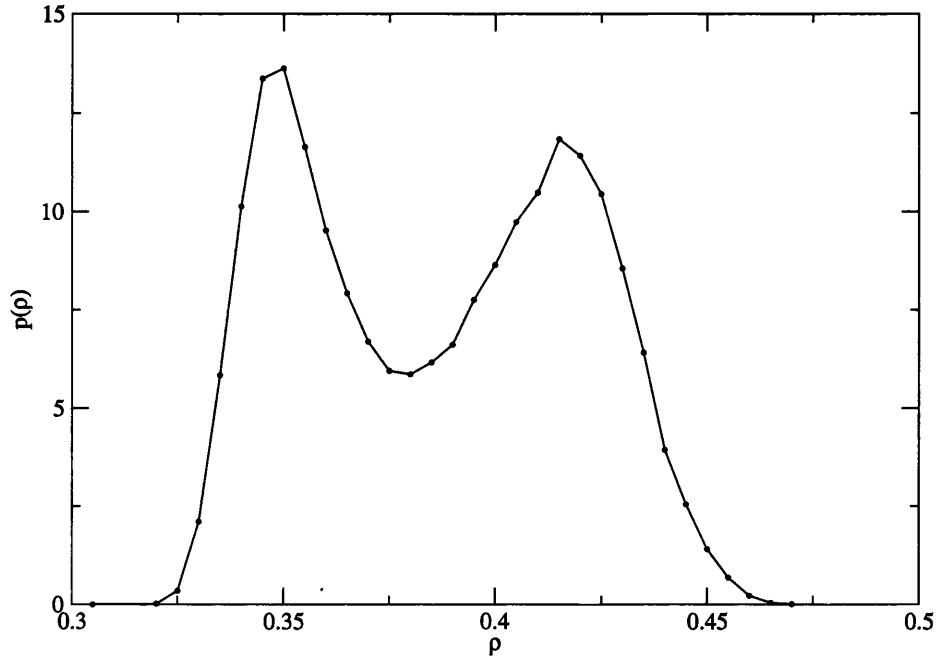

Figure 4.3: A normalised histogram demonstrating the probability of each density, obtained from the simulation run shown in Figure 4.2.

T and pressure P, then we can extrapolate to temperature T_e and pressure P_e to find $p(V|T_e, P_e)$, thus:

$$p(V|T_e, P_e) = \frac{Z}{Z_e} p(V|T, P) e^{-(\frac{1}{T_e} - \frac{1}{T})U - (\frac{P_e}{T_e} - \frac{P}{T})V} \tag{4.22}$$

where $\frac{Z}{Z_e}$ is a factor that is absorbed by normalisation.

The benefit of this reweighting is that it allows one to follow the line of coexistence in a phase diagram. The pressure can be varied until the reweighted histogram shows equal peaks at each of the densities, thus estimating where the point of coexistence occurs. However, this does not predict when the system will freeze because reweighting is unable to predict a density that was not sampled the initial simulation. Therefore, to determine if the system will freeze, a new simulation has to be run. However, the further from the critical point the system is, the larger the free energy barrier that the system has to pass to get from one phase to another.

In order to get good statistics to estimate $p(V)$ accurately, the system must pass back and forth between the two phases several times. To make this happen within the time-scale of the simulation, the probability of passing through the high free-energy states that involve the two phases coexisting has to be enhanced. This is done using multicanonical sampling, as detailed in Section 4.3.5 below.

4.3.5 Multicanonical sampling

Multicanonical sampling [74] allows easy passage over the free energy barrier between two phases, thus allowing us to gain reliable information about the shape of the graph of $p(V)$ away from the critical point. The aim is to artificially make the probability of each state equal, or, to put it another way, to have a flat histogram of the volume of the system. In order to do this, we weight the calculation of the probability thus:

$$p(V) = e^{-\beta H} \qquad \text{becomes} \qquad \tilde{p}(V) = e^{-\beta H - \ln w(V)} \tag{4.23}$$

where $w(V)$ is the weight attached to volume V and H is the enthalpy, $H = U + PV$.

Then, if we were to make $w(V) = p(V) = e^{-\beta H}$, then $\tilde{p}(V) = 1$ for all V and therefore the histogram is flat, as required.

The obvious problem is that $p(V)$ is exactly the function we are wanting to find. However it is possible to extrapolate the $p(V)$ found at the critical point to give an estimation of $p(V)$ for the new values of temperature and pressure, as described in Section 4.3.4. This estimation can then be used as the preweighting function, $w(V)$.

This preweighting function is then used during the simulation when calculating the probability that a volume change will take place:

$$P(accept) = \min\left\{1, \quad \frac{w(V)}{w(V')} e^{-\beta \Delta H + (N+1)\ln(V'/V)}\right\} \tag{4.24}$$

where $\Delta H = \Delta U + P\Delta V$

After the simulation has run for several million steps, the histogram of volumes of the system is normalised to give $\tilde{p}(V)$. The real probabilities can be extracted by reweighting thus:

$$p(V) = w(V)\ \tilde{p}(V) \tag{4.25}$$

This probability function, $p(V)$, can be extrapolated again to give a preweighting function for a simulation even further down the coexistence curve. As the temperature was lowered each time, the weighted simulations eventually froze – something that the extrapolations could not predict. Thus it was possible to identify the triple point with the solid on a line of coexistence between two liquids.

4.3.6 Multiple histogram reweighting

This method is particularly useful for tracing isobars. Using overlapping histograms from simulations carried out at several temperatures, it is possible to reduce the error bars of the estimates of the densities at the temperatures studied, and interpolate to obtain the densities with similarly small error bars at intermediate temperatures, thus vastly reducing the uncertainty in locating the temperature of density maximum.

It is also useful for finding the location of the critical point: when several overlapping histograms are close to the critical point, their combined information will reveal the location of the critical point with greater certainty.

The code used was written by Dr Nigel B. Wilding, based on the work in [75]. It begins by reading in the histograms of n simulations. The ith simulation is at pressure P_i and temperature T_i, and the volume and energy histograms ($N_i(V)$ and $N_i(U)$ respectively) are read in, each with $num(i)$ independent data points. As before, the enthalpy is given by $H = U + PV$, and so an enthalpy histogram can be constructed for each simulation i, labelled $N_i(H)$. The probability of enthalpy H at pressure P and temperature T is calculated thus:

$$p(H|T,P) = \frac{\sum_{i=0}^{n} N_i(H) \exp[-H/k_B T]}{Z \sum_{j=0}^{n} \frac{num(j)}{Z_j} \exp[-H_j/k_B T_j]} \tag{4.26}$$

Where

$$Z = \sum_{H} p(H|T,P) \tag{4.27}$$

And the partition functions Z_j are calculated self-consistently by iterating between the equations until the ratio of successive values does not differ from 1 by more than a threshold, set at 1×10^{-9}.

Similarly, the probability of each volume can be isolated, thus:

$$p(V|T,P) = \frac{\sum_{i=0}^{Nhists} N_i(V) \exp[-(\sum_{j=0}^{num(i)} U_{ij} + PV)/k_B T]}{Z \sum_{k=0}^{Nhists} \frac{num(k)}{Z_k} \exp[-(\sum_{l=0}^{num(k)} U_{kl} + P_k V)/k_B T_k]} \tag{4.28}$$

And, as before,

$$Z = \sum_V p(V|T,P) \tag{4.29}$$

Thus it was possible to find, for example, the volume at a temperature and pressure from a set of histograms at slightly different temperatures and pressures. This meant that, when plotting isobars, it was only necessary to set off a simulation at a few widely-spaced temperatures, and the probability distribution at intermediate temperatures could be extrapolated using this method.

In addition, the statistical error of $p(V|T,P)$ is given by

$$\delta p(V|T,P) = \frac{p(V|T,P)}{\sqrt{\sum_i^{Nhists} N_i(V)}} \tag{4.30}$$

so that, the more histograms involved, the better the estimate.

Chapter 5

From stable to metastable: the critical point is moved

Wilding and Magee used the constant-NPT ensemble [54] to study Jagla's $r_1 = 1.72$ potential, and so, as expected, we found the critical points at exactly the same temperatures and pressures as they did, within error bars.

We extended the study by considering the changes to the phase diagram resulting from changes in the potential. The majority of the contents of this chapter have already been presented in [1].

It should be noted that the results in this chapter and the next took around two years to obtain, due to the slow speed of the simulations. The nature of the constant-NPT ensemble was such that volume fluctuations were slow to be accepted, especially at low temperatures when the particles were close together.

Before going into how the LLCP moved with the changes in the potential, it is useful to consider the structural difference between the high density liquid (HDL) and the low density liquid (LDL), and the structural changes with temperature that result in the density anomaly.

5.1 Structural studies

Being able to identify the individual position of every particle at any point during the simulation allows us to plot the radial distribution function, $g(r)$, as laid out in Section 4.3.1.

5.1.1 HDL versus LDL

We used the $r_1 = 1.68$ potential (see Section 3.3 and the Appendix for its definition) for this study. We plotted $g(r)$ at a point on the LLPT line with temperature $T = 0.944T_c$ where T_c is the temperature of the LLCP. For one simulation we started with a configuration that was LDL and for the other simulation the initial configuration was HDL. As there was a large free-energy barrier between the two phases, and no weighting was used, the system remained in the initial phase for the duration of the simulation. Thus it was possible to sample purely from the LDL phase in the first case, and purely from the HDL phase in the second case. Each system was simulated for approximately 24 hours, during which around 4.5×10^6 Monte Carlo sweeps took place on a 1.7 GHz desktop processor. Thus sufficient data were gained for a smooth graph of $g(r)$.

As can be seen in figure 5.1, the difference between the HDL and LDL phases lies mostly in the proportion of particles separated from each other only by their hard core. In the HDL, far more hard cores are touching each other than in the LDL. In contrast, in the LDL, a greater proportion of particles are at the larger separation distance corresponding to the minimum in the potential energy curve.

On calculating the co-ordination number as described in Section 4.3.2 we found that a particle in HDL had, on average, 6 particles next to its hard core (specifically between separations of $1r_0$ and $1.3r_0$), compared to only 2 particles within that range in LDL. On average, a particle was surrounded at the larger separation corresponding to the potential minimum (specifically between $r = 1.3r_0$ and $r = 2.15r_0$) by 35 particles in HDL, compared with a larger number of particles (40 particles) in LDL.

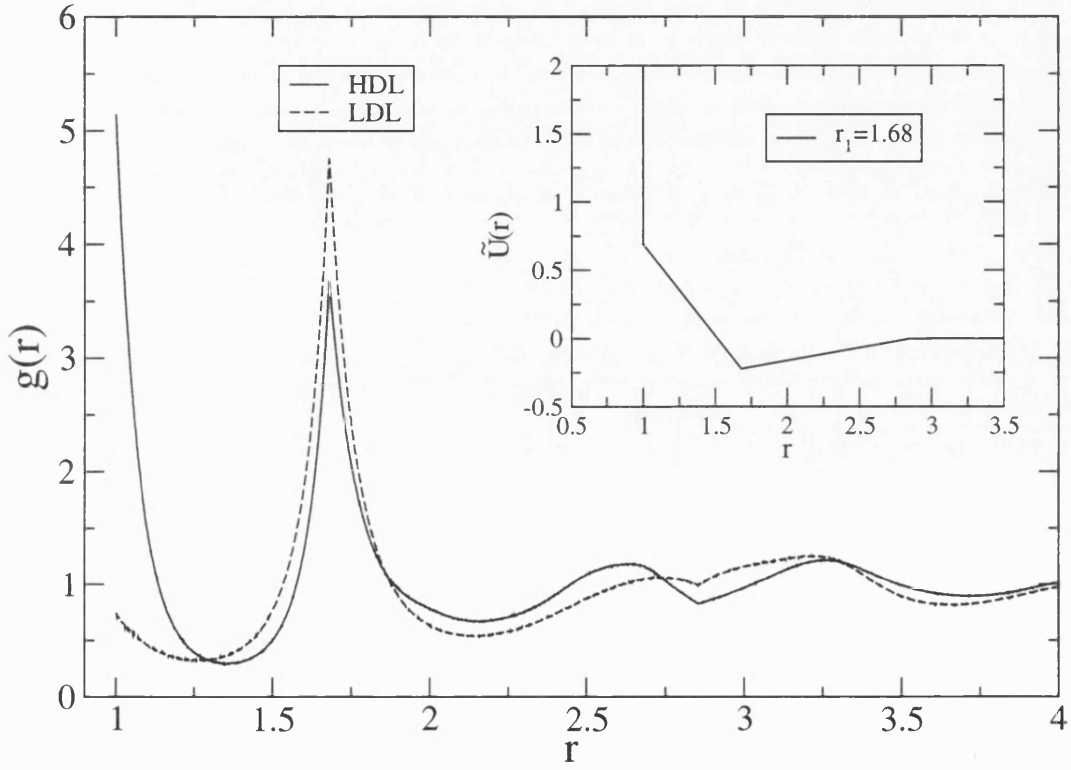

Figure 5.1: Comparison of the shapes of $g(r)$ for coexisting points on the LLPT line. Parameters are $r_1 = 1.68$, $T = 0.0644 = 0.944T_c$, $P = 0.05021$. The density of the HDL phase is $\rho = 0.484(1)$, while that of the LDL phase is $\rho = 0.313(1)$. The inset shows the corresponding form of the interaction potential.

5.1.2 The density anomaly

A radial distribution study was also carried out to determine what caused the density anomaly that was identified in [54] and [63]. An example of such an anomaly is shown in figure 5.2(a) for the potential $r_1 = 1.72$ along the isobar $P = 0.0247$. Each point on this graph required a day of simulation to obtain the 67% uncertainty error bars plotted. As can be seen, the maximum density occurs at $T_{MD} = 0.095(5)$. The radial distribution at this temperature is plotted in figure 5.2(b) along with radial distributions at temperatures on either side of T_{MD}. As one would expect, the number of particles resting in the minimum of the potential increases with decreasing temperature. However, looking at the inset of figure 5.2(b), the trend in the proportion of particles resting at the hard core is not as simple. As temperature decreases, the proportion of particles in close contact increases, but peaks at T_{MD}. Thereafter, lowering the temperature further sees fewer particles resting at the hard core, resulting in the observed density maximum. Thus we have seen that the reason for the density anomaly is a shift from the shorter of the two separation distances to the longer as temperature is lowered.

5.2 Phase behaviour

The phase diagram for Jagla's potential was thoroughly studied by Wilding and Magee [54]. In the present study we build on that by seeing how changing the parameters of the potential affects the phase diagram. In particular we followed the LLCP and associated LLPT.

5.2.1 Moving the critical point

A family of potentials was defined in Section 3.3, each labelled by the value of the separation distance r_1 – the distance at which the minimum value of potential energy occurs. Decreasing r_1 makes the potential more like the Lennard-Jones potential.

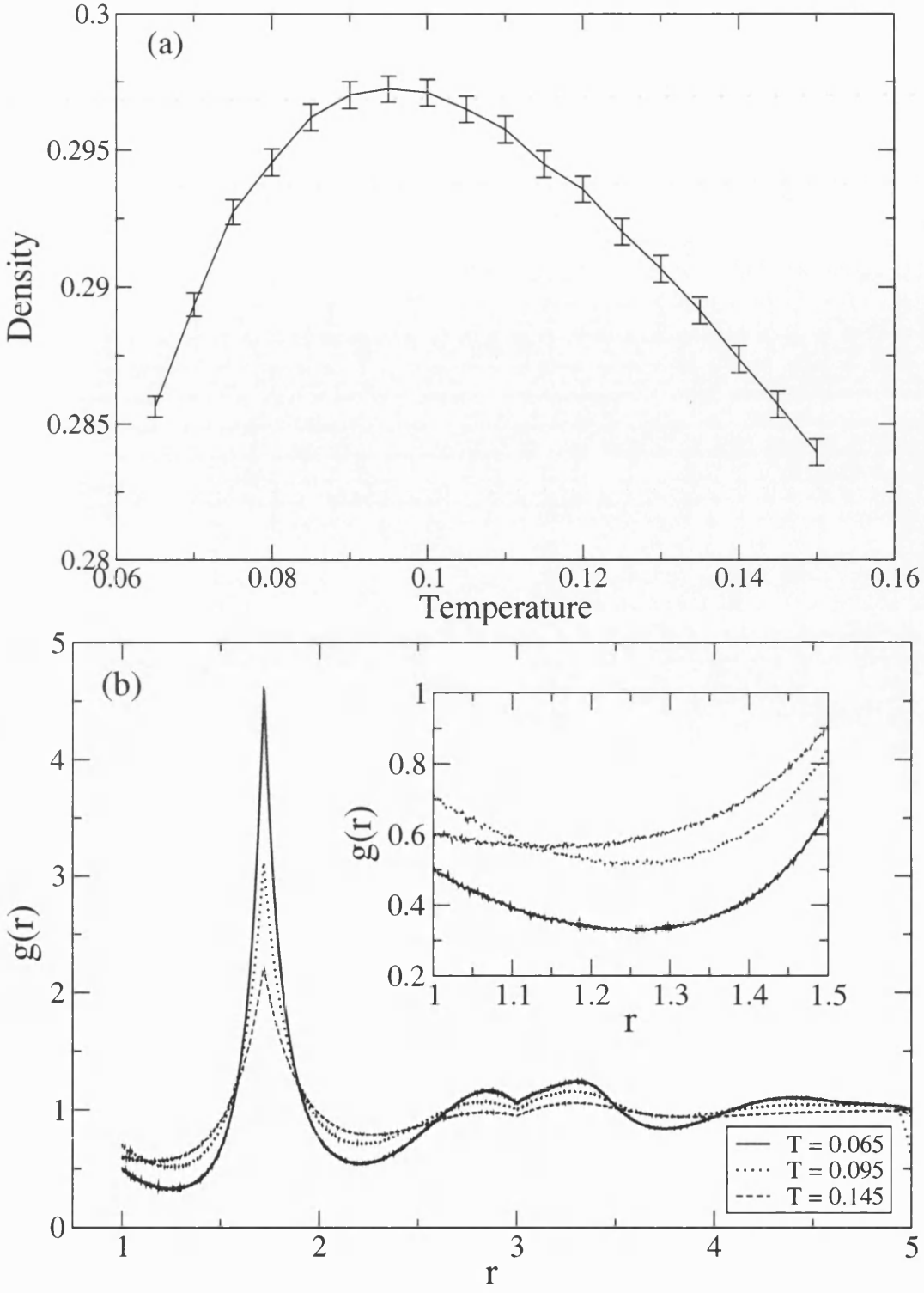

Figure 5.2: **(a)** The measured number density as a function of temperature for $P = 0.0247$, for the potential having $r_1 = 1.72$. The error bars are given by the standard deviation divided by the square root of the number of data points. **(b)** The measured form of the radial distribution function $g(r)$ for the same potential at three temperatures on the $P = 0.0247$ isobar spanning $T_{MD} = 0.095(5)$.

By making small changes in the value of r_1, the LLCP was caused to move by similarly small amounts on the phase diagram. Thus it was possible to locate the LLCP quickly after each change in parameters. Pressure and temperature were varied until the first signs of a phase transition were seen in the density-step plot, and then histogram reweighting (Section 4.3) was used to get a better estimate of the position of the critical point. Further simulations were then carried out until the histogram of the $p(V)$ plot had the universal shape. Each simulation took about a day to get sufficient data from which to extrapolate. Near the critical point the simulations were of longer duration to increase the accuracy of the estimation of the critical temperature and pressure.

Using the trend of the LLCP movements, it became possible to predict where the next LLCP would be, making it easier to locate the first signs of the critical point for subsequent LLCPs.

For some LLCPs the LLPT was tracked using a combination of histogram reweighting and multicanonical preweighting, as described in Section 4.3.5, in order to determine its gradient and identify the triple point with the solid. Again, each simulation along the line of coexistence had to be at least a day long to obtain enough data to perform the required histogram reweighting.

In some simulations the system went into a new phase. The phase was of lower density, covered a much narrower range of densities (as shown in figure 5.3) and was suspected of being a solid phase. A plot of the radial distribution of the phase is compared with the radial distribution of the HDL in figure 5.4. The structure after the potential minimum at $r = 1.60$ is more defined in the new phase than in the HDL phase, indicating that the new phase may be a crystal.

In order to be sure that the new phase is indeed a crystalline solid, the three-dimensional graphic imaging package called Jmol was used to visualise the co-ordinates of all the particles in a snapshot of the suspected solid. As shown in figure 5.5, the particles are indeed organised into a crystalline structure. The configuration could be swivelled and studied from all angles. This revealed that it had a hexagonal close-packed (HCP) structure.

For freezing to occur took a varying number of Monte Carlo steps in simulations with the same initial parameters, due to the stochastic nature of the process.

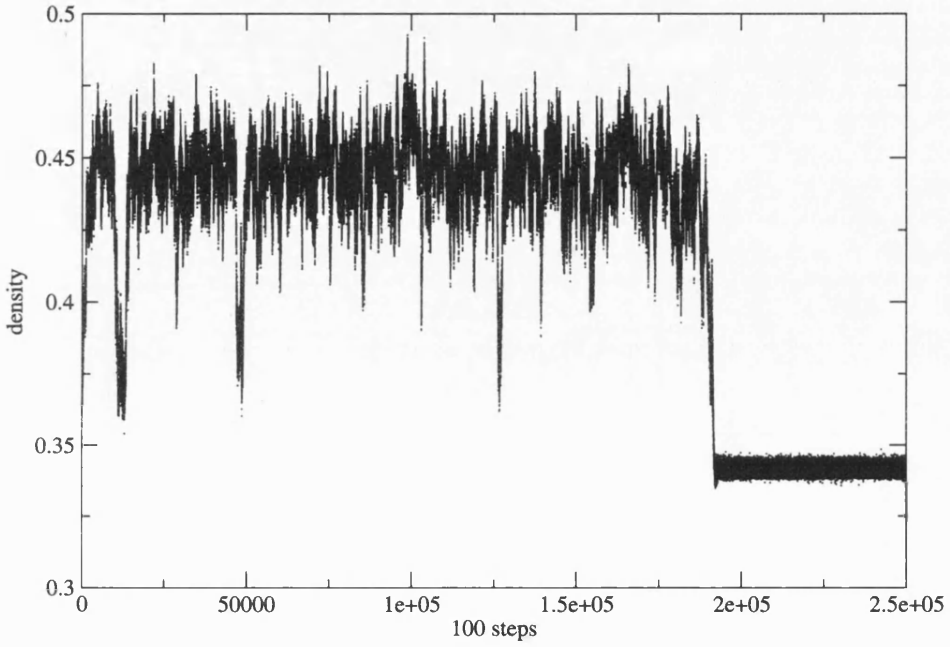

Figure 5.3: A density versus step number graph of a run that was near-critical but changed to the new phase after 1.8×10^7 steps. $r_1 = 1.6\ r_0$, pressure $P = 0.145$, temperature $T = 0.062$.

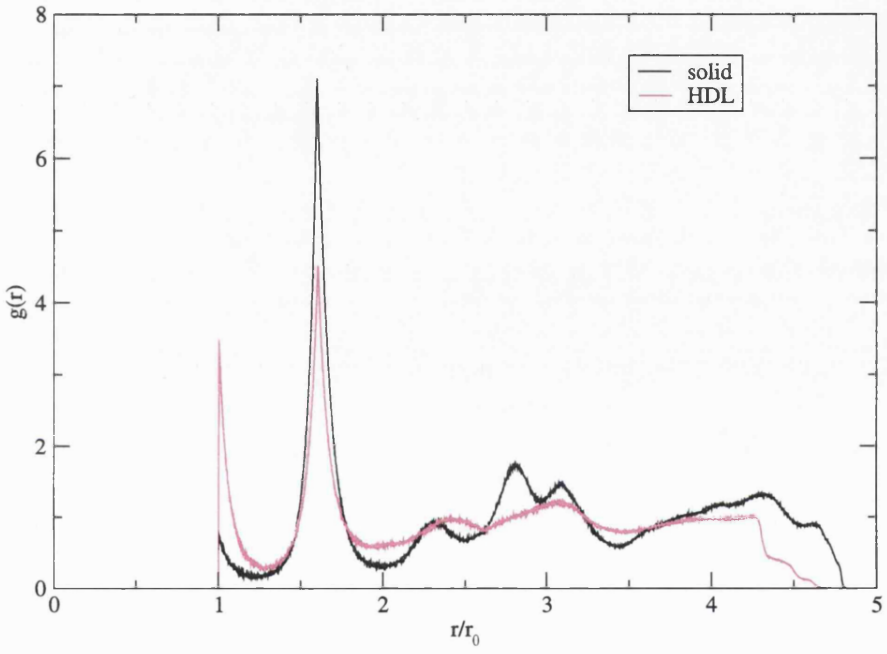

Figure 5.4: Comparing the radial distribution of the system in the HDL phase and the new phase described in the text. The HDL phase is at $P = 0.155$, $T = 0.06$, while the new phase is at $P = 0.1456$, $T = 0.062$. Both graphs were obtained using the $r_1 = 1.6$ pair potential.

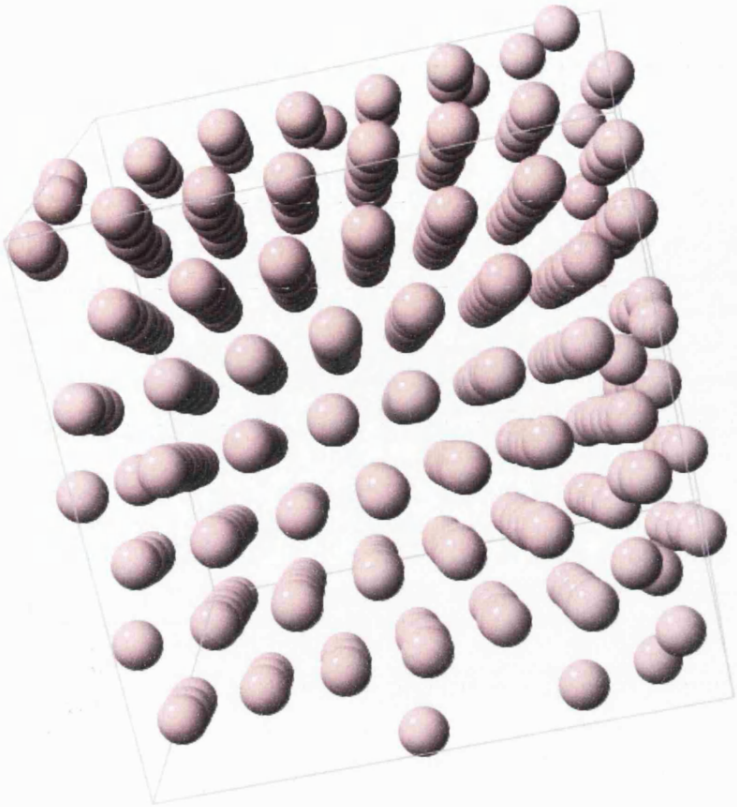

Figure 5.5: Graphical representation of the new phase described in the text. It is an HCP crystalline solid at $P = 0.1456$, $T = 1 \times 10^{-6}$, using the $r_1 = 1.6$ pair potential.

Each simulation down a coexistence line was at a lower temperature than the one before. To obtain the approximate position of the freezing point along a coexistence line, we marked the freezing point as being at the temperature and pressure at which the system first froze within 4.5×10^6 Monte Carlo sweeps (roughly a day on a 1.7 GHz desktop processor).

The freezing point along each line of coexistence was plotted, as were the LLCPs and LLPTs, on a pressure-temperature chart shown in figure 5.6. As can be seen, the LLCP for $r_1 < 1.61$ is metastable with respect to the crystalline solid. As r_1 is decreased, the LLCP shifts to lower temperatures and higher pressures, whilst the freezing point moves to higher temperatures. Thus the stable section of the LLPT gets shorter with decreasing r_1, until $r_1 = 1.61$ when the LLCP is just at the freezing point. This LLCP, and the one for $r_1 = 1.60$, was identified using the density fluctuations occurring in the period prior to freezing. However, for $r_1 = 1.59$ there were insufficient fluid phase density fluctuations before freezing occurred (at least 10 traverses of the fluid density range are required to obtain a reasonably reliable result), so we had to extrapolate the histogram from a higher temperature to identify the LLCP. For values of r_1 below this, the stable region was too far from the LLCP to extrapolate, and near the LLCP the system did not stay in the liquid phase for any time before freezing, making identification of further LLCPs impossible.

5.2.2 Freezing behaviour

In order to identify the types of freezing behaviour which may occur in our model potentials, we have estimated the locus of the liquid-solid coexistence boundary in the pressure-temperature plane of the pair potential defined by $r_1 = 1.61$ (for which the LLCP is barely metastable). The points on the estimated coexistence boundary, marked in figure 5.8(a), are the temperatures at which simulations along an isobar first froze within 3×10^6 Monte Carlo steps. The simulations at higher pressures froze to an HCP solid, while the simulations at lower pressures formed a face centred cubic (FCC) solid, an example of which is shown in figure 5.7. Figure 5.8(b) shows, for both a high and low pressure, the time evolution of the simulation density starting from an initial liquid-like configuration for two temperatures on either side of the freezing point. In the case of the higher pressure ($P = 0.1$), the system freezes to an HCP solid of lower

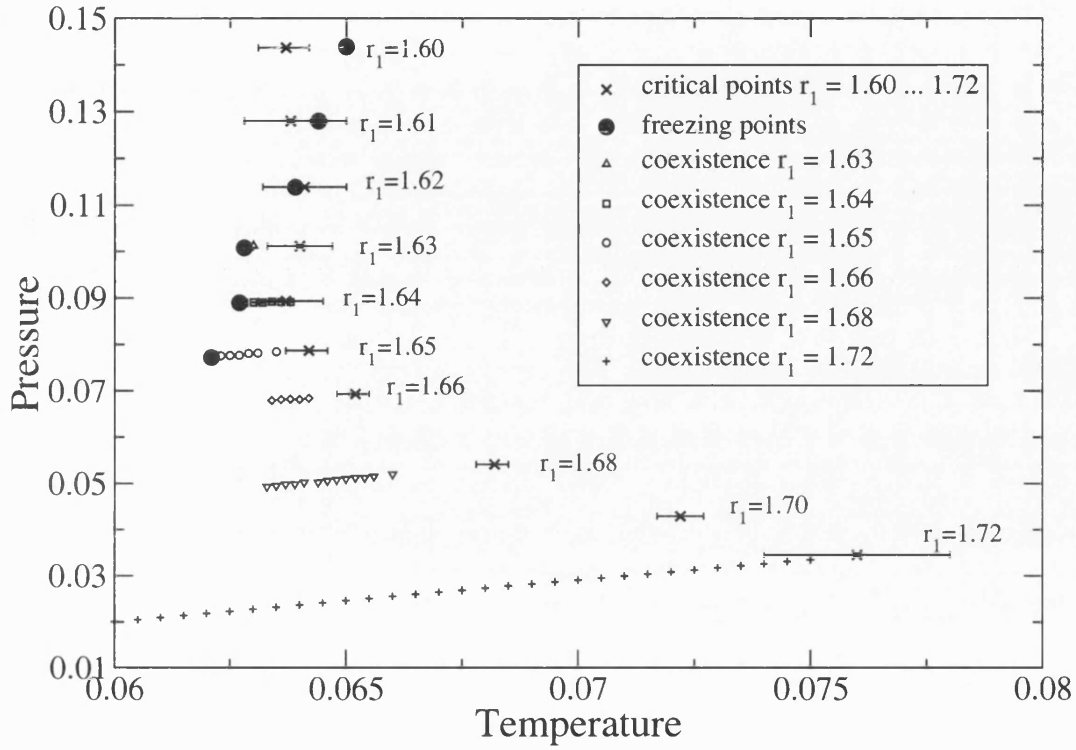

Figure 5.6: The near-critical region of the phase diagram for each of the ramp potentials studied. Shown in each instance is the estimated location of the LLCP. For certain larger values of r_1 in the range studied, a segment of the LLPT has also been estimated. The point of intersection of the LLPT (or its continuation) with the freezing line is shown for potentials in which the LLCP is either metastable or only moderately stable with respect to freezing. Error bars represent the uncertainties in the critical temperature. Uncertainties in the critical pressure, as well as in the location of the LLPT and the freezing points, are comparable to the symbol sizes.

density than the liquid, while for lower pressure ($P = 0.001$), the solid is FCC, having a density greater than that of the liquid. Therefore, by the Clapeyron relation (equation 1.4), the section of the coexistence line where the solid was FCC would be expected to have a positive gradient, while the section where the solid was HCP would be expected to have a negative gradient. This is indeed confirmed by figure 5.8(a): within the limited accuracy of our measurements, the gradient of the freezing boundary appears to change sign at $P \simeq 0.02$, suggesting that this marks a triple point between HCP, FCC and liquid phases. We have not attempted to map the HCP-FCC coexistence line within the solid region.

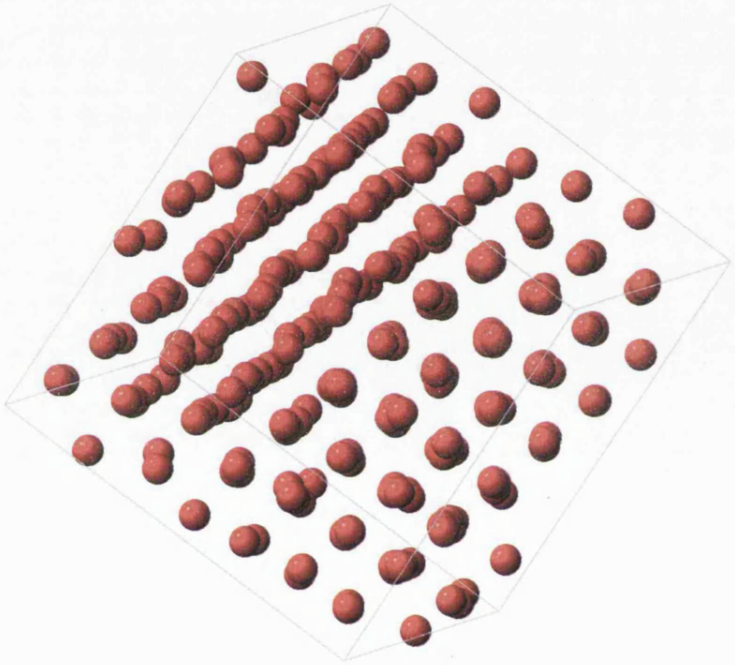

Figure 5.7: Graphical representation of an FCC crystalline solid at $P = 0.001$, $T = 0.082$, using the $r_1 = 1.61$ pair potential. Compared with the HCP crystal in figure 5.5, the planes in the FCC crystal alternate A-B-C-A-B-C, while in an HCP crystal, the planes alternate A-B-A-B.

5.2.3 The gradient of the LLPT

The gradients of the LLPTs were measured. For the potentials with $r_1 > 1.63$ this was done by finding the line of best fit of the coexistence points previously calculated and presented in Section 5.2.1. However, for $r_1 <= 1.63$ not enough of the line of coexistence was available to get a good estimate of its gradient.

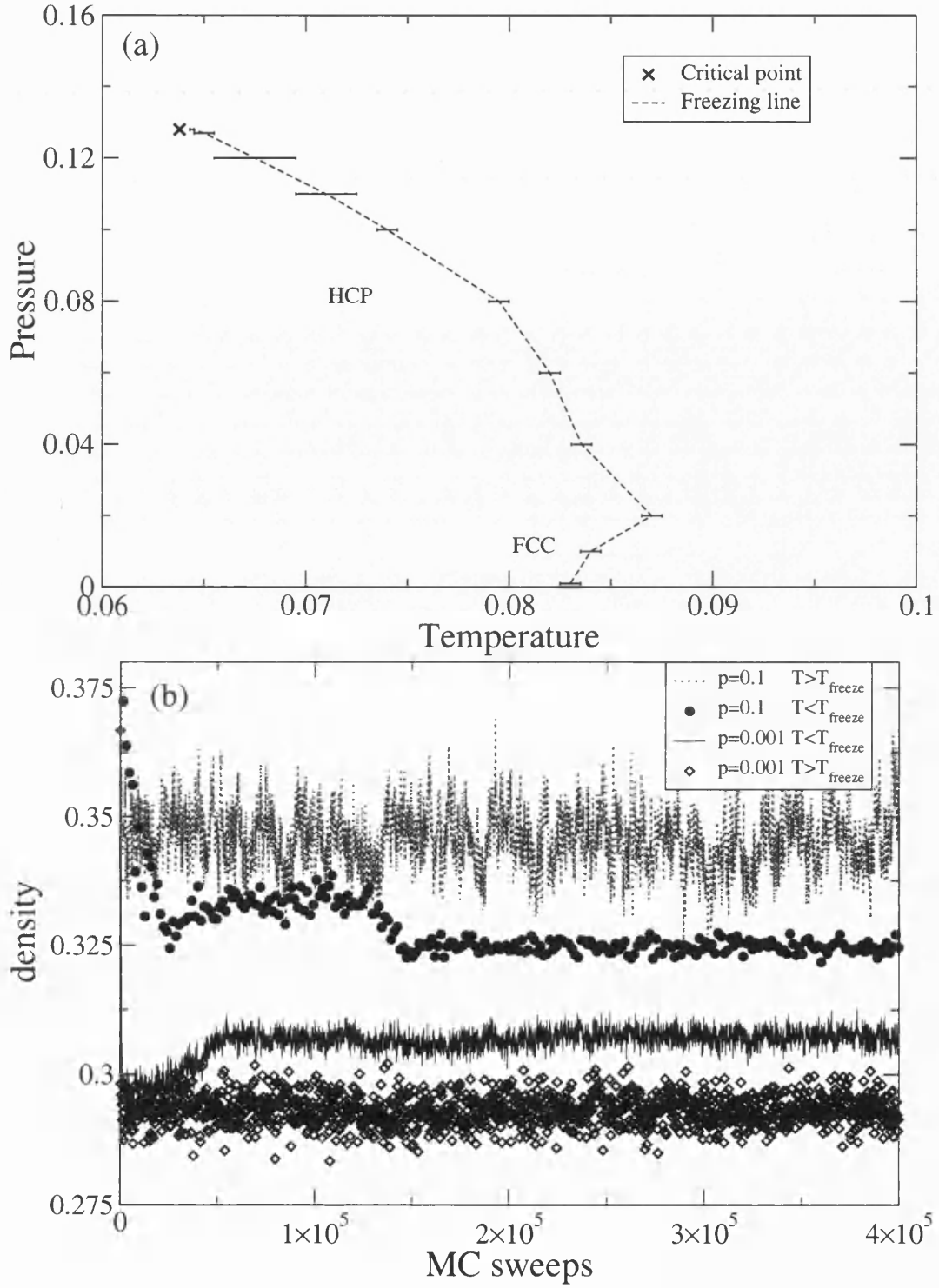

Figure 5.8: **(a)** Estimate of the liquid-solid coexistence boundary and location of the LLCP for $r_1 = 1.61$. **(b)** The time evolution of the system density close to the freezing transition, as described in the text. The figure shows the freezing to a solid of higher density for low pressures, and the freezing to a solid of low density for high pressures. Time is measured in units of Monte Carlo sweeps.

Therefore histogram reweighting (Section 4.3.4) was employed to project the line of coexistence using the data obtained at the critical point. This was done by extrapolating to a lower temperature and finding the pressure that gave two histogram peaks of equal area. In the case of $r_1 = 1.59$, data were only available at temperatures slightly above the LLCP, but the two peaks were still just distinguishable. It was therefore possible to find the pressure that equalised the areas under both peaks, and then extrapolate to lower temperatures towards the critical point, as done previously in Section 5.2.1, to locate the critical point. When extrapolating the histogram for each of the critical points found, it was noticed that the line of equal-peaked histograms continued at the same gradient in the $P-T$ phase diagram above and below the critical point. Therefore the gradient of the line linking the temperature and pressure of the super-critical, equal-peaked histogram with the temperature and pressure of the predicted $r_1 = 1.59$ LLCP is a reliable result for the gradient of the LLPT.

For $r_1 > 1.63$, the error of the gradient of the line of best fit was obtained through summing the squares of the deviations of the data points from the line. To gauge how accurate histogram reweighting was at finding the gradient of the LLPT, this method was performed too. The result always fell within the error bars of the line of best fit result. Therefore, the error associated with the line of best fit through the line of coexistence points was used as an indication of the error from histogram reweighting.

In contrast to the results using the cell model (Chapter 3), the gradient of the LLPT was found to decrease in magnitude with decreasing r_1. In addition, the gradient of the LLPT for the $r_1 = 1.59$ potential was found to be negative, as is predicted for water (see Section 2.1.3). The values obtained for the gradients are plotted against r_1 in figure 5.9.

The change of gradient was shown to be due to a shift in the relative entropies of the phases. We were able to calculate the entropy difference, ΔS, between HDL and LDL at sub-critical temperatures through the second law of thermodynamics for a reversible process: $\Delta S = \Delta H/T$, where $H = U + PV$ and U is the total energy of the system, gained by adding together the energy of all the individual interactions. We found that when r_1 was larger, the LDL phase had a larger entropy than the HDL phase, but as r_1 was decreased, the difference in entropy decreased also. We predict that around $r_1 = 1.60$ the situation will be reversed,

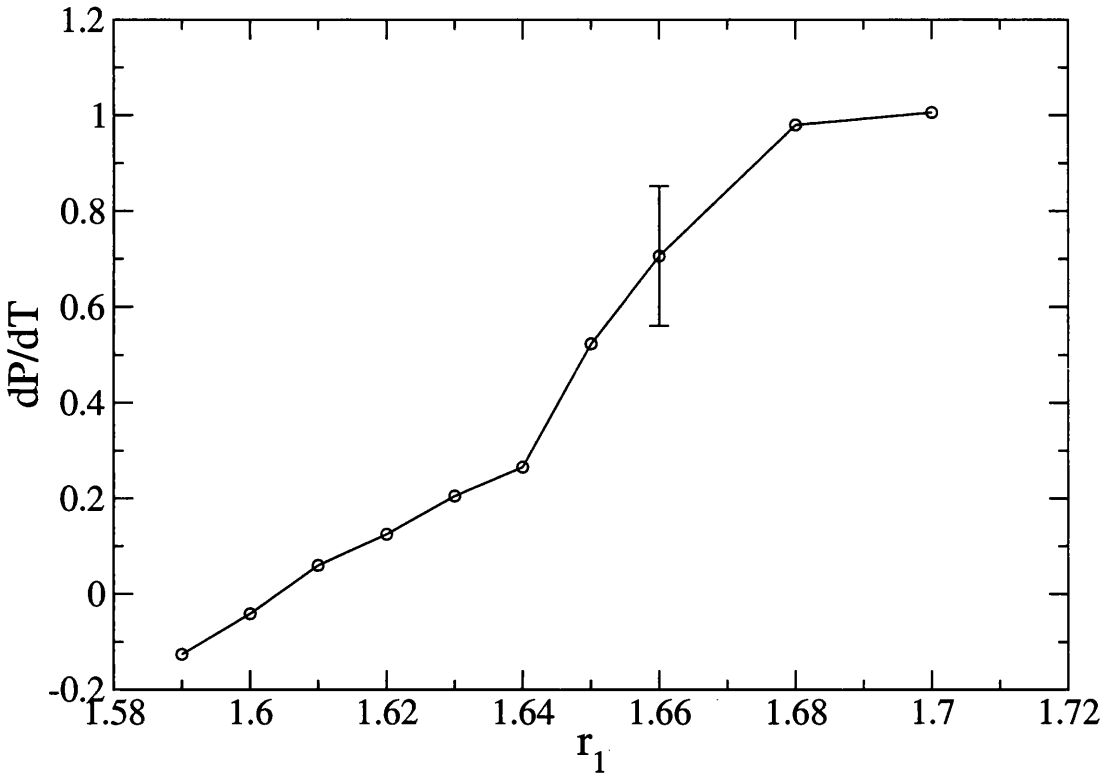

Figure 5.9: Estimates of the near-critical gradient of the LLPT in the $P-T$ plane for the family of potentials shown in 3.7. A representative error bar is shown.

with the entropy of the LDL phase becoming less than that of the HDL phase, resulting in the negative gradient of the LLPT, in accordance with the Clapeyron relation (equation 1.4).

The phase diagrams for the $r_1 = 1.59$ and $r_1 = 1.6$ potentials are therefore very like that predicted for water: the LLPT and LLCP are both metastable and the LLPT has a negative gradient.

5.2.4 Studying the density anomaly

In water, while the predicted LLCP is metastable with respect to a crystalline solid, the density anomaly is visible in the stable fluid region. We wanted to see if, in our model, in those cases where the LLCP was metastable, the density anomaly was still in the stable region. To this end, we carried out simulations along isobars, and, through multiple histogram reweighing (detailed in Section 4.3.6), plotted temperatures of maximum density (TMD) on a pressure-temperature plot. For

each point on the locus of TMD, at least four day-long simulations were required, one at each temperature along the isobar, from which the maximum temperature was obtained. We did this for several of the pair potentials, and superimposed the results on the data in figure 5.6. The resulting plot can be seen in figure 5.10.

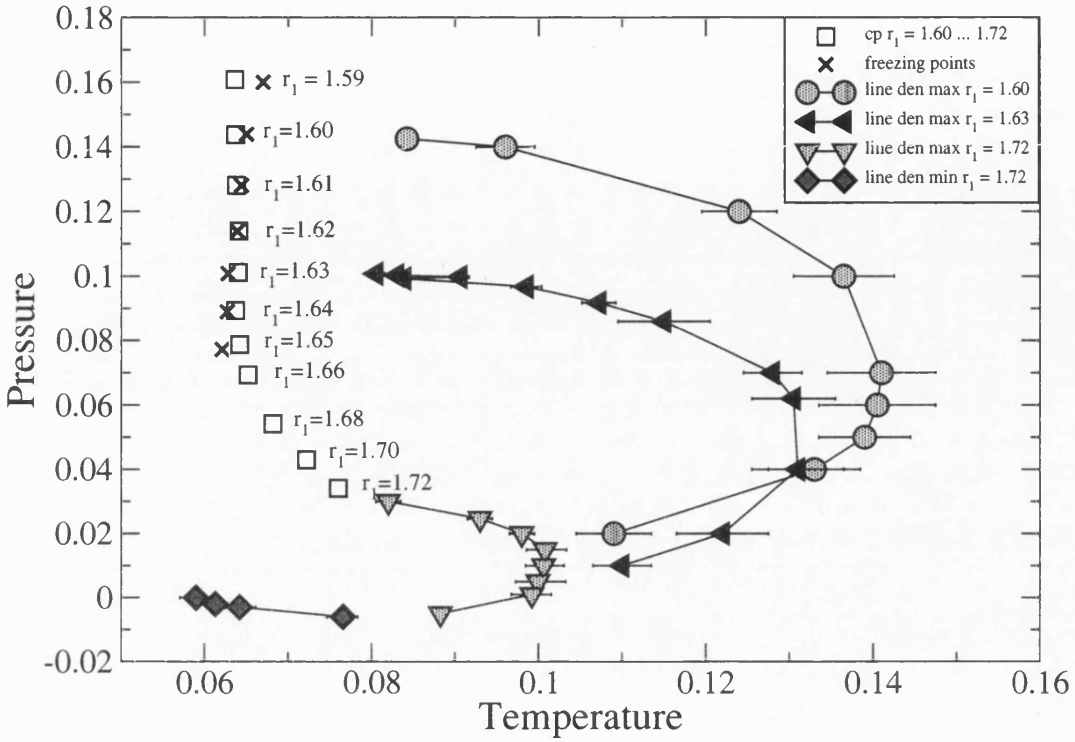

Figure 5.10: Lines of density maxima for a selection of the potentials studied, superimposed upon the phase diagrams of figure 5.6. Also shown for the case $r_1 = 1.72$ is the line of density minima (cf. figure 5.12).

The first thing to note is that there is a stable line of density maxima for the $r_1 = 1.60$ pair potential, previously shown to have a metastable LLCP. At high pressure, this (and the other lines of density maxima) is relatively flat and appears to approach the corresponding LLCP. As the pressure is lowered, the line of TMD moves through a maximum temperature, after which its gradient changes sign and the line bends back upon itself. This maximum temperature increases with decreasing r_1.

Towards lower pressures the line of TMD tends towards lower temperatures and the maximum disappears to become a point of inflexion, just below $P = -0.006$ in the case of $r_1 = 1.72$, as shown in figure 5.11(a). Following isobars at pressures just above this point of inflexion towards lower temperatures, one can see that the density maximum is followed by a density minimum (see figure 5.11). The $P =$

-0.003 isobar is shown individually in figure 5.12. At temperatures lower than the density minimum, the liquid's density increases with decreasing temperature, as is the "normal" behaviour.

In the case of $r_1 = 1.60$ and $r_1 = 1.63$, the line of density minima was short, terminating in an FCC solid. However, in the case of $r_1 = 1.72$ the freezing point was much lower, and so it was possible to follow the line of density minima for a range of temperatures, as plotted in figures 5.10 and 5.11(b), until it could no longer be traced due to its becoming metastable with respect to an HCP solid.

It is interesting to note that the shape of the line of TMD is similar to that found in the molecular dynamics simulations of the TIP5P model of water (see figure 2.5). Also, the line of density maxima smoothly turning into the line of density minima was predicted by the ST2 model of water (see figure 2.4).

Whilst the LLCP becomes metastable for $r_1 \lesssim 1.62$, we have shown that the line of density anomalies is nevertheless observable in the stable liquid region for this value of r_1 and indeed for a considerable range of smaller values. However, since no density anomaly occurs for the Lennard-Jones potential, and since by decreasing r_1 we are making the ramp potentials increasingly like a Lennard-Jones potential, we would expect the density anomaly to disappear if r_1 were sufficiently low, since the Lennard-Jones potential displays no anomalies.

It is not clear how the anomaly would disappear, as both the freezing point and the maximum temperature on the TMD locus were observed to increase with decreasing r_1. Therefore we studied the potentials having r_1 in the range $r_1 = 1.5 - 1.3$ (cf. figure 3.7), which are much closer to the Lennard-Jones limit than the potentials discussed so far.

Whilst studying $r_1 = 1.5$ we noted that the freezing temperature had increased by much more than expected given the previous trend. For $r_1 = 1.4$ very little of the locus of TMD was visible as the maximum temperature of the line of TMD was not much higher than the freezing temperature, and for $r_1 = 1.3$ no density anomalies were identified at all. Thus we concluded that the freezing temperature increased faster than the maximum temperature of the line of TMD with decreasing r_1, which resulted in the stable solid region engulfing the temperature range in which the anomalies would otherwise be found.

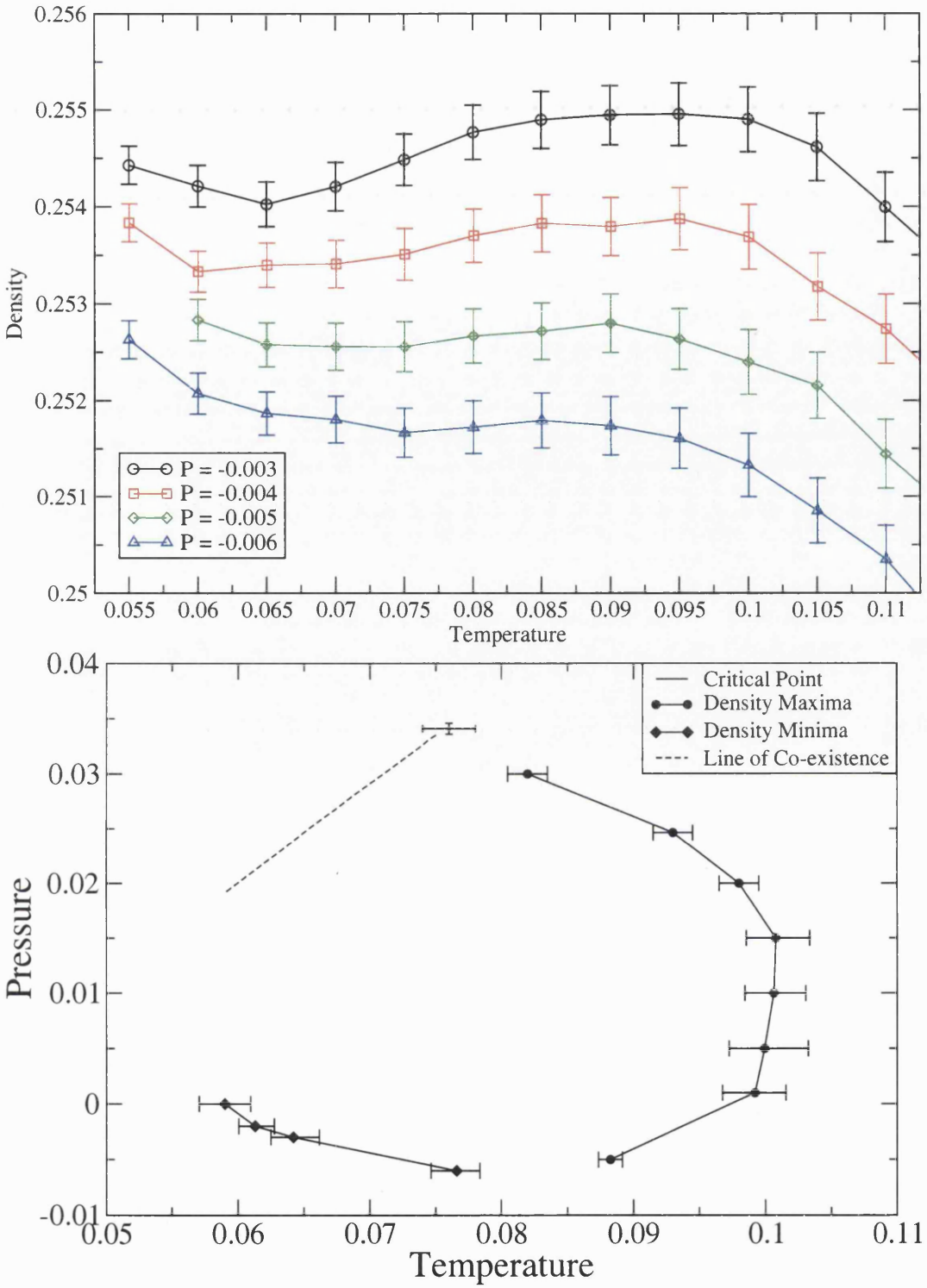

Figure 5.11: **(a)** The measured number density as a function of temperature for a range of pressures, for the potential having $r_1 = 1.72$. Two extrema are found, a maximum and a minimum. For $P = -0.006$, the maximum and minimum are so close together it is almost a point of inflexion. **(b)** The lines of density maxima and density minima for the case $r_1 = 1.72$. The error bars have been shortened through the use of multiple histogram reweighting, as before. Also shown are the LLCP and the LLPT.

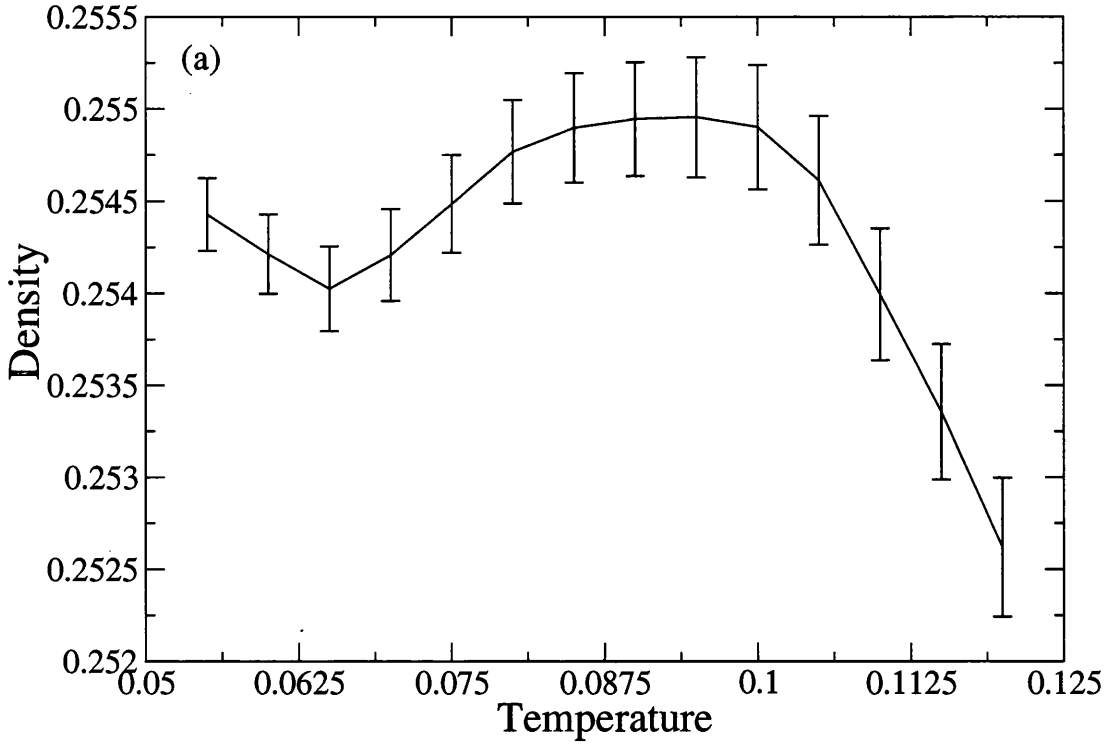

Figure 5.12: The measured number density as a function of temperature at $P = -0.003$, for the potential having $r_1 = 1.72$. Two extrema are found, a maximum and a minimum.

5.3 Discussion and conclusions

We started from the Jagla potential (equation 3.5) with an LLCP in the stable fluid section of the phase diagram, accompanied by a stable LLPT with a positive gradient. Reducing the range of the ramp and attractive component of the pair potential caused the LLCP to move to lower temperatures and higher pressures, just as was seen in Hemmer and Stell's original calculations when they reduced the range of the ramp of their pair potential [49] (see Section 2.2.2). Simultaneously, the freezing point on the LLPT moved to higher temperatures, and thus the LLCP became metastable with respect to a lower-density crystalline solid. The metastable LLCP was accompanied by a metastable LLPT with a negative gradient. The line of density maxima, which occurred in the Jagla model, still existed in the stable fluid region despite the LLCP being metastable. All these features of our new system are in qualitative agreement with the predicted phase diagram of water, and therefore add weight to the "second critical point" hypothesis for water.

The behaviour of the line of density maxima was interesting. As the pair potential was altered, and as the LLCP moved in temperature and pressure, the line of density maxima would also move so that at the high-pressure end of the locus it would always be pointing towards the LLCP. In the TIP5P (figure 2.5) and ST2 (figure 2.4) models of water, and some simpler models (e.g. [76, 44]), the line of density maxima comes very close to the LLCP, while in other models exhibiting LLPT [77, 48, 78] the line of TMD is set to intersect the LLPT far from the LLCP. In the next chapter, we vary Jagla's potential in a different fashion, this time extending the range, and discover that this causes the line of TMD to intersect the LLPT below the LLCP.

Chapter 6

"Detaching" the locus of density maxima

The link between the density anomaly and the critical point seems strong: the line of density maxima points towards the critical point for all the systems studied in the previous chapter. We were therefore interested by Caballero and Puertas' [79] prediction that the density anomaly would cease to exist when r_2 was increased to 3.2. They used Jagla's definition of the pair potential (equation 3.5), so, as well as extending the range of the potential, increasing r_2 also caused the minimum to deepen slightly, and resulted in a slightly steeper ramp.

Caballero and Puertas [79] had approximated the free-energy by applying a first order perturbation to the well-established free-energy of hard spheres. In order to do this they also required the radial distribution function of the repulsive section of the pair potential which they calculated using constant-NVT Monte Carlo simulations. Then they were able to apply the perturbation and plot isotherms of the pressure varying with density. From this they were able to identify phase transitions and density anomalies.

Caballero and Puertas [79] found that increasing r_2 resulted in the LLCP moving to higher temperatures and lower pressures, and the disappearance of the density anomaly.

The equation of state resulting from the application of the perturbation theory

was

$$P = P_{HS} + \rho^2 \frac{\partial \langle u_{total} \rangle_{rep}}{\partial \rho} \tag{6.1}$$

where P_{HS} is the the hard-sphere pressure, and $\langle u_{total} \rangle_{rep}$ is the repulsive component of the total pair-potential. Through Maxwell's relations it was shown that, for there to be a density anomaly,

$$\left(\frac{\partial P}{\partial T}\right)_V < 0 \tag{6.2}$$

Applying this to equation 6.1 requires that

$$\left(\frac{\partial P_{HS}}{\partial T}\right)_V + \rho^2 \left[\frac{\partial}{\partial T}\left(\frac{\partial \langle u_{total} \rangle_{rep}}{\partial \rho}\right)_T\right]_V < 0 \tag{6.3}$$

for there to be a density anomaly. So, as the first term is strictly positive, the second term must be negative and of greater absolute value than the first term. Therefore, if the energy of the system varied too gradually with changes in temperature, a density anomaly could not exist.

6.1 Extending the range

We were interested to know if our simulations would also produce these results, and if so, wondered how the density anomaly disappeared.

6.1.1 Method

Unlike Caballero and Puertas (who varied r_2 as it appears in Jagla's definition of the pair potential, equation 3.5), we varied r_2 as defined in our set of equations, where $U(r)$ was expressed in terms of the depth of the minimum (equation 3.13).

As a result, increasing r_2 only resulted in an extension of the range, while the depth and steepness of the ramp remained constant (see figure 6.1). This is in contrast to Caballero and Puertas' set of pair potentials, which, as mentioned above, had slightly deeper minima when r_2 was larger.

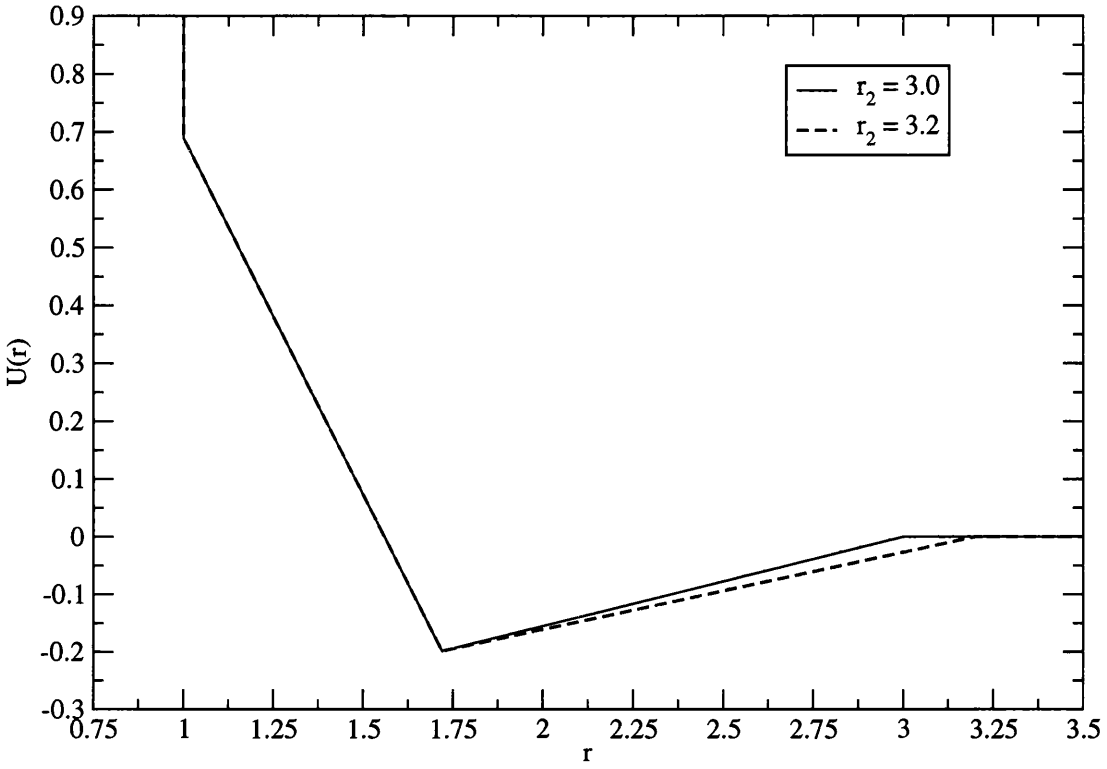

Figure 6.1: Jagla's original potential [2] compared with the potential when $r_2 = 3.2$.

We began with Jagla's original potential and increased r_2 step by step so as not to lose track of the position of the LLCP. Once the LLCP for a given potential was found, we plotted a few points on the density maximum line using multiple histogram reweighting (Section 4.3.6). The gradient of the coexistence line was estimated by extrapolating the histogram at the LLCP (Section 4.3.4).

6.1.2 Results

The results are shown in figure 6.2. The LLCP, LLPT and locus of TMD for $r_2 = 3.00$ are the results found by Wilding and Magee [54]. When $r_2 = 3.03$ the results are fairly similar. But as r_2 is increased further, the line of maximum density can be seen to tend towards a point on the projected coexistence line, and no longer

towards the critical point. Also, the initial gradient of the line of maximum density increases with r_2, indicating that the intersection with the coexistence line occurs closer and closer to the point on the TMD line where its gradient changes sign. The point of maximum temperature on the line of TMD can be seen to occur at increasingly low temperatures. As only one of the calculated isobars exhibited a density maximum for the $r_2 = 3.15$ potential, we suggest this is the point of maximum temperature, only just stable at the projected LLPT. Larger values of r_2 exhibited no density maxima at all, as predicted by Caballero and Puertas [79]. We now see that this is because the locus of TMD becomes metastable with respect to the HDL.

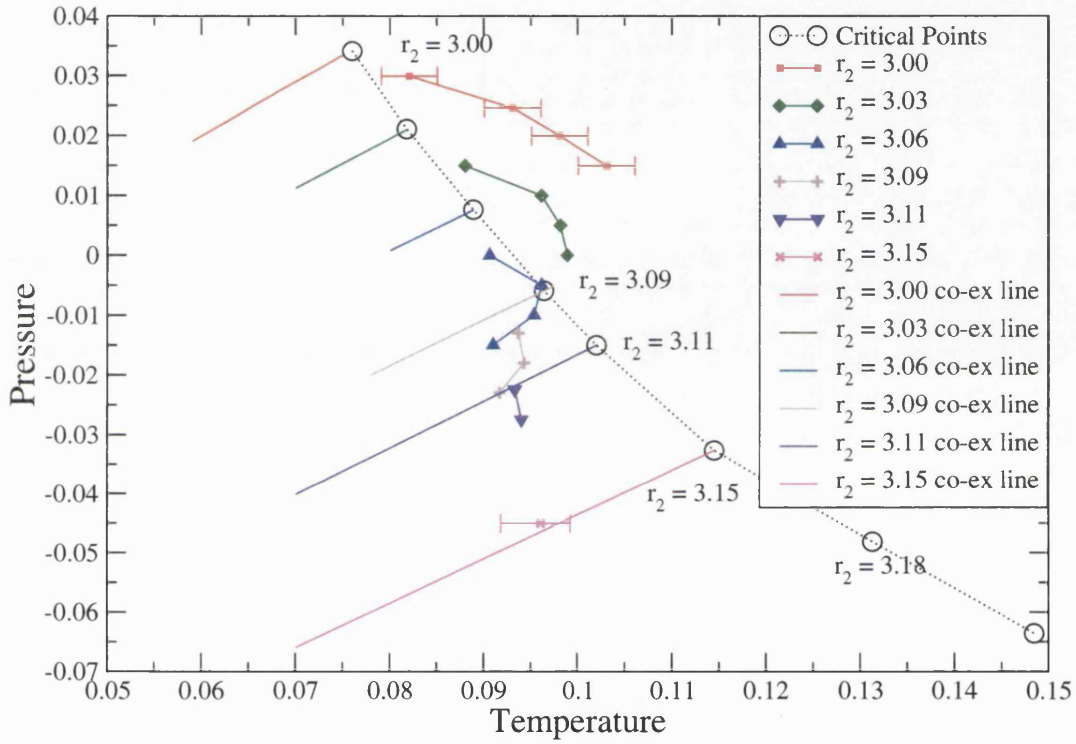

Figure 6.2: The LLCP, extrapolated line of coexistence and first few points on the line of density maxima are plotted for each pair potential studied. The error bars on the critical points are comparable to the symbol size. The error bars plotted on the first ($r_2 = 3.00$) line of density maxima are representative of the error bars on the other lines of density maxima.

As the locus of the density maxima moves to lower temperatures as r_2 is increased, the point of contact with the LLPT occurs at increasingly low temperatures relative to the critical temperature. Thus, the locus appears to "detach" from the LLCP. The locus disappears completely as the maximum temperature of the locus becomes lower than the temperature at the same pressure on the coexistence

line.

6.1.3 Discussion

It is unclear why the locus of TMD moves to lower temperatures relative to the LLCP. It may be a combination of the LLCP moving to higher temperatures with increasing r_2 (also predicted by Caballero and Puertas [79]), whilst the locus of the TMD moves to lower temperatures.

This trend was already seen in the previous chapter, where, as we reduced r_1, we also reduced r_2. It was seen in figure 5.10 that the temperature of the LLCPs for $r_1 = 1.68$, 1.70 and 1.72 increased as r_1 and r_2 increased, while the pressure decreased. A similar trend had also been recorded in the experiments carried out by Skibinsky *et al.* [57] (see Section 2.2.2): when the width of the square well was increased, the LLCP moved to lower pressure and higher temperature.

The movement of the locus of TMD to lower temperatures was also seen in the previous chapter: the maximum temperature of the locus of TMD for $r_1 = 1.72$ is much lower than that of $r_1 = 1.63$, which is in turn lower than that of $r_1 = 1.60$ (see figure 5.10).

It may be significant that changing the potential as we have in this section results in the virial coefficient, B, also changing. When $r_2 = 3.0$, $B = -0.76r_0^3$ as before, but increasing r_2 to 3.11 gave $B = -1.27r_0^3$, and when $r_2 = 3.18$, $B = -1.61r_0^3$. As the range of the attraction increases, the second virial coefficient becomes more negative.

6.2 Reducing the range

We carried out another experiment to examine further the link between the critical point and the locus of density maxima. Starting with the potential $r_2 = 3.11$ (which produces a line of density maxima that intersects the LLPT below the LLCP), we reduced r_1 and r_2 whilst maintaining the second virial coefficient – in the same way as we did for the experiment detailed in Chapters 3 and 5 – in

order to see if the high-pressure end of the line of density maxima would re-attach itself to the critical point.

6.2.1 Method

We took the interaction potential with parameters $r_2 = 3.11$, $r_1 = 1.72$, $U(r_1) = 0.1984$, $U(r_0) = 0.69$ and treated it exactly as we did Jagla's potential (equation 3.5) in Section 3.3.

Specifically, the second virial coefficient was calculated as before (detailed in Section 3.3), and came to $-1.27r_0^3$. A Lennard-Jones approximation with the same virial coefficient was designed. A line was then drawn between its minimum and that of the $r_2 = 3.11$, $r_1 = 1.72$ potential. This line, calculated to be

$$D(r_1) = 1.39667 - 0.69667r_1 \tag{6.4}$$

(where $D(r_1) = -U(r_1)$ is the magnitude of the depth at $r = r_1$), is the line on which all the minima in the family of potentials are set to lie. Thus, for a given r_1, the depth $U(r_1)$ was calculated from equation 6.4, and then r_2 changed to the value that maintained the virial coefficient at $-1.27r_0^3$. A selection of potentials, alongside the Lennard-Jones potential scaled to have the same virial coefficient, are shown in figure 6.3. Table 6.1 contains the parameters of all the potentials studied.

r_1	$D(r_1)$	r_2
1.72	0.1984	3.11
1.7	0.212333	3.01774
1.68	0.226267	2.93336

Table 6.1: The parameters of the three potential wells studied in this section. When put into equation 3.13 they produce ramp potentials with a second virial coefficient of approximately $-1.27r_0^3$.

Then, as before, the critical point was located for each potential studied, and a section of the locus of density maxima was calculated using multiple histogram

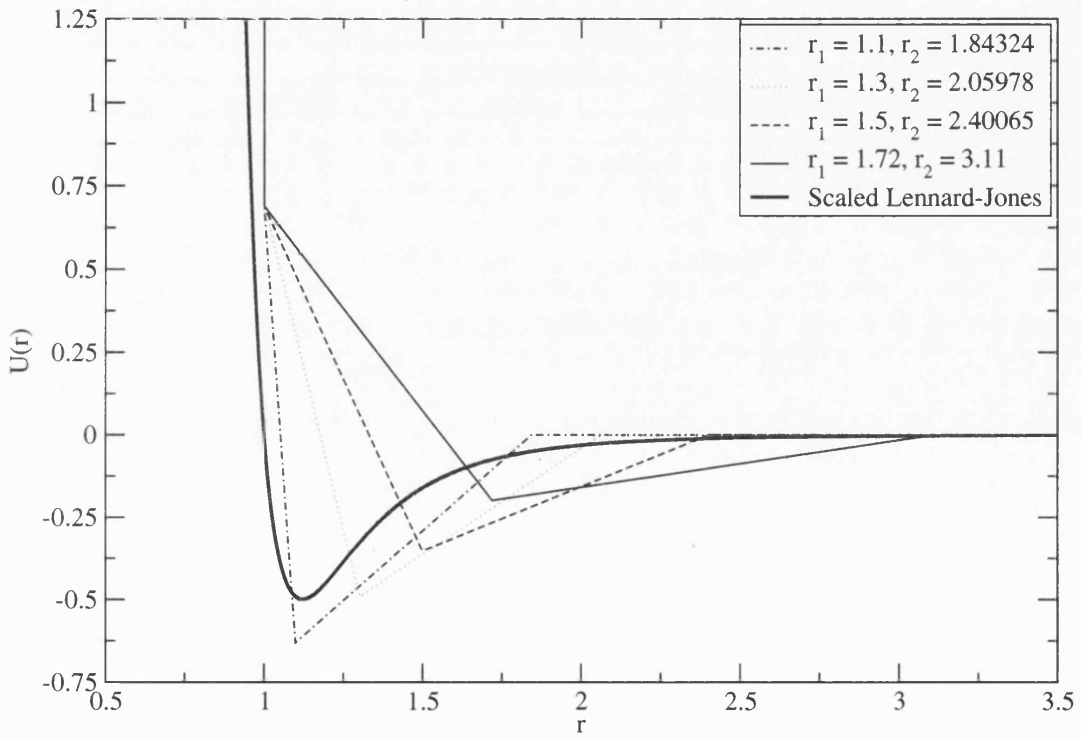

Figure 6.3: A selection of ramp potentials, and a scaled Lennard-Jones potential, all with the same virial coefficient. The line connecting the minima of the ramp potentials is given by equation. 6.4.

reweighting (Section 4.3.6). The line of coexistence was estimated by extrapolating the density histogram at the critical point as described in Section 4.3.4.

6.2.2 Results

The results, in figure 6.4, show that as r_1 and r_2 are decreased, the initial gradient of the line of density maxima decreases, and the line begins to tend towards the critical point once more. Comparing the sections plotted here with the general shape of the loci of density maxima we have seen before (see figures 5.10 and 6.2), one can predict that the maximum temperatures of the loci of TMD are greater for smaller values of r_1. In addition, the temperature of the critical point can be seen to decrease with decreasing r_1.

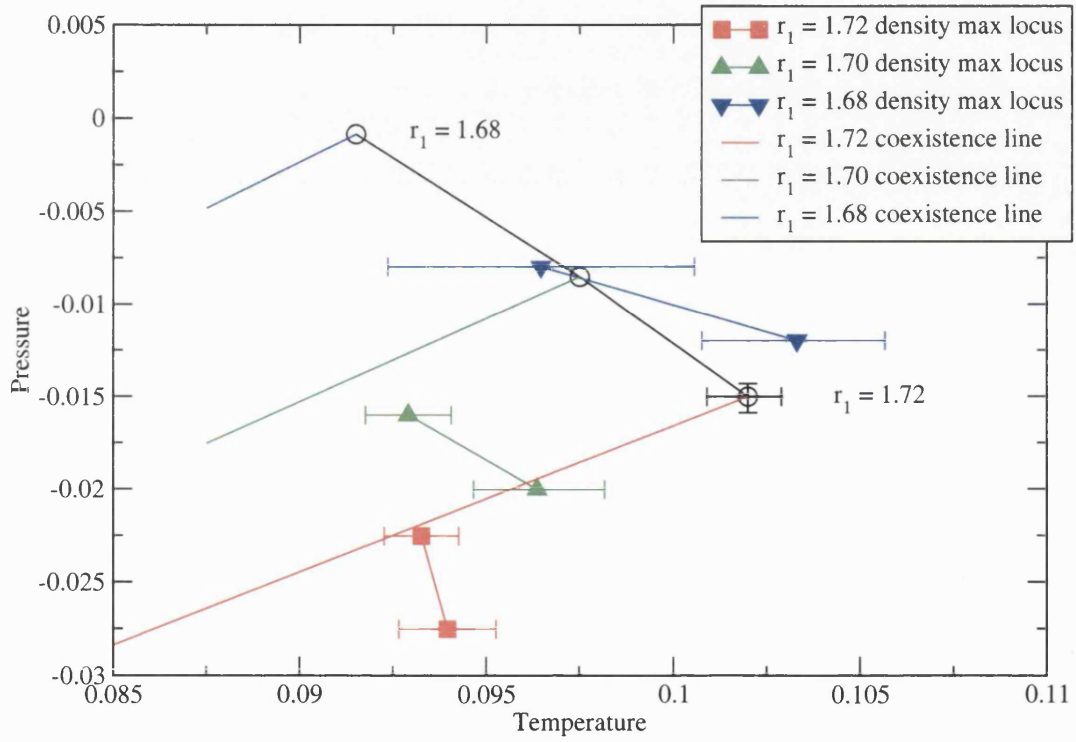

Figure 6.4: The LLCP, two points on the line of density maxima, and an extrapolation of the line of coexistence are plotted for the three potentials detailed in Table 6.1.

6.2.3 Discussion

As before, it seems that when the parameters of the potential are changed such that the LLCP is at higher temperatures, the locus of density maxima moves to lower temperatures. Conversely, when the LLCP is at lower temperatures, the maximum point on the locus of TMD is at higher temperatures. Thus LLCPs that occur at lower temperatures have larger loci of density maxima. The gradient of the locus of density maxima approaches zero at the high pressure, low temperature end. The general trend is that if this zero-gradient section of the locus of density maxima is stable in the LDL region, it will point towards the LLCP. However, if the locus has shifted to lower temperatures relative to the critical point, and this zero-gradient section is no longer in the stable LDL region, then the locus does not point towards the critical point, but rather meets the LLPT at a subcritical temperature and pressure.

In this section we have kept the virial coefficient of the pair potential constant, so the movement of the locus of density maxima relative to the LLCP that we saw in the previous section cannot be due only to the change in virial coefficient.

6.3 Lowering $U(r_0)$

Another experiment we carried out was to lower the value of $U(r_0)$: that is, decrease the height of the core-softening ramp. As equation 3.13 shows, $U(r_0)$ was originally set to 0.69. We changed this number, whilst keeping all the other parameters constant at the values set for Jagla's potential in equation 3.13. The potential for which $U(r_0) = 0.60$ is plotted with Jagla's potential ($U(r_0) = 0.69$) in figure 6.5. Effectively, decreasing $U(r_0)$ reduces the energy difference between the two preferred separation distances.

As before, the potential was altered step by step, so it was always easy to locate the LLCP in the new system. The LLCP, two points on the line of TMD and a projection of the LLPT were calculated for each potential in the same manner as in the previous section.

Reducing the height of the top of the ramp can be seen (figure 6.6) to move the

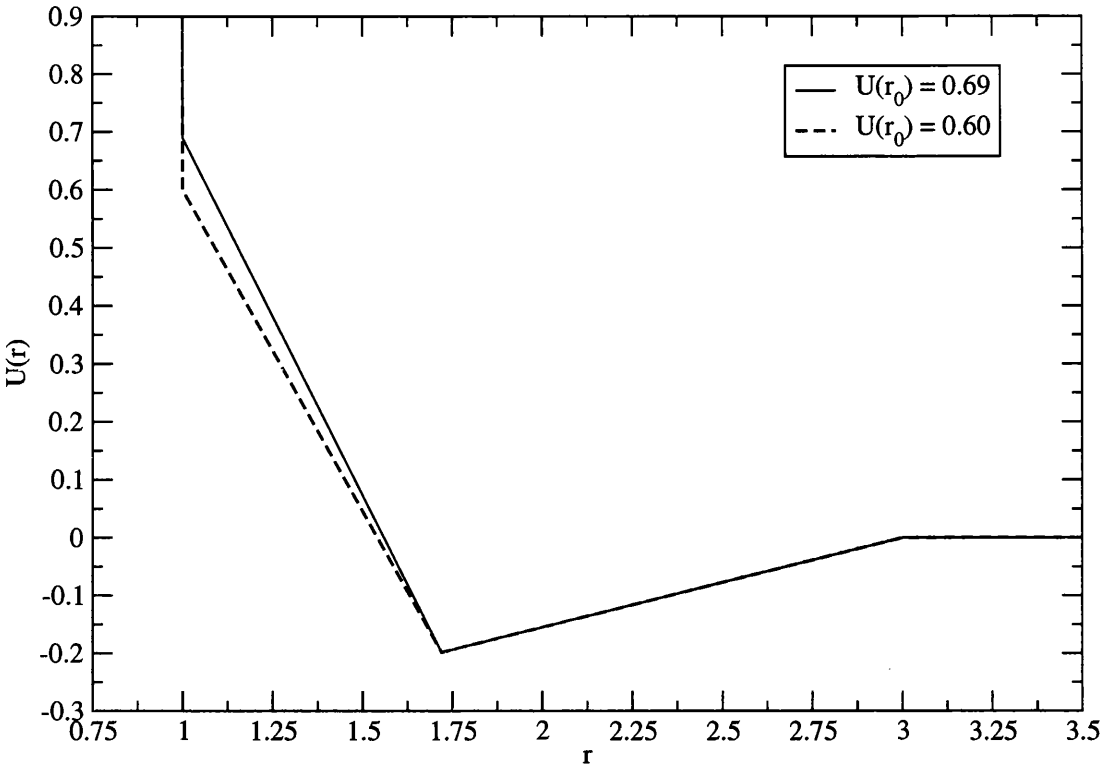

Figure 6.5: Jagla's potential ($U(r_0) = 0.69$) is plotted alongside the potential $U(r_0) = 0.60$.

LLCP to higher temperatures and lower pressures. The section of locus of TMD plotted for each potential has a steeper gradient if the height of the ramp is lower, suggesting that the locus of TMD moves to lower temperatures as the height of the ramp is lowered.

Reducing the height of the top of the ramp was seen to have an effect on the temperature and pressure of the LLCP similar to that created by extending the range (see Section 6.1). As was found in Sections 6.1 and 6.2, the higher the temperature of the LLCP, the further from the LLCP is the intersection between the LLPT and the line of TMD.

These results are in line with Hemmer and Stell's results using the ramp potential [49], outlined in Section 2.2.2, which showed that lowering the height of the ramp would result in the LLCP occurring at higher temperatures and lower pressures.

Our results are also in line with experiments on square-well potentials [57], again mentioned in Section 2.2.2, which found that a lower shoulder height would also

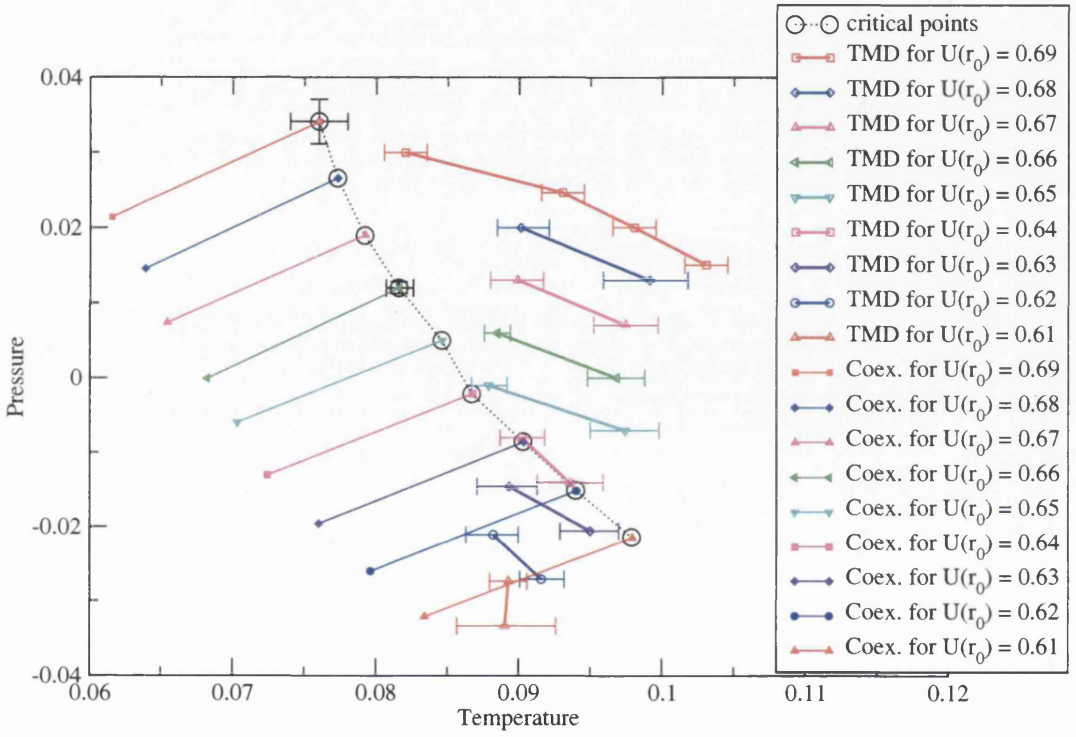

Figure 6.6: Liquid-liquid critical points (LLCP) and sections of the line of temperature of maximum density (TMD) are plotted for a selection of potentials, along with the extrapolated line of coexistence.

result in the LLCP occurring at higher temperatures and lower pressures.

It may be significant that reducing $U(r_0)$ caused the virial coefficient to decrease, just as increasing the range had. When $U(r_0) = 0.69$ the virial coefficient was $B = -0.76r_0^3$ as before, but when $U(r_0)$ is 0.61 the virial coefficient is $-0.98r_0^3$.

6.4 Increasing r_1

Using the definition of the original family of potentials (equation 3.13), in this experiment we increased r_1, whilst keeping the virial coefficient constant. As the range increases with r_1, we would expect behaviour similar to that seen in Section 6.1.

The parameters of the pair potentials used are shown in the Appendix. The LLCP for each potential was found in the usual manner, and for roughly every second potential a section of the locus of TMD was calculated.

As figure 6.7 shows, the trend in the temperature and pressure of the LLCP was initially as expected: moving toward higher temperatures and lower pressures with increasing r_1. However, around $r_1 = 1.9$ the trend in temperature reversed: further increases in r_1 saw the temperature of the LLCP decrease.

The trend in the maximum temperature of the locus of TMD also saw a change. The maximum temperature of the locus for $r_1 = 1.76$ was lower than that of $r_1 = 1.72$, as was expected given the trend in Section 6.1. However, the maximum temperature of the locus of TMD of the $r_1 = 1.80$ potential was actually slightly higher than that of the $r_1 = 1.76$ potential. The maximum temperature of the $r_1 = 1.84$ locus was higher still, and the maximum temperature of the $r_1 = 1.88$ locus was even higher. However, the maximum temperature for $r_1 = 1.94$ was lower than that of $r_1 = 1.88$. We expect that this is due to the temperature of the LLCP for $r_1 = 1.94$ being less than that of $r_1 = 1.88$.

It is clear – especially when looking at the loci of TMD for $r_1 = 1.72$, $r_1 = 1.76$, $r_1 = 1.8$ and $r_1 = 1.94$ (for which the TMD at pressures close to the LLCP were calculated) – that the locus of TMD always tends towards the LLCP at its higher

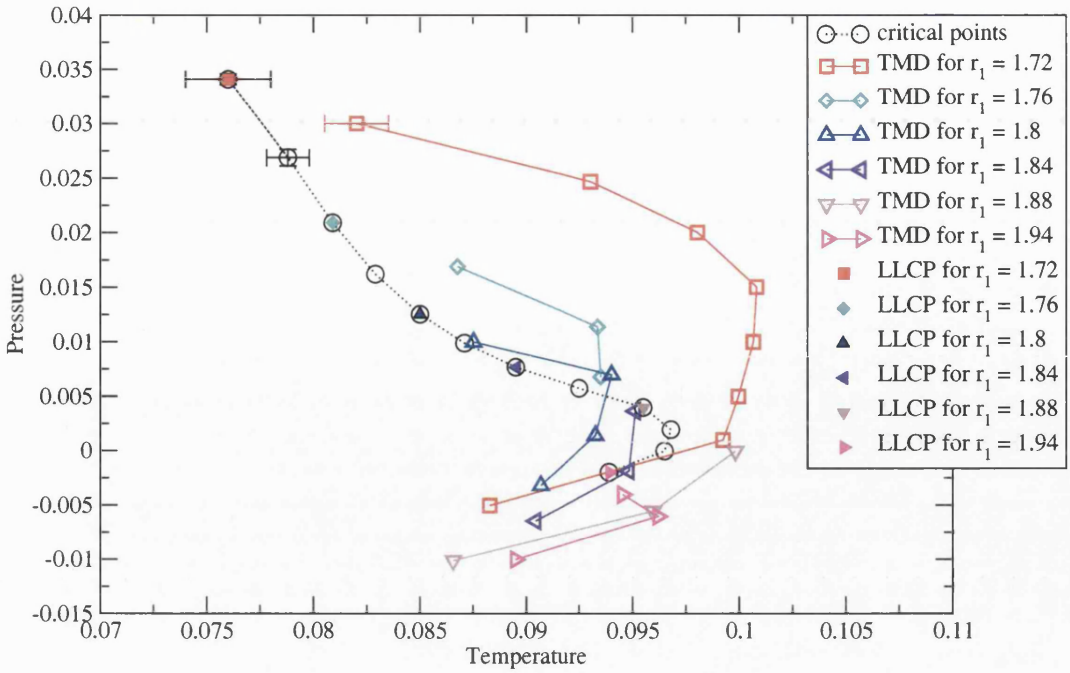

Figure 6.7: The LLCPs for $r_1 = 1.72$, 1.74, 1.76, 1.78, 1.8, 1.82, 1.84, 1.86, 1.88, 1.9, 1.92 and 1.94, and lines of TMD for selected potentials with $r_1 \geq 1.72$. The error bars shown are typical of the error bars on the rest of the data.

pressure end. At no point does the locus of TMD appear to intersect the LLPT at a lower temperature than the critical temperature.

The LLPTs were not plotted in figure 6.7 as this would complicate an already busy graph. However we did calculate their gradient using histogram reweighting as before, and plotted the results against r_1, along with previous results for $r_1 < 1.72$, as shown in figure 6.8. The gradient of the LLPT was at a maximum around $r_1 = 1.7$, and then began to decrease again. By $r_1 = 1.92$ the trend was beginning to level off. If r_1 were to be increased further, the gradient of the LLPT might be seen to increase once more.

Although the range of the potential far exceeded $r_2 = 3.2$, a density anomaly was always present and the loci of TMD tended towards the LLCP for all the values of r_1 studied. This is due to maintaining the virial coefficient through a combination of decreasing the depth of the minimum of the pair potential, D, and increasing the radius at which the minimum potential energy was felt, r_1. The trend of the gradient of the LLPT seen in Chapter 5 was reversed, as was the trend in the maximum temperature of the locus of TMD.

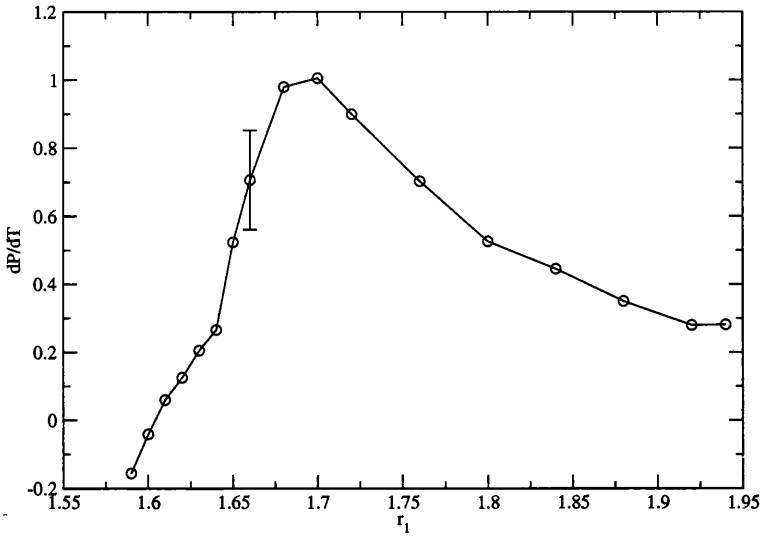

Figure 6.8: A plot of the gradient of the LLPT in the P-T plane for the full range of potentials studied with a virial coefficient of 1.52.

6.5 Conclusion

We have found that both extending the range and reducing the height of the ramp have comparable effects on the phase diagram: the LLCP is moved to higher temperature and lower pressure while the locus of TMD moves to lower temperatures and pressures. Significantly, we have seen that only very small changes in the pair potential (about 5% in the case of extending the range; about 14% in the case of reducing the height of the ramp) cause the density anomaly to detach itself from the critical point. Both of these changes to the pair potential reduce the relative contribution of the repulsive element of the potential to the virial coefficient, resulting in a lower value for the virial coefficient. Indeed, this may be particularly significant in the case where the range of the potential is extended, as a 6% increase in r_2 results in a huge 111% decrease in the virial coefficient.

Also, both extending the range and decreasing the height of the ramp have the effect of increasing the angle between the lines that meet at the minimum of the potential, shown in figure 6.9, which in turn increases the range of separation distances available at low energies. Increasing r_1 whilst maintaining the virial coefficient also increases this angle.

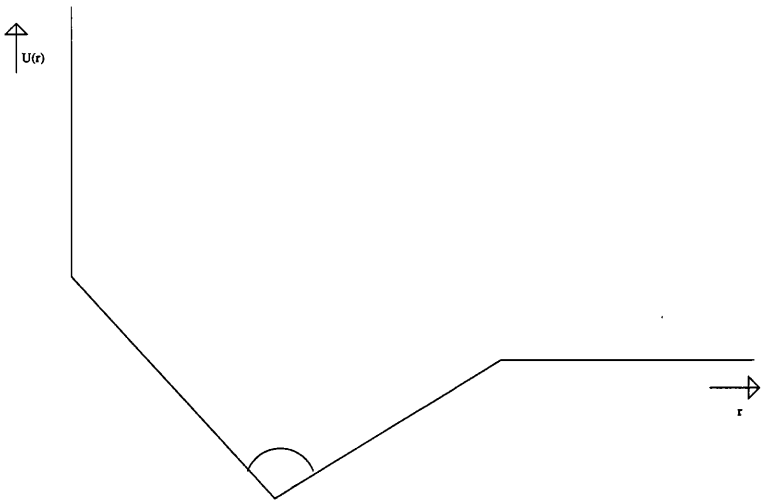

Figure 6.9: A sketch showing the angle referred to in the text.

The trend in the movement of the LLCP was seen to be reversed if r_1 was *decreased* whilst maintaining the virial coefficient of the $r_2 = 3.11$ potential (Section 6.2). Specifically, the locus of TMD reattached itself to the LLCP, showing that it was not just the change in the virial coefficient that had caused the density anomaly to detach in Sections 6.1 and 6.3.

It was anticipated that increasing r_1 whilst maintaining the virial coefficient of Jagla's potential would see the LLCP move to higher temperatures and lower pressures as before. Although this was the case initially, the LLCP began to move to lower temperatures when r_1 exceeded 1.9, and the locus of TMD moved to higher temperatures when r_1 exceeded 1.8, but moved to lower temperatures again when it reached $r_1 = 1.94$. Throughout, the locus of TMD remained attached to the LLCP at its high pressure end.

It is interesting that a large change in the parameters of Jagla's potential, with no change in virial coefficient, does not remove the density anomaly, while a very small change in a parameter of the potential, that also changes the virial coefficient, eliminates the density anomaly altogether. Figure 6.10 shows the relevant potentials together for comparison. It would appear that the deciding factor is the virial coefficient, and yet, in Section 6.2, we kept the virial coefficient constant and nevertheless saw the position of the locus of TMD change relative to the LLCP.

As regards the broader question of exactly what it is that determines which

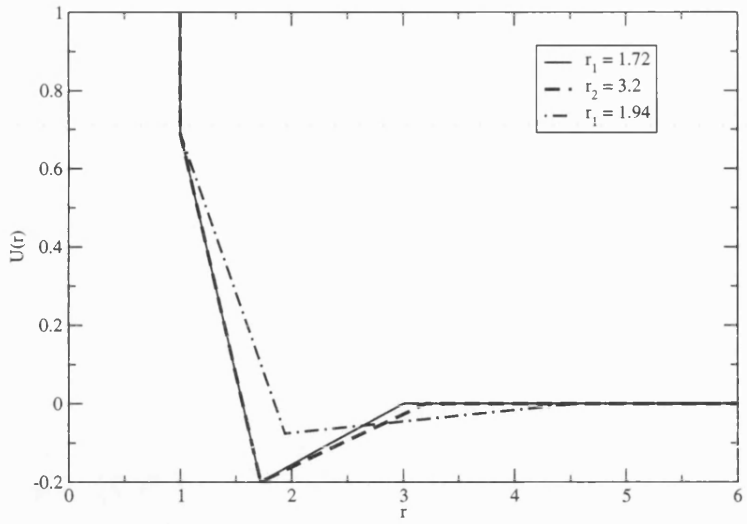

Figure 6.10: Jagla's potential compared with the potential with range $r_2 = 3.2$, and with the potential with the same virial coefficient as Jagla's potential, but with $r_1 = 1.94$.

potentials show a density anomaly and which do not, the answer still eludes us; but we have shown a number of cases where the density anomaly remains, and a number where it disappears. Perhaps closer examination of the energy and entropy changes involved in these systems will reveal the determining factor.

Chapter 7

Square well

7.1 Introduction

Recent studies (references [59] and [60], mentioned in the Literature Review, Section 2.2.2) have used a different isotropic core-softened potential altogether: instead of the core being softened by a ramp as it is in Jagla's potential, it is softened by a square shoulder, and the minima take the form of a square well. Specifically, the potential can be described by:

$$U(r) = \begin{cases} \infty & \text{when } 0 < r \leq \sigma_0 \\ \epsilon_r & \text{when } \sigma_0 < r \leq \sigma_1 \\ -\epsilon_a & \text{when } \sigma_1 < r \leq \sigma_2 \\ 0 & \text{when } r > \sigma_2 \end{cases} \tag{7.1}$$

where $U(r)$ is the interaction energy of two particles whose centres are separated by the distance r, σ_0 is the hard-core diameter, σ_1 is the width of the repulsive shoulder, σ_2 is the width of the attractive well, ϵ_r is the shoulder height, and ϵ_a is the well depth. The parameters were set to $\sigma_1/\sigma_0 = 2$, $\sigma_2/\sigma_0 = 2.2$, and $\epsilon_r/\epsilon_a = 0.5$. The potential is shown in figure 2.8, in the Literature Review. The units of temperature are ϵ_a/k_B. Those of density are σ_0^{-3}. Energy is measured in units of ϵ_a and pressure in units of ϵ_a/σ_0^3.

The studies, the first [59] using molecular dynamics (MD) in the constant-NVT ensemble and the second [60] using Gibbs Ensemble Monte Carlo (GEMC), produced similar results, although exact values differed slightly. The potential exhibited HDL-LDL and LDL-gas phase transitions, but no density anomalies.

The study by Franzese *et al.* [59] found the critical points to be metastable with respect to a crystal. The authors deemed the fluid to be stable if a crystal seed shrank at a given pressure and temperature, and deemed the fluid to be metastable if the crystal grew. Neither study, however, seemed to be hampered by the metastability, perhaps because neither method provided an easy transition from the fluid to the crystal phase.

Our aim was to reproduce the results, and then look again for a density anomaly.

7.2 Method

We used the constant-NPT Monte Carlo (MC) simulation method, as used in Chapters 5 and 6, merely altering the code to use the square potential in place of the ramp potential.

Simulations were begun at the temperatures and pressures where the previous studies [59, 60] had predicted critical points. The resulting volume histogram, $p(V)$, was extrapolated to estimate the temperature and pressure of the critical points that our method generated. Simulations at these temperatures and pressures were used to refine the estimates and further simulations were carried out at the improved estimates of the critical temperature and pressure. This cycle would have been repeated until the universal shape of the critical point was observed in $p(V)$, had it not been for the problems detailed below.

7.3 Results

It proved very difficult to simulate this system in the constant-NPT ensemble. The simulations were slow, resulting in infrequent fluctuations between phases,

and making it hard to get an accurate position for the critical points on the phase diagram.

In addition, many of the simulations at low density froze to a solid with a density of around 0.275 (see figure 7.1). Although it was clearly a solid (with the characteristic low volume fluctuations, indicating low compressibility) the crystal was not sufficiently defined to be identified.

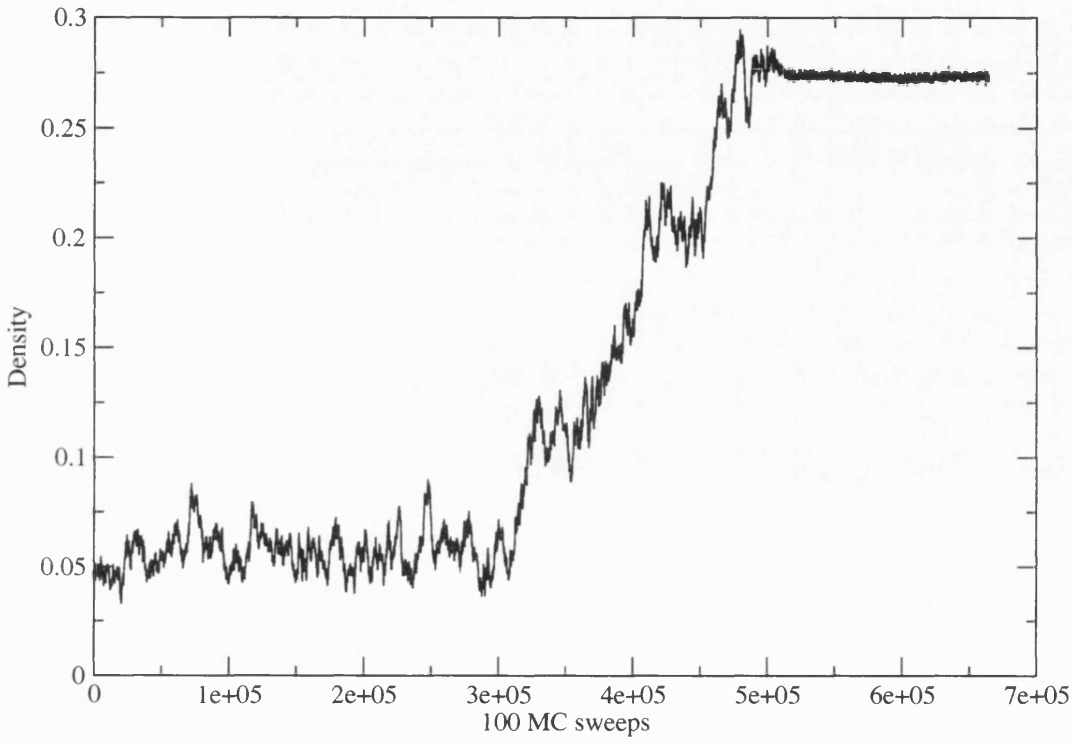

Figure 7.1: The "time"-evolution of the density of a simulation at $T = 0.59$, $P = 0.014$ – an example of when the system froze.

However, despite these difficulties, the temperature and pressure of each critical point was narrowed down in the usual way. But the quality of the data was not sufficient to be sure that we had found the critical points. Far greater computing power than was available would be required. Here we present the results of two simulations that did appear to be close to the gas-LDL and HDL-LDL critical points.

Figure 7.2(a) shows the progression of the simulation near the gas-LDL critical point ($T = 0.6, P = 0.016676$). Around five full traverses of the density range take place over 1.8×10^8 Monte Carlo sweeps, which took around 40 days to simulate

on a single 1.7 GHz processor. However, at least 10 full traverses are required to get sufficiently accurate statistics to pin-point the critical point. As can be seen in figure 7.2(b), the resulting histogram is extremely choppy, highlighting the absence of sufficient data to get an accurate estimate of the critical point. The average density was calculated to be $\rho = 0.111$.

Similarly, simulations at $T = 0.698$, $P = 0.1459$ seem close to the HDL-LDL critical point, but again the traverses are too infrequent (figure 7.3(a)). The histogram of the density (figure 7.3(b)) was rough, and there was insufficient data from which to extrapolate to get a good estimate of the temperature and pressure of the critical point. The average density was $\rho = 0.316$.

Nevertheless, plotting the temperature and average density alongside the results quoted in papers [60] and [59] (figure 7.4) shows that our results are close to theirs.

7.4 Discussion

Despite the poor quality of the data, our results were nevertheless very close to those of the other papers that study this interaction potential.

The reason for the poor quality of data was the low acceptance rates of volume changes, due to the low temperatures at which the critical points lay. The other methods involved constant volume simulations in the case of the MD calculations, and particle and volume exchange between two boxes of constant total volume in the case of the GEMC simulations. Thus neither of the previous methods suffered from low acceptance rates to the same extent.

We concluded that the simulations took too long to obtain more accurate estimates of the critical point, or to examine the possibility of finding a density anomaly.

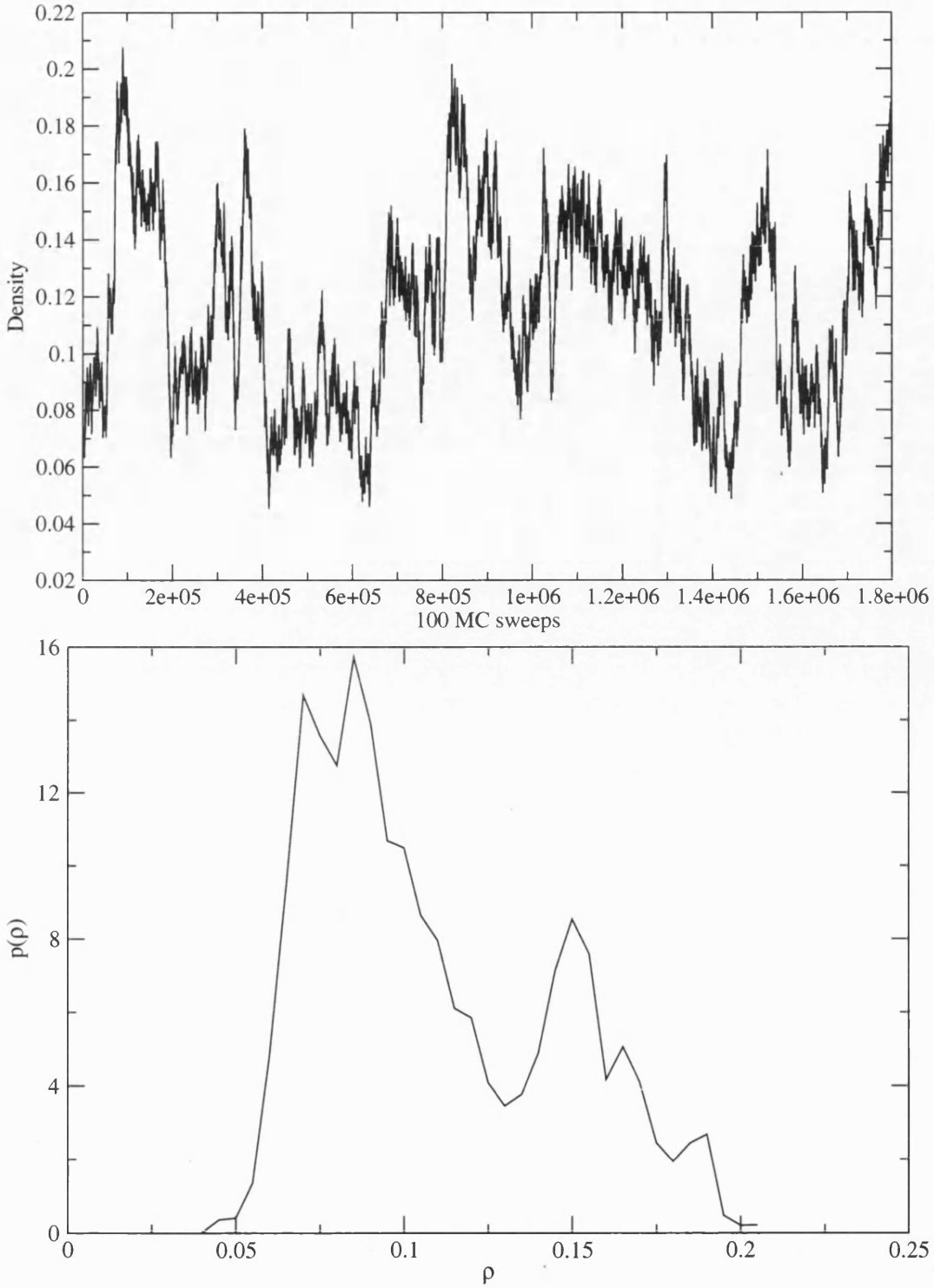

Figure 7.2: **(a)**The "time"-evolution of the density of a simulation at $T = 0.6$, $P = 0.016676$. **(b)** The density histogram of the "time"-evolution plot.

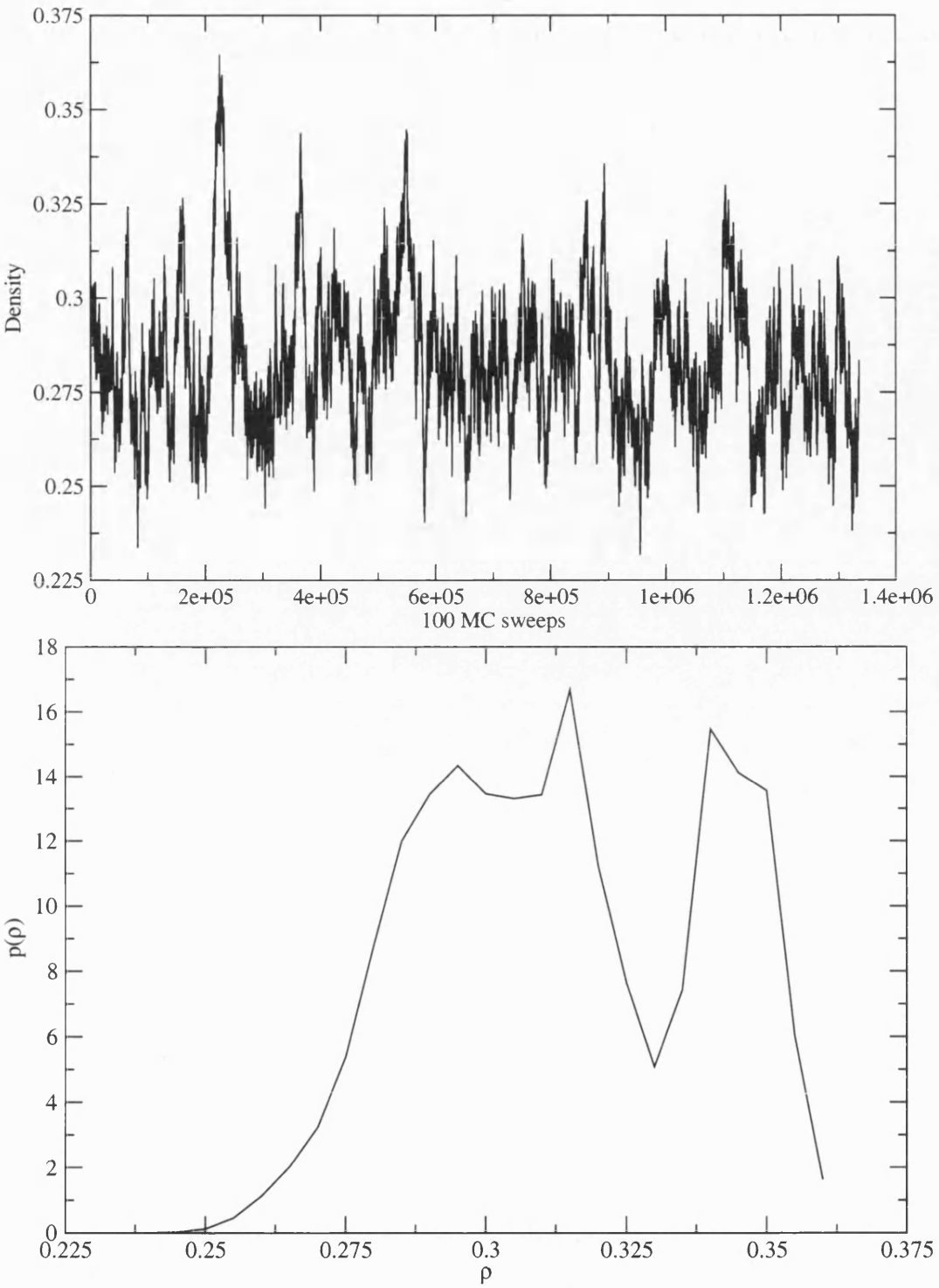

Figure 7.3: **(a)**The "time"-evolution of the density of a simulation at $T = 0.698$, $P = 0.1459$. **(b)** The density histogram of the "time"-evolution plot.

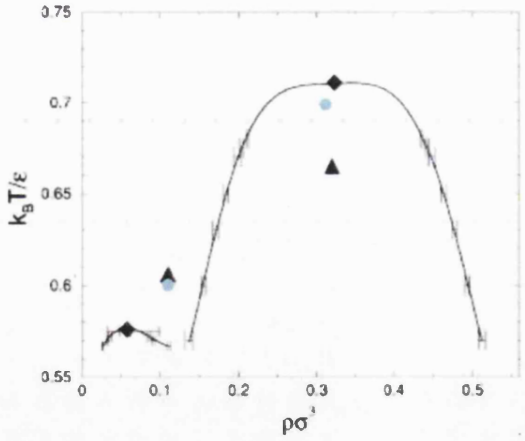

Figure 7.4: Figure 6 from [60] with our results superimposed. It is the "Fluid phase diagram in the temperature-density plane." The error bars are the coexistence densities of the LDL-gas and HDL-LDL coexistence, calculated using GEMC [60]. The diamonds are the GEMC critical points (LLCP: $T_C = 0.711 \pm 0.001$, $P_C = 0.185 \pm 0.024$. LGCP: $T_C = 0.576 \pm 0.002$, $P_C = 0.012 \pm 0.001$) [60] while the triangles are the MD critical points (LLCP: $T_C = 0.665 \pm 0.005$, $P_C = 0.1 \pm 0.01$. LGCP: $T_C = 0.606 \pm 0.004$, $P_C = 0.018 \pm 0.001$) [59]. The blue circles are our results, calculated using constant-NPT MC.

7.5 A further experiment

Concerned that the metastability of the system might have contributed to our difficulties, we simulated a square well potential which had been studied using molecular dynamics by Skibinsky *et al.* [57]. Using the parameter set $\sigma_1/\sigma_0 = 1.7$, $\sigma_2/\sigma_0 = 2.4$, and $\epsilon_r/\epsilon_a = 2$, Skibinsky and his co-authors identified a gas-LDL and an LDL-HDL critical point and stated that there was "no spontaneous crystal nucleation", suggesting that both critical points were stable with respect to the solid.

We set off a simulation run at $T = 0.74$ and $P = 0.07$, corresponding to the parameters at which they had found the LDL-HDL critical point. After 38 days (1.56×10^8 MC steps) the system had performed 10 full traverses of the density range, as shown in figure 7.5. Using histogram reweighting, the critical point was found to be at $T = 0.741 \pm 0.013$, $P = 0.0692 \pm 0.0084$. The histogram at the simulation temperature and pressure is shown alongside the extrapolated histogram in figure 7.6.

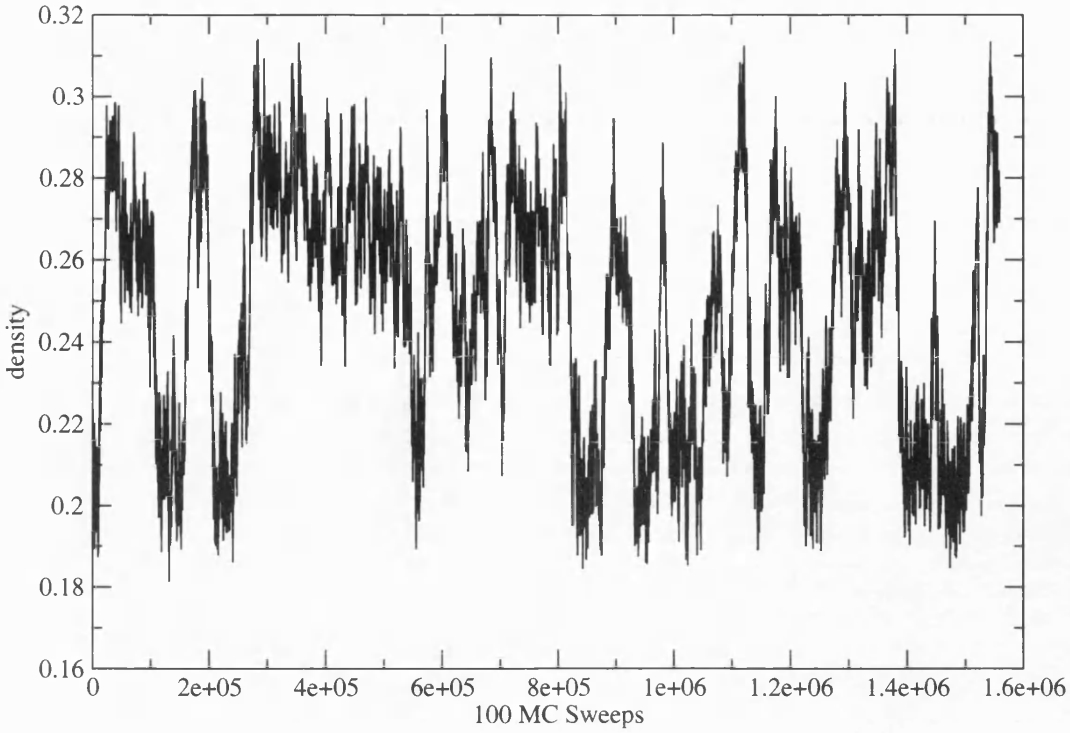

Figure 7.5: The "time"-evolution of the density of the system at $T = 0.74$ and $P = 0.07$ for the parameter set $\sigma_1/\sigma_0 = 1.7$, $\sigma_2/\sigma_0 = 2.4$, and $\epsilon_r/\epsilon_a = 2$.

The error bars of our result overlap with the error bars of their result ($T_C = 0.74 \pm 0.01$, $P_C = 0.07 \pm 0.01$) and we can conclude that the two methods agree. However, despite the system being stable, our method proved to be too inefficient for this system to merit further investigation.

7.6 Comparisons with Jagla's interaction potential

The reasons for the relative inefficiency of the square-well isobaric-isothermic simulations when compared with the simulations of Jagla's potential in the same ensemble are two-fold. Firstly, the pressure of the LDL-HDL critical point is twice that of the LDL-HDL critical point of the Jagla potential. This alone may make the volume moves too unlikely to be accepted. In addition, the shape of the square-well potential, when compared with the Jagla potential, reveals the second reason. In figure 7.7 we have scaled the square-well potential studied in

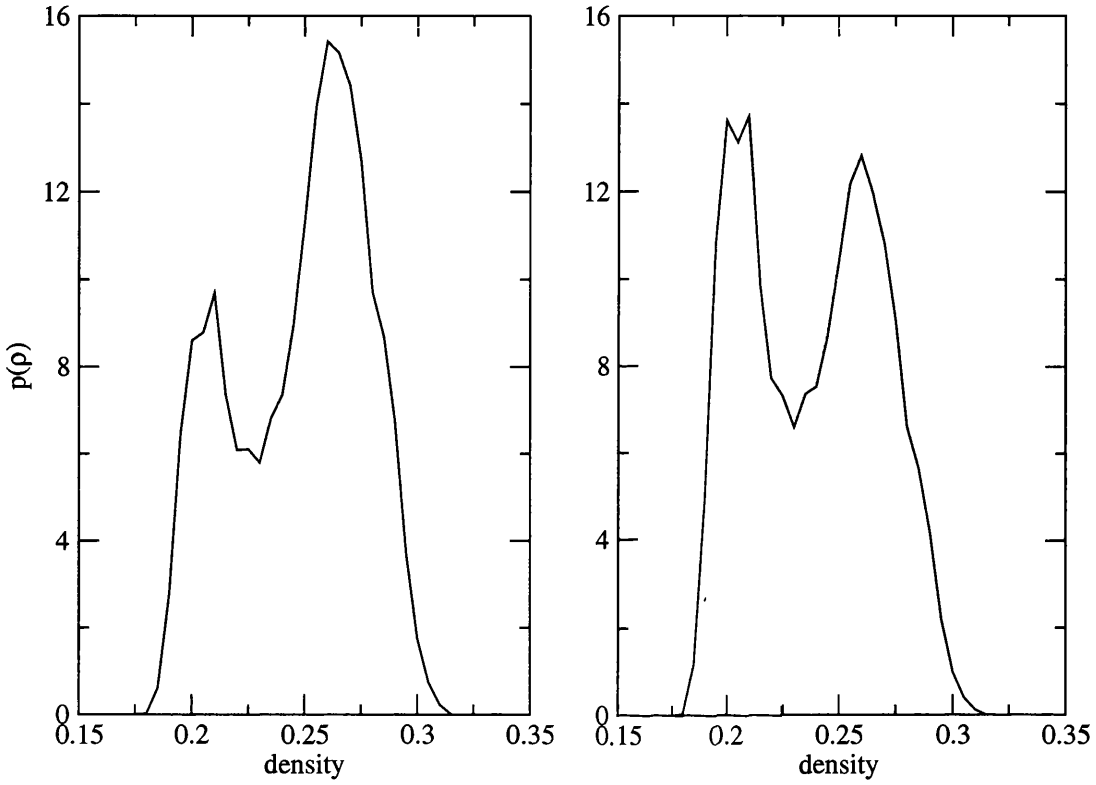

Figure 7.6: **(a)** The histogram of the density of the run at $T = 0.74$ and $P = 0.07$ for the parameter set $\sigma_1/\sigma_0 = 1.7$, $\sigma_2/\sigma_0 = 2.4$, and $\epsilon_r/\epsilon_a = 2$. **(b)** The resulting histogram after extrapolating the one in (a) to $T = 0.741$, $P = 0.0692$.

Section 7.5 such that $\epsilon_r = 0.7$, and plotted it on the same axes as Jagla's potential. As can be seen, in the Jagla potential small changes in the separation from the minimum of the potential towards the hard core result in small increments in internal energy. In contrast, in the square-well potential, a small change in the separation that results in the system moving from the minimum to the soft shoulder results in a huge leap in internal energy. As a result, this change in separation has a low acceptance rate, explaining why changes between the two preferred separation distances happened so rarely in the simulations of the square-well potentials.

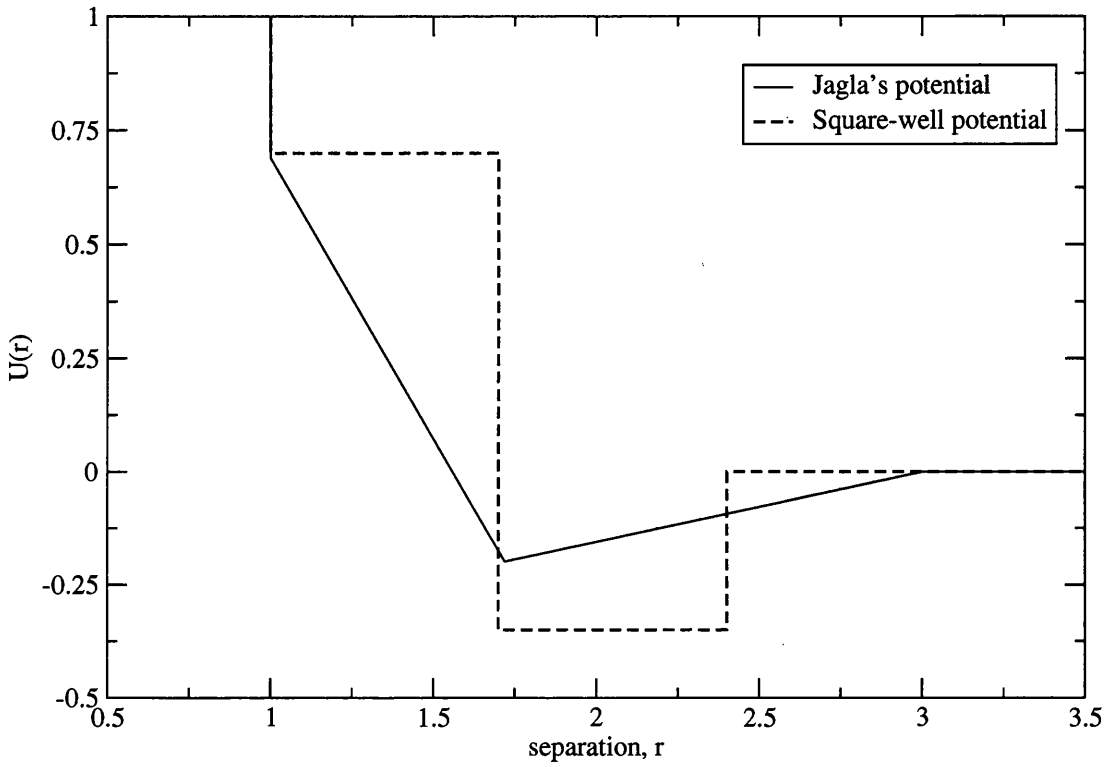

Figure 7.7: A plot showing Jagla's potential and the square-well potential studied in Section 7.5 on the same axes. The latter has been scaled so that $\epsilon_r = 0.7$.

Chapter 8

Conclusion and future work

In this thesis we have explored the relationship between the existence of a liquid-liquid critical point (LLCP) and the existence of a density anomaly (specifically a trend of increasing density with increasing temperature).

We used Jagla's model as our starting point, as it displayed both an LLCP and a density anomaly. However, our attempt to study it using the Lennard-Jones-Devonshire cell theory (Chapter 3) did not prove fruitful as the density anomaly was not reproduced, and there was even some question as to the identities of the phases. While the cell theory method showed that the phase diagram changed as the parameters of the potential were altered, the trend in the gradient of (what seemed to be) the liquid-liquid phase transition (LLPT) was the reverse of that found with the more reliable Monte Carlo simulation techniques.

Using Monte Carlo simulation techniques in the constant-NPT ensemble, we were able to analyse the structural differences of the two liquid phases, and the structural changes around the density maxima. We were also able to identify two distinct crystalline structures (HCP and FCC). We changed the pair potential whilst keeping the virial coefficient constant, and identified a potential for which the LLPT had a negative gradient, the LLCP was metastable with respect to the solid, and the density anomaly was stable, much as in the case of water.

We then altered the potential in such a way that the virial coefficient increased, and found that the density anomaly moved to lower temperatures relative to

the LLCP, and eventually became unstable. We also found that, for a potential with a higher virial coefficient, the density anomaly would move back to higher temperatures relative to the LLCP if the range of the potential was reduced whilst keeping the virial coefficient constant. This appeared strange when further studies showed that increasing the range of *Jagla's* pair potential, whilst keeping the virial coefficient constant, did not move the high-pressure end of the line of density maxima away from the LLCP.

Previous studies involving square-well potentials had not shown density anomalies. Curious to see if we could find a system with a density anomaly, we began by trying to reproduce previous results using our isobaric-isothermal Monte Carlo simulation technique. However, the simulations were too slow to allow accurate measurements to be taken.

Overall we have added substantially to the evidence supporting the second critical point theory of water by finding a potential that produces an LLCP and a negatively sloped LLPT, both metastable with respect to a solid of lower density, accompanied by a stable density anomaly. In addition we have shed some light on the link between the density anomaly and the LLCP, but further work is required to obtain a definitive answer to the question of why some pair potentials with LLPTs have density anomalies while others do not.

It would be valuable to do more analysis of how the changes in the phase diagrams, resulting from changes in the parameters of the interaction potential, are driven by energy and entropy. Further study along these lines may shed light on the reasons for the density anomaly disappearing at certain parameters, and being very closely linked to the critical point for other sets of parameters.

Dynamic studies of Jagla's pair potential found the more ordered HDL phase to be strong while the less ordered LDL phase was fragile. This is different from water, where the more ordered phase is the LDL phase, and therefore the LDL phase is strong and the HDL phase is fragile. In our studies, when $r_1 = 1.59$, we found a negatively sloped LLPT with the LDL phase being more ordered than the HDL phase, just as in water. It would be interesting to see if this resulted in the LDL phase also being the strong phase, and the HDL phase being the fragile phase, just as in water.

Further studies of the crystal phases found may also reveal interesting features. The more information gained, the closer we will be to a definitive answer to the complex behaviour of these ramp potentials, and how this is linked to the phase behaviour of water, silica, phosphorous, carbon and other substances which display liquid-liquid phase transitions.

Appendix

The table below details the parameters of pair potentials used. When put into equation 3.13 they produce ramp potentials with a second virial coefficient of $B_2 \approx -0.76 r_0^3$.

r_1	$D(r_1)$	r_2
1.25	0.460556	2.00769
1.3	0.432667	2.06848
1.4	0.376889	2.21068
1.5	0.321111	2.38847
1.58	0.276489	2.56631
1.59	0.270911	2.5914
1.60	0.265333	2.61721
1.61	0.259756	2.6438
1.62	0.254178	2.67118
1.63	0.2486	2.69941
1.64	0.243022	2.72853
1.65	0.237444	2.75859
1.66	0.231867	2.78963
1.68	0.220711	2.8549
1.7	0.209556	2.92483
1.72	0.1984	3.0
1.74	0.187244	3.08111
1.76	0.176089	3.169
1.78	0.164933	3.2647
1.80	0.153778	3.36984
1.82	0.142622	3.4849
1.84	0.131467	3.61299
1.86	0.120311	3.75637
1.88	0.109156	3.9185
1.90	0.098000	4.10416
1.92	0.0868444	4.31999
1.94	0.0756889	4.57582

References

[1] H. M. Gibson and N. B. Wilding. Metastable liquid-liquid coexistence and density anomalies in a core-softened fluid. *Physical Review E*, 73:061507, 2006.

[2] E. A. Jagla. Liquid-liquid equilibrium for monodisperse spherical particles. *Physical Review E*, 63:061501, 2001.

[3] L. Xu, P. Kumar, S. V. Buldyrev, S.-H. Chen, P. H. Poole, F. Sciortino, and H. E. Stanley. Relation between the Widom line and the dynamic crossover in systems with a liquid-liquid phase transition. *Proceedings of the National Academy of Sciences of the United States of America*, 102:16558–16562, 2005.

[4] J. S. Rowlinson and F. L. Swinton. *Liquids and Liquid Mixtures.* Butterworths Monographs in Chemistry. Butterworths, 3rd edition, 1982.

[5] P. G. De Gennes and G Prost. *The Physics of Liquid Crystals.* International Series of Monographs on Physics. Oxford University Press, 2nd edn edition, 1993.

[6] P. F. McMillan. Polyamorphic transformations in liquids and glasses. *Journal of Materials Chemistry*, 14:1506–1512, 2004.

[7] Rapoport. Model for melting curve maxima at high pressure. *Journal of Chemical Physics*, 46:2891, 1967.

[8] V. V. Brazhkin, R. N. Voloshin, A. G. Lyapin, and S. V. Popova. Quasi-transitions in simple liquids under high pressures. In A. Radzig, editor, *Physics-Uspekhi*, volume 42, pages 941–945, 1999.

[9] H. Tanaka. General view of a liquid-liquid phase transition. *Physical Review E*, 62:6968, 2000.

[10] Y. Katayama, T. Mizutani, W. Utsumi, O. Shimomura, M. Yamakata, and K. Funakoshi. A first-order liquid-liquid phase transition in phosphorus. *Nature*, 403:170–173, 2000.

[11] F. Monaco, S. Falconi, W. A. Crichton, and M. Mezouar. Nature of the first-order phase transition in fluid phosphorus at high temperature and pressure. *Physical Review Letters*, 90:255701, 2003.

[12] M. Togaya. Pressure dependences of the melting temperature of graphite and the electrical resistivity of liquid carbon. *Physical Review Letters*, 79:2474–2477, 1997.

[13] J. N. Glosli and F. H. Ree. Liquid-liquid phase transformation in carbon. *Physical Review Letters*, 82:4659, 1999.

[14] C. J. Wu, J. N. Glosli, G. Galli, and F. H. Ree. Liquid-liquid phase transition in elemental carbon: A first-principles investigation. *Physical Review Letters*, 89:135701, 2002.

[15] P. G. Debenedetti. Supercooled and glassy water. *Journal of Physics: Condensed Matter*, 15:R1669–R1726, 2003.

[16] R. J. Speedy and C. A. Angell. Isothermal compressibility of supercooled water and evidence for a thermodynamic singularity at $-45°$c. *Journal of Chemical Physics*, 65:851, 1976.

[17] O. Mishima and H. E. Stanley. The relationship between liquid, supercooled and glassy water. *Nature*, 396:329–335, 1998.

[18] R. J. Speedy. Stability-limit conjecture. An interpretation of the properties of water. *Journal of Physical Chemistry*, 86:982, 1982.

[19] S. Sastry, P. G. Debenedetti, F. Sciortino, and H. E. Stanley. Singularity-free interpretation of the thermodynamics of supercooled water. *Physical Review E*, 53:6144–6154, 1996.

[20] P. H. Poole, F. Sciortino, U. Essmann, and H. E. Stanley. Phase behaviour of metastable water. *Nature*, 360:324–328, 1992.

[21] O. Mishima, L. D. Clavert, and E. Whalley. An apparently first-order transition between two amorphous phases of ice induced by pressure. *Nature*, 314:76–78, 1985.

[22] O. Mishima, L. D. Calvert, and E. Whalley. 'Melting ice' I at 77 K and 10 kbar: a new method of making amorphous solids. *Nature*, 310:393–395, 1984.

[23] M. M. Koza, H. Schober, H. E. Fischer, T. Hansen, and F. Fujara. Kinetics of the high- to low-density amorphous water transition. *Journal of Physics: Condensed Matter*, 15:321–332, 2003.

[24] C. A. Tulk, C. J. Benmore, J. Urquidi, D. D. Klug, J. Newefeind, B. Tomberli, and P. A. Egelstaff. Structural studies of several distinct metastable forms of amorphous ice. *Science*, 297:1320–1323, 2002.

[25] O. Mishima and Y. Suzuki. Propagation of the polyamorphic transition of ice and the liquid-liquid critical point. *Nature*, 419:599–603, 2002.

[26] O. Mishima and H. E. Stanley. Decompression-induced melting of ice IV and the liquid-liquid transition in water. *Nature*, 392:164–168, 1998.

[27] L. Liu, S. Chen, A. Faraone, C. Yen, and C. Mou. Pressure dependence of fragile-to-strong transition and a possible second critical point in supercooled confined water. *Physical Review Letters*, 95:117802, 2005.

[28] I. Brovchenko, A. Geiger, and A. Oleinikova. Liquid-liquid phase transitions in supercooled water studied by computer simulations of various water models. *The Journal of Chemical Physics*, 123:044515, 2005.

[29] P. H. Poole, I. Saika-Voivod, and F. Sciortino. Density minimum and liquid-liquid phase transition. *Journal of Physics: Condensed Matter*, 17:L431–L437, 2005.

[30] E. Sanz, C. Vega, J. L. F. Abascal, and L. G. MacDowell. Phase diagram of water from computer simulation. *Physical Review Letters*, 92:255701, 2004.

[31] M. Yamada, S. Mossa, H. E. Stanley, and F. Sciortino. Interplay between time-temperature transformation and the liquid-liquid phase transition in water. *Physical Review Letters*, 88:195701, 2002.

[32] G. Franzese and H. E. Stanley. Understanding the unusual properties of water. *arXiv:cond-mat/0603634 v1*, 2006.

[33] C. A. Angell and H. Kanno. Density maxima in high-pressure supercooled water and liquid silicon dioxide. *Science*, 193:1121–1122, 1976.

[34] S. Sen, R. L. Andrus, D. E. Baker, and M. T. Murtagh. Observation of an anomalous density minimum in vitreous silica. *Physical Review Letters*, 93:125902, 2004.

[35] P. H. Poole, M. Hemmati, and C. A. Angell. Comparison of thermodynamic properties of simulated liquid silica and water. *Physical Review Letters*, 79:2281–2284, 1997.

[36] I. Saika-Voivod, F. Sciortino, and P. H. Poole. Computer simulations of liquid silica: Equation of state and liquid-liquid phase transition. *Physical Review E*, 63:011202, 2000.

[37] I. Saika-Voivod, P. H. Poole, and F. Sciortino. Fragile-to-stong transition and polyamorphism in the energy landscape of liquid silica. *Nature*, 412:514–517, 2001.

[38] I. Saika-Voivod, F. Sciortino, and P. H. Poole. Fragile-to-strong crossover and polyamorphism in liquid silica: changes in liquid structure. *Philosophical Magazine*, 84(13-16):1437–1445, 2004.

[39] H. Tanaka, R. Kurita, and H. Mataki. Liquid-liquid transition in the molecular liquid triphenyl phosphite. *Physical Review Letters*, 92:025701, 2004.

[40] V. V. Brazhkin, S. V. Popova, and R. N. Voloshin. Pressure-temperature phase diagram of molten elements: selenium, sulfur and iodine. *Physica B*, 265:64–71, 1999.

[41] J. Y. Raty, J. P. Gaspard, T. Le Bihan, M. Mezouar, and M. Bionducci. Local order of the high-pressure metallic phase of liquid selenium: a diffraction study. *Journal of Physics: Condensed Matter*, 11:10243–10249, 1999.

[42] F.H. Stillinger and A. Rahman. Improved simulation of liquid water by molecular dynamics. *Chemical Physics*, 60:1545–1557, 1974.

[43] A. B. de Oliveira and M. C. Barbosa. Density anomaly in a competing interactions lattice gas model. *Journal of Physics: Condensed Matter*, 17:399–411, 2005.

[44] S. S. Borick and P. G. Debenedetti. A lattice model of network-forming fluids with orientation-dependent bonding: Equilibrium, stability and implications for the phase behaviour of supercooled water. *Journal of Physical Chemistry*, 99:3781–3792, 1995.

[45] V. B. Henriques and M. C. Barbosa. Liquid polymorphism and density anomaly in a lattice gas model. *Physical Review E*, 71:031504, 2005.

[46] C. Buzano, E. de Stefanis, A. Pelizzola, and M. Pretti. Two-dimensional lattice-fluid model with water-like anomalies. *Physical Review E*, 69:061502, 2004.

[47] C. J Roberts and P. G. Debenedetti. Polyamorphism and density anomalies in network-forming fluids: Zeroth- and first-order approximations. *Journal of Chemical Physics*, 105:658–672, 1996.

[48] T. M. Truskett, P. G. Debenedetti, S. Sastry, and S. Torquato. A single-bond approach to orientation-dependent interactions and its implications for water. *Journal of Chemical Physics*, 111:2647–2655, 1999.

[49] P. C. Hemmer and G. Stell. Fluids with several phase transitions. *Physical Review Letters*, 24:1284–1287, 1970.

[50] J. M. Kincaid, G. Stell, and E. Goldmark. Isostructural phase transitions due to core collapse. II. A three-dimensional model with a solid-solid critical point. *Journal of Chemical Physics*, 65:2172–2179, 1976.

[51] P. J. Camp. Structure and dynamics in a monolayer of core-softened particles. *Journal of Molecular Liquids*, 127:10–13, 2006.

[52] G. Malescio and G. Pellicane. Stripe patterns in two-dimensional systems with core-corona molecular architecture. *Physical Review E*, 70:021202, 2004.

[53] M. R. Sadr-Lahijany, A. Scala, S. V. Buldyrev, and H. E. Stanley. Liquid-state anomalies and the Stell-Hemmer core-softened potential. *Physical Review Letters*, 81:4895–4898, 1998.

[54] N. B. Wilding and J. E. Magee. Phase behavior and thermodynamic anomalies of core-softened fluids. *Physical Review E*, 66:031509, 2002.

[55] P. Mausbach and H. O. May. A MBWR-equation of state of a core-softened fluid in 3D. *Fluid Phase Equilibria*, 214:1–9, 2003.

[56] D. Quigley and M. I. J. Probert. Progression of phase behavior for a sequence of model core-softened potentials. *Physical Review E*, 72:061202, 2005.

[57] A. Skibinsky, S. V. Buldyrev, G. Franzese, G. Malescio, and H. E. Stanley. Liquid-liquid phase transitions for soft-core attractive potentials. *Physical Review E*, 69:061206, 2004.

[58] M. R. Sadr-Lahijany, A. Scala, S. V. Buldyrev, and H. E. Stanley. Waterlike anomalies for core-softened models of fluids: One dimension. *Physical Review E*, 60:6714–6721, 1999.

[59] G. Franzese, G. Malescio, A. Skibinsky, S. V. Buldyrev, and H. E. Stanley. Generic mechanism for generating a liquid-liquid phase transition. *Nature*, 409:692–695, 2001.

[60] B. Pellicane, G. Pellicane, and G. Malescio. Polymorphism in simple liquids: A Gibbs Ensemble Monte Carlo study. *Journal of Chemical Physics*, 120:8671–8675, 2004.

[61] S. V. Buldyrev, G. Franzese, N. Giovambattista, G. Malescio, M. R. Sadr-Lahijany, A. Scala, A. Skibinsky, and H. E. Stanley. Models for a liquid-liquid phase transition. *Physica A*, 304:23–42, 2002.

[62] E. A. Jagla. Phase behavior of a system of particles with core collapse. *Physical Review E*, 58:1478–1486, 1998.

[63] E. A. Jagla. Core-softened potentials and the anomalous properties of water. *Journal of Chemical Physics*, 111:8980–8986, 1999.

[64] L. Xu, S. V. Buldyrev, C. A. Angell, and H. E. Stanley. Thermodynamics and dynamics of the two-scale spherically-symmetric Jagla model of anomalous liquids. *Physical Review E*, 74:031108, 2006.

[65] L. Xu, I. Ehrenberg, S. V. Buldyrev, and H. E. Stanley. Relation between the liquid-liquid phase transition and dynamic behavior in the Jagla model. *arXiv:cond-mat*, 2:0604022, 2006. http://arxiv.org/pdf/cond-mat/0604022.

[66] J. E. Magee and N. B. Wilding. The Lennard-Jones-Devonshire cell model revisited. *Molecular Physics*, 100:1641–1644, 2002.

[67] M. P. Allen and D. J. Tildesley. *Computer Simulation of Liquids.* Oxford Science Publications, 1989.

[68] B. Smit. Phase diagrams of Lennard-Jones fluids. *Journal of Chemical Physics*, 96:8639, 1992.

[69] Y. V. Kalyuzhiny and P. T. Cummings. Phase diagram for the Lennard-Jones fluid modelled by the hard-core Yukawa fluid. *Molecular Physics*, 87:1459–1462, 1996.

[70] N. B. Wilding. Generic sampling strategies for Monte Carlo simulation of phase behaviour. In M. Ferrario, G. Ciccotti, and K. Binder, editors, *Computer Simulations in Condensed Matter: From Materials to Chemical Biology*, volume 703 of *Lecture Notes in Physics*, pages 39–66. Springer, 2006.

[71] D. Frenkel and B. Smit. *Understanding Molecular Simulation.* Academic Press, 1996.

[72] N. B. Wilding. Critical-point and coexistence-curve properties of the Lennard-Jones fluid: A finite-size scaling study. *Physical Review E*, 52:602, 1995.

[73] M. M. Tsypin and H. W. J. Bl"ote. Probability distribution of the order parameter for the 3d Ising model universality class: a high precision Monte Carlo study. *Physical Review E*, 62:73–76, 2000.

[74] N. B. Wilding. Computer simulation of fluid phase transitions. *American Journal of Physics*, 69:1147–1155, 2001.

[75] A. M. Ferrenberg and R. H. Swendsen. Optimized Monte Carlo data analysis. *Physical Review Letters*, 63:1195, 1989.

[76] S. S. Borick and P. G. Debenedetti. Equilibrium, stability, and density anomalies in a lattice model with core-softening and directional bonding. *Journal of Physical Chemistry*, 97:6292–6303, 1993.

[77] G. Franzese, M. I. Marque's, and H. E. Stanley. Intramolecular coupling as a mechanism of a liquid-liquid phase transition. *Physical Review E*, 67:011103, 2003.

[78] C. J. Roberts and P. G. Debenedetti. Polyamorphism and density anomalies in network forming fluids: Zeroth- and first-order approximations. *Journal of Chemical Physics*, 105:658–672, 1996.

[79] J. B. Caballero and A. M. Puertas. Density anomaly and liquid-liquid transition from perturbation theories. *Physical Review E*, 74:051506, 2006.